Title
High Voltage Reactivity in Lithium Batteries

Author
Papp, Joseph K

Publication Date
2020

High Voltage Reactivity in Lithium Batteries

by

Joseph K. Papp

A dissertation submitted in partial satisfaction of the

requirements for the degree of

Doctor of Philosophy

in

Chemical Engineering

in the

Graduate Division

of the

University of California, Berkeley

Committee in charge:

Professor Bryan D. McCloskey, Chair
Professor Nitash P. Balsara
Professor Gerbrand Ceder

Summer 2020

High Voltage Reactivity in Lithium Batteries

Abstract

High Voltage Reactivity in Lithium Batteries

by

Joseph K. Papp

Doctor of Philosophy in Chemical Engineering

University of California, Berkeley

Professor Bryan D. McCloskey, Chair

A major limit of electric vehicle performance is the energy density of available mobile energy storage systems. Lithium ion (Li-ion) batteries are now well-known and have enabled many portable electronics as well as electronic vehicles. However, for greater market penetration and range competitiveness, a battery with greater practical energy density must be designed. This dissertation focuses on three methods of improving energy density in lithium based batteries: lithium oxygen (Li-O_2) batteries, Li-rich cathodes for Li-ion batteries, and high voltage operation of simple transition metal oxide cathodes for Li-ion batteries. To evaluate each of these technologies, the reactivity of each system is monitored.

Li-O_2 batteries, a “beyond Li-ion” battery technology, have a very high theoretical energy density that is difficult to realize. After initial excitement surrounding the novel chemistry, many challenges associated with Li-O_2 batteries have been highlighted in the past decade. Among these challenges, the reactivity of oxygen in the system is one of the most pressing. In this dissertation, the possible stability of LiO_2, an advantageous discharge product to the typical Li_2O_2, is examined alongside binder degradation in the system.

As the workings of a Li-ion battery require the removal and intercalation of Li, the theoretical capacity is determined by the amount of Li available for extraction from the cathode. Consequently, a method of increasing energy density in Li-ion batteries is to increase the stoichiometric ratio of Li in the cathode material. These ”Li-rich” cathode materials demonstrate large capacities, but must compensate the additional Li with cation double redox or anion redox. The electrochemical cells must be operated to > 4.5 V vs Li/Li^+ to reach these additional capacities, and this operation results in greater reactivity and instabilities. This dissertation examines the trends of high voltage instability, especially as it relates to oxygen redox, in these Li-rich cathode materials.

Typical Li-ion batteries utilize only a fraction of the theoretical capacity available, only extracting around half of the available lithium from the layered transition metal oxide cath-

ode material during charge. This is due to enhanced degradation mechanisms and reduced cyclability when additional Li is extracted at the necessitated higher voltages. Enabling operation of layered transition metal oxides at high voltages would result in increased capacity without the need for "beyond Li-ion" technologies. But first, the instabilities associated with Li extraction at voltages beyond the typical cut-off must be well-studied. Currently, the stability and degradation mechanisms of cathode materials even as common as $LiCoO_2$ remain unclear. In studies presented in this dissertation, high voltage reactivity for layered transition metal oxide cathode materials is investigated.

The main conclusions of the studies presented here are drawn from measurements monitoring the reactivity of each of the aforementioned technologies. Among the measurements presented in these studies, outgassing and gas evolution measurements by differential electrochemical mass spectrometry have proved paramount in utility. As cell reactivity and instability at high voltages is often accompanied by outgassing, these measurements have assisted in the elucidation of instability origins. Practical application of Li-O_2 batteries remains elusive as additional instabilities are discovered, Li-rich cathode materials show promise as various methods of mitigating high voltage instabilities are discussed, and the major sources of high voltage reactivity of layered transition metal oxide cathode materials are evaluated here.

Contents

List of Figures

List of Tables

Acknowledgments

I would first like to thank my advisor, Professor Bryan McCloskey, for his guidance and support throughout my entire graduate career. Thank you, Bryan, for teaching me electrochemistry and what it means to be a scientist. Thank you also for patiently and consistently providing invaluable advice throughout the challenges and successes I've encountered at Berkeley.

I am grateful to Professor Alexis Bell, Professor Gerbrand Ceder, Professor Nitash Balsara, and Professor Jeffrey Reimer for serving on my qualifying exam committee. Thank you Carlet Altamirano and Joseph Nolan for your administrative support and encouragement.

I am also grateful to all of my fellow colleagues in the McCloskey lab. Thank you, all of you, who have provided friendship, encouragement, and valuable scientific discussion. Colin, Sara, and Jessica, thank you especially for helping me build a foundation of skills upon which all of my subsequent research has been built.

Thank you also to my many collaborators, all who have helped make my graduate career successful. Thank you to Professor Reza Younesi for hosting me at Uppsala University and your assistance with my X-ray photoelectron spectroscopy studies there. Thank you also to Dr. Wei Tong, Dr. Wanli Yang, Dr. Jinhyuk Lee, Dr. Ning Li, and the many other collaborators who have been critical to my research success.

Thank you to the many friends I have made during my time at Berkeley who have made my experience enjoyable and unforgettable. Thank you especially to Gumi for your continual encouragement and understanding. I can't imagine getting through graduate school without you.

Finally, thank you to my family for your ceaseless support and encouragement throughout my whole life. Amy and Jana, thank you for being great sisters and role models, and for each pushing me to grow. Mom and Dad, thank you for instilling within me a strong sense of curiosity and a desire to learn, as well as for urging me to pursue whatever interested me.

For financing my research, I am grateful to the National Science Foundation Graduate Research Fellowship Program as well as the Energy & Biosciences Institute through the EBI-Shell program.

Chapter 1

An Introduction to Lithium Batteries

1.1 Lithium Battery Basics

After the commercialization of Li-ion batteries in the early 1990s, the market share of lithium based energy storage technologies has continuously increased. Li-ion batteries now provide energy to numerous types of portable electronic devices as well as most commercial electric vehicles (EVs). Since Sony first introduced Li-ion batteries to the market in 1991, advances in materials chemistry and cell engineering have allowed the energy density of commercial Li-ion batteries to increase, and the cost per unit energy stored to decrease. However, for continued market penetration in demanding applications, such as EVs and grid scale storage, advances in Li-ion batteries are needed to achieve greater energy density and lower cost that can allow electricity to better rival fossil fuels as an energy carrier.[1,2]

1.1.1 Li-ion Batteries

The chemistry of a typical Li-ion battery is ostensibly straight forward. Batteries are composed of electrochemical cells, and each cell has three primary active components: the cathode, the anode, and the electrolyte. The cathode, the positive electrode, is typically a porous composite comprised of a layered transition metal oxide powder, a high surface area carbon black additive to improve electronic conductivity, and a polymer binder, such as poly(vinylidene fluoride). The electrode is typically prepared by creating a slurry in a solvent in which the polymer can dissolve, followed by coating the slurry on a metal (typically aluminum for the cathode) foil current collector, and then evaporating the solvent to leave the dry, porous composite. The transition metal oxide is typically referred to as the active material, where Li ions can insert in and deinsert from the oxide's crystal lattice in an electrochemically reversible process referred to as intercalation or deintercalation, respectively. The anode, the negative electrode, is similar in composition, although graphitic carbon powder is used as the active material and copper foil as the current collector. Li ions can intercalate between the graphene layers in graphite and do so at potentials much lower than that in which they intercalate into a layered transition metal oxide, thereby creating a potential energy difference between the electrodes that is exploited for energy storage. The electrolyte conducts Li ions between the electrodes and is usually composed of linear and cyclic carbonate solvents and Li salt in conventional Li-ion batteries. Between the electrodes, a polymer separator is also often used to physically and electrically separate the electrodes. The electrolyte ideally fills the entire porous structure of each electrode and separator, thereby leaving no unfilled void space throughout the entire anode-separator-cathode stack. A simplified schematic of a Li-ion electrochemical cell, without the carbon black, binder, or current collectors for clarity, is shown in Figure 1.1.

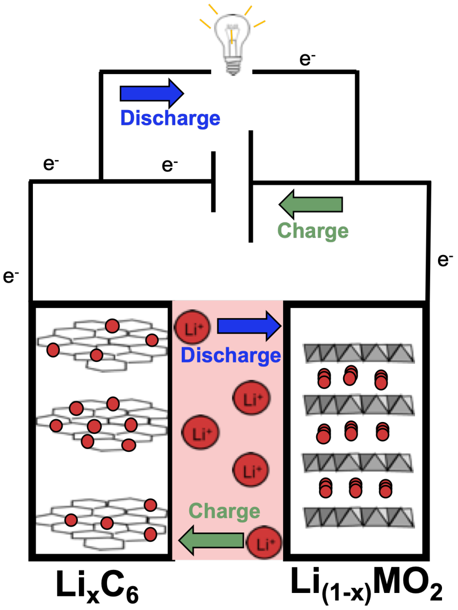

Figure 1.1: Simplified diagram of a Li-ion cell containing a graphite anode and a layered transition metal oxide cathode.

The operation of a Li-ion battery necessitates the shuttling of Li^+ ions between the cathode and anode while the electrons facilitate work in an external circuit on discharge. The ideal electrochemical reactions for this process during charge, where M is a general transition metal, are as follows:

$$\text{Anode}: xLi^+ + xe^- + C_6 \longrightarrow Li_xC_6 \tag{1.1}$$

$$\text{Cathode}: LiMO_2 \longrightarrow Li_{1-x}MO_2 + xLi^+ + xe^- \tag{1.2}$$

$$\text{Net}: LiMO_2 + C_6 \longrightarrow Li_{1-x}MO_2 + Li_xC_6 \tag{1.3}$$

For charge neutrality to be maintained, the general transition metal, M, must compensate the removal of the positive charge accompanying the Li ion. As this process must be reversible for a secondary battery, M is required to have an appropriate redox couple (e.g., M^{3+}/M^{4+}). Therefore, if M fully compensates the intercalation of Li in the cathode, the formal oxidation state of M will be +3 at a state of complete discharge ($x = 0$) and +4 at a state of complete charge ($x = 1$). In this way, the available M redox and total Li present are used to dictate the theoretical capacity of transition metal oxide (TMO) cathode material. Typical gravimetric capacities of some common layered TMOs, graphite, and Li metal are provided in Table 1.1, and as can be seen, the capacities of the anode materials are usually much higher than for the TMOs.

Material	**Theoretical Capacity (mAh g^{-1})**	**Reversible Capacity (mAh g^{-1})**
$LiCoO_2$	274	140[3]
$LiMn_2O_4$	148	125[3]
$LiNiO_2$	274	125[4]
$Li(NiMnCo)_{1/3}O_2$	278	180[5]
Graphite	372	350[3]
Li Metal	3860	N/A

Table 1.1: Theoretical and reversible capacities of example transition metal oxides (cathode materials) as well as graphite and Li metal (anode materials). No commercial cells are available that use Li metal as an anode, and hence its reversible capacity is not provided.

Due to instabilities and enhanced reactivity as Li ions are removed from the cathode, the total theoretical capacity of transition metal oxides cannot practically be achieved without severe loss of capacity retention on subsequent cycles. $LiCoO_2$, the first commercialized Li-ion battery cathode material that remains widely used in mobile electronics, can only tolerate the removal of roughly half its lithium content before irreversible degradation begins.[6–8] This extraction limit, along with the cost and toxicity of Co, has encouraged the search for alternative cathode materials. $LiNiO_2$ was briefly considered due to its identical structure and similar redox couple charge compensation to $LiCoO_2$. Unfortunately, $LiNiO_2$ is not only also limited by irreversible degradation during Li ion extraction, but also suffers from cation migration between the Li and transition metal layers and a difficult synthesis.[9,10] Spinel materials such as $LiMn_2O_4$ are utilized because of their extreme stability, but remain poor replacements for $LiCoO_2$ in terms of capacity.[11,12] Instead, transition metal oxide materials combining Ni, Mn, and/or Co (NMCs) have been developed that combine beneficial characteristics of each. The batteries based on these materials currently have the largest practical capacities among commercialized batteries. Each of these cathode materials maintain crystal structures that facilitate the intercalation of Li ions that has largely been viewed as a requirement for cathode materials. $LiCoO_2$ and $LiNiO_2$ adopt the α-$NaFeO_2$

structure, a derivative of the rocksalt NaCl structure.[7,9] This structure maintains "layered" planes of alternating metal and O ions, such that the stacking becomes O-Li-O-M-O-Li-.... The neat layering enables two dimensional Li^+ transport through the Li planes. $LiMn_2O_4$ adopts a spinel structure that restricts Li^+ transport to one dimension.[12] This more restrictive structure has greater rate capability when compared to a layered rocksalt, however it cannot maintain as great a lithium content, and hence has lower electrochemical capacity.[13]

1.1.2 Li-O_2 Batteries

Lithium oxygen (Li-O_2) batteries are being explored as potential high energy alternatives to Li-ion batteries.[14] Li-O_2 batteries have an extremely large theoretical capacity made possible by incorporating a Li metal anode and a transition metal free cathode material. Rather than a transition metal oxide intercalation cathode, the cathode for a Li-O_2 cell is commonly carbon black powder bound to a metal mesh current collector using a fluorinated polymer. The porosity of the electrode and current collector allow access to an oxygen gas reservoir (ideally air), such that lithium ions react with oxygen gas at the cathode to form lithium peroxide, Li_2O_2, as the discharge product. The anode of a Li-O_2 cell is Li metal, another factor in the increased energy density of this cell chemistry given its high theoretical capacity, as seen in Table 1.1. Initially, similar electrolyte compositions to Li-ion cells were used for Li-O_2 cells, but it was discovered that carbonate based solvents readily degrade in the presence of the Li-O_2 discharge reactions.[15] Therefore, Li salts dissolved in ether based solvents are typically used as electrolytes in Li-O_2 cells. A simplified schematic of a Li-O_2 electrochemical cell is shown in Figure 1.2.

Many challenges are associated with the chemistry of a Li-O_2 battery, not least of which is the insulating Li_2O_2 discharge product. As the cell is discharged, the Li_2O_2 discharge product accumulates on the carbon cathode until a critical thickness (only a few nanometers) is reached that disallows electron tunneling.[16] This electronic passivation is one of the key limits to the practical capacity of a Li-O_2 battery, but a host of other issues also arise during operation. For example, if the oxygen reservoir is not pure oxygen, a number of possible side reactions involving CO_2 and humidity will occur that greatly decrease efficiency. This introduces additional weight in any proposed Li-O_2 battery pack design due to the necessary pressurized O_2 gas reservoir.[14]

1.2 Necessary Improvements for EV Batteries

Improvements must be made to modern commercialized lithium batteries for greater market penetration of electric vehicles. Primary concerns for drivers of electric vehicles are range, safety, charging time, and cost.[17] Each of these areas has seen improvement over the past decades, but a major demand remains for gains in each.

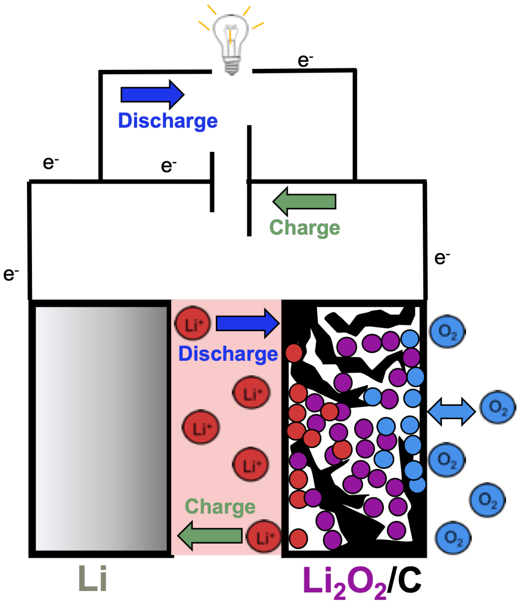

Figure 1.2: Simplified diagram of a Li-O_2 cell containing a Li metal anode and a porous carbon cathode.

1.2.1 Range

There are a varied number of options for improving the capacity of lithium batteries to alleviate range anxiety for potential electric vehicle owners. For Li-ion batteries, the capacity and energy density can be increased by either increasing the gravimetric electrochemically reversible lithium content in each active material, or by increasing the potential difference between the electrodes. Increasing the potential difference between electrodes typically involves strategies to raise the operational voltage of the cathode, as Li insertion into graphite occurs at a voltage very close the thermodynamic limit of reversible Li/Li^+ redox (10-100 mV vs. Li/Li^+).[18,19] However, in raising the cathode voltage, increased instabilities related to TMO phase transitions and interfacial degradation of both the electrode and electrolyte are observed, but poorly understood.[20] Therefore, efforts to better understand these high voltage instabilities are needed to continuously enhance energy storage capacity of Li-ion batteries. An alternative strategy to increase battery energy is to develop new materials with more reversible Li capacity per unit volume or weight. As an example, Increasing the lithium content of layered TMOs can be done by synthesizing “Li-excess” materials with a stoichiometric excess of lithium (Li_xMO_2, x>1).[21] The excess lithium provides a greater theoretical capacity, but the additional charge removal must be compensated by either M double redox or lattice oxygen redox, both of which have proven to be poorly reversible in prior studies.[22,23] A more difficult route to increasing capacity is to alter the typical chemistry used in lithium batteries to a more energy dense chemistry, such as Li-O_2, Li-S, or divalent Mg-ion batteries. More recent research in Li-O_2 battery chemistry has also lead to novel materials showing oxygen redox without an accompanying need for an oxygen gas reservoir, potentially pushing a form of oxygen redox batteries nearer to commercialization.[24] Nevertheless, these battery chemistries also suffer from challenges that limit their rechargeability and commercialization, as was discussed in the section above.

1.2.2 Safety

While a greater capacity is required to relieve range anxiety, high degrees of lithium extraction from TMOs is often accompanied by instabilities that can cause safety concerns. Not least among the concerns is gas evolution that could result in battery expansion, shorting, and ignition. It is therefore necessary to carefully examine instabilities associated with increased energy density and capacity to maintain the safety of lithium battery powered electric vehicles.

1.2.3 Cost

The cost of Li-ion batteries have greatly decreased over the past three decades largely due to optimized cell engineering and production.[25,26] But use of cheaper materials has also helped reduce costs. Of the battery materials commonly used, cobalt is one of the most expensive components due to its relative scarcity.[27] Efforts to move away from cobalt have resulted in Ni-rich cathode materials (e.g., Ni-rich NMCs), but there is continued interest in utilizing more cost-effective alternatives. Manganese based compounds have therefore been explored given Mn's abundance compared to Ni and Co, and have the additional benefit of a possible double redox capability (Mn^{2+}/Mn^{4+}) at high voltages vs. Li/Li^{+}, which could dramatically enhance material capacity.[27]

1.3 Monitoring High Voltage Reactivity

This dissertation focuses on the aforementioned instabilities associated with high capacity/high energy density lithium battery technologies. Investigating the high voltage reactivity of intercalation cathodes and Li-O_2 reactions is made possible by numerous characterization techniques discussed throughout this dissertation. Particular attention is given to outgassing and gas evolution monitoring measurements during applied electrochemical techniques to lithium cells. In the case of Li-O_2 cells, oxygen gas consumption and evolution is critical to understanding the efficiency of the Li_2O_2 discharge product formation and its reversible oxidation back to O_2 during charging. Outgassing can also provide information on the mechanisms of side reactions that define high voltage instabilities in Li-ion batteries, specifically through the identification and quantification of the masses of gas observed. Additional information is gained through isotopic labeling of the cell components in certain cases. High voltage lithium battery materials and associated reactivity are also investigated with a large number of other characterization techniques as discussed in the relevant chapters.

The objective of this dissertation is to provide a greater understanding of high voltage instabilities and reactivity in lithium battery cathode materials. Chapter 2 examines Li-O_2 batteries and the stability and mechanism of formation for the Li_2O_2 discharge product. This study also reveals the propensity for binder degradation in Li-O_2 cell cathodes, which then creates a spectroscopic signature that complicates discharge product characterization. Chapter 3 highlights various outgassing studies of cobalt-free Li-excess disordered rocksalt cathode materials with very high experimental capacities. Chapter 4 focuses on the layered Li_2MnO_3 material, the parent compound for many Li-excess transition metal oxides, and demonstrates common irreversible degradation processes associated with severe oxygen redox when it is operated to high voltages. Oxygen redox at high voltages is studied in more depth for $LiCoO_2$, $LiNiO_2$, and Li_2MnO_3 in Chapter 5, as cycling studies and isotopic labeling reveal reactivity (or lack of it) in these layered transition metal oxides. Finally, Chapter 6 explores the use of transition metal doping to enable highly disordered Li_2O based cathode materials that exhibit extreme oxygen activity.

Chapter 2

PVDF Binder Degradation in Li-O_2 Batteries

2.1 Abstract

In this study, a common Li-O_2 battery cathode binder, poly(vinyidene fluoride) (PVDF), is shown to degrade in the presence of reduced oxygen species during Li-O_2 discharge when adventitious impurities are present. This degradation process forms products that exhibit Raman shifts (~1133 and 1525 cm^{-1}) nearly identical to those of lithium superoxide (LiO_2), complicating the identification of LiO_2 in Li-O_2 batteries. These peaks do not appear on extracted cathodes when poly(tetrafluoroethylene) (PTFE) is used as a binder, even when used to bind iridium decorated reduced graphene oxide (Ir-rGO) based cathodes similar to those that reportedly stabilize bulk LiO_2 formation. In all discharges in which the 1133 and 1525 cm^{-1} Raman shifts are observed on extracted carbon cathodes, only a 2.0 e$^-$/O_2 process is identified, and Li_2O_2 is predominantly formed (along with typical parasitic side product formation). These results strongly suggest that bulk, stable LiO_2 formation via the 1 e$^-$/O_2 process is not an active discharge reaction in Li-O_2 batteries.*

2.2 Introduction

Lithium-air (Li-O_2) batteries can theoretically provide extraordinarily high specific energy compared to current lithium-ion batteries.[28–30] Unfortunately, their development is inhibited by parasitic reactions that limit cell rechargeability, among other challenges. Although the exact mechanism of the Li-O_2 cathode electrochemistry depends on a variety of cathode and electrolyte properties, the dominant discharge process is oxygen reduction at the cathode to form solid lithium peroxide, Li_2O_2, through a transient superoxide intermediate, e.g.:[31–35]

---

[*] This chapter adapted with permission from previously published work in: Papp et al. *J. Phys. Chem. Lett.* **2017**, 8, 6, 1169–1174.

$$Li^+ + e^- + O_2 \rightleftharpoons LiO_2 \tag{2.1}$$

$$Li^+ + e^- + LiO_2 \rightleftharpoons Li_2O_2 \text{ or} \tag{2.2}$$

$$2LiO_2 \rightleftharpoons Li_2O_2 + O_2 \tag{2.3}$$

The formation and oxidation of Li_2O_2 causes numerous challenges for the development of practical Li-O_2 batteries. Li_2O_2 is a wide bandgap insulator and insoluble in known organic electrolytes. It therefore greatly limits practical battery capacities by passivating the cathode surface as it is formed.[36–39] It also is highly reactive, resulting in the aforementioned rechargeability limitations.[40–45] As a result, recent studies have described Li-O_2 cell compositions that may result in the formation of potentially less reactive products and hence may provide a route to improved battery rechargeability.[46,47] Of particular interest, a series of studies have reported a route to stabilizing the LiO_2 intermediate such that it comprises a sizeable fraction of the ultimate discharge product.[47–50] Using a standard ether-based electrolyte composition, these studies have reported 'superoxide-like species' formed on ultra-high surface area carbon cathodes and pure LiO_2 formation on Ir-decorated reduced graphene oxide (Ir-rGO) electrodes. The most compelling spectroscopic technique employed to identify the LiO_2 and LiO_2-like species in theses studies was ex-situ Raman spectroscopy on cathodes extracted from cells after discharge.[47] By combining density functional theory calculations with Raman spectroscopy, two observed peaks (1123 cm^{-1} and 1505 cm^{-1}) were ascribed to LiO_2 and LiO_2-like species formation as a discharge product. These ex-situ Raman results are unexpected given that bulk LiO_2 has been previously reported to be unstable at room temperature and ambient pressures.[51]

It was briefly noted in review articles that the observation of Raman shifts at similar frequencies (namely 1125 cm^{-1} and 1525 cm^{-1}) was a common, and surprising, occurrence when characterizing cathodes extracted from discharged cells in early Li-O_2 studies.[29,30,52] These studies were performed using a standard cathode composition, namely carbon black powder (Vulcan XC72) bound to P50 AvCarb carbon paper using a poly(vinylidene fluoride) (PVDF) binder, and a standard ether-based electrolyte. However, it was noticed that the Raman peaks at 1125 and 1525 cm^{-1} were not observed if cathode compositions were employed that did not include PVDF. After isolating the cause of these Raman signatures, which were ascribed to PVDF degradation during oxygen reduction in Li-O_2 cells where minor, uncontrolled impurities were present, a switch to poly(tetrafluoroethylene) (PTFE) as a binder eliminated the occurrence of these peaks. Additionally, it was determined that electrode preparation procedure (in particular, the final temperature at which they are dried), which influenced the amount of impurities present after electrode preparation, also influenced the appearance of these peaks when PVDF was used as the binder. In light of recent reports ascribing similar Raman peaks to bulk, stabilized LiO_2 as a final discharge product, this study presents results on PVDF degradation to show how it might be misconstrued as LiO_2 when using Raman spectroscopy studies. Of particular importance, all articles in which

LiO_2 or LiO_2-like species have been observed as final, stable discharge products use PVDF (Kynar) as a cathode binder.[47–50] In-operando Raman spectroscopy of the Li-O_2 electrochemistry occurring at binder-less glassy carbon and roughened gold electrodes has indeed shown Raman peaks near 1125 cm^{-1} and 1525 cm^{-1} that can be ascribed to LiO_2.[34,35,53] However, this LiO_2 is only observed as a transient, unstable intermediate to Li_2O_2 formation, rather than a stabilized final product. Standard carbon cathodes are studied, such as those prepared from XC72 carbon black bound using PTFE and PVDF, as are iridium nanoparticle decorated reduced graphene oxide (Ir-rGO) electrodes that are similar to those used in a previous study that reported stable bulk LiO_2 formation.[47] Two important results are identified in this study: 1) Raman peaks appear at 1133 cm^{-1} and 1525 cm^{-1} only in cells that use PVDF binders, and only then if they are not fully dried after preparation under ambient atmosphere. 2) Regardless of the electrode composition employed (binder, catalyst, preparation conditions), only a 2 e^-/O_2 process is observed and never a 1 e^-/O_2 process either on discharge or charge. These results do not exclude the possibility of a small amount ($<1\%$ of total product formation) of LiO_2 formation as possible stable discharge product, and no further claim is made on the possibility of LiO_2 as a stable product. These results hopefully spur further exploration into stable LiO_2 formation, which remains an interesting open question.

2.3 Experimental Methods

2.3.1 Materials

Iridium chloride ($IrCl_3$), ammonium hydroxide (NH_4OH), poly(tetrafluoroethylene) emulsion (60 wt%, PTFE), poly(vinylidene fluoride) (MW = 180,000 g/mol, PVDF), N-methyl 2-pyrrolidone (NMP), and sodium hydroxide (NaOH) were all purchased from Sigma Aldrich. The graphite used as the feedstock for graphene oxide synthesis was acquired from Bay Carbon Inc. 1,2-Dimethoxyethane (DME), and lithium bis(trifluorosulfonylimide) (LiTFSI) were purchased from BASF. P50 Avcarb carbon paper (P50) and XC72 Vulcan carbon black powder (XC72) were purchased from the Fuel Cell Store. Lithium metal was purchased from FMC.

2.3.2 Ir-GO Synthesis and Characterization

Graphene oxide (GO) was synthesized by a modified Hummer's method, and the Ir-rGO was prepared by a simple thermal reduction method.[54,55] GO was mixed and ultrasonicated in a 300 mL aqueous solution (0.1 wt%) followed by the addition of 100 mg $IrCl_3$ and a repetition of stirring and sonication. 10 mL 5M NH_4OH was then added as a reducing agent and the solution was heated at 100 °C for 12 hours under a nitrogen atmosphere. After filtering and drying in a vacuum oven at 100 °C, the produced powder was annealed at 450 °C for 3 hours under an inert atmosphere (N_2). The final Ir-rGO product was characterized by powder X-ray diffraction (PXRD), scanning transmission electron microscopy (TEM), and X-ray photoelectron spectroscopy (XPS). PXRD (Bruker) was used to determine iridium decoration in rGO and estimate the size of the iridium nanoparticles in the Ir-rGO samples. The PXRD results (Figure 2.1a) show the appearance of the Ir(111) metal diffraction pattern after the synthesis procedure,[56] without the presence of $IrCl_3$ reflections. An estimation for the size of the iridium nanoparticles based on peak broadening using the Scherrer equation is $\sim$1.5 nm. TEM (JEOL 2100-F 200 kV Field-Emission Analytical Transmission Electron Microscope) was employed to determine the morphology, dispersion, and particle size of the iridium in the Ir-rGO samples. Samples for TEM were prepared by placing a drop of an ultra dilute solution of Ir-rGO on a copper grid that was then dried. TEM images (Figure 2.1b) show that the iridium nanoparticles decorating the rGO are well dispersed and generally very small (< 2 nm). X-ray photoelectron spectroscopy (XPS) was carried out to verify the chemical structure of Ir-rGO using a monochromatized Al Kα X-ray source (Quantum2000, Physical electronics, Chanhassen, MN, USA). Figure 2.1c shows representative XPS spectra of the Ir 4f edge in Ir-rGO, which was then deconvoluted by Gaussian curve fitting. The peaks at 61.2 and 64.1 eV are ascribed to metallic iridium (Ir $4f_{7/2}$ and Ir $4f_{5/2}$), with minor shoulders at 62.6 and 65.7 eV due to the presence of IrO_2.[47] From TEM and XPS data, we confirm that metallic Ir is mainly attached to the basal planes of the rGO. These results confirm that we have synthesized an Ir-decorated reduced graphene oxide material where the Ir metal particles are small (< 2 nm) and well-dispersed, as is consistent with a previous study.[47]

2.3.3 Electrode Preparation and Nomenclature

Five different electrodes were studied and are reported using the following naming convention: XXXX/YYYY ZZZZ, where 'XXXX' is the active material (either Ir-rGO or Vulcan XC72 carbon black), 'YYYY' is the binder used (either PVDF or PTFE), and 'ZZZZ' is the final drying temperature used during the electrode preparation process (either 25 °C or 200 °C). To prepare electrodes in which PVDF was used as the binder, a homogenized slurry of active materials, binder, and NMP (active material to PVDF weight ratio of 50:50, 10 wt% solids in NMP solution) was evenly spread onto a P50 carbon paper substrate. To prepare electrodes in which PTFE was used as the binder, a homogenized slurry of active materials composed of a PTFE dispersion (60 wt% in H_2O), a 1:1 mixture of isopropanol: H_2O, and Ir-rGO (active material to PTFE weight ratio of 50:50) was spread onto a P50 carbon paper substrate.

Electrodes were then dried using one of two procedures: either by placing them in a fume hood at ambient conditions overnight (electrodes labeled ZZZZ = 25 °C), or by drying under vacuum at 110 °C overnight, quickly transferring them into a glovebox while still hot, and then placing them on a 200 °C hotplate for at least 1 hr prior to cell assembly (ZZZZ = 200 °C). No additional drying was performed on the 25°C electrodes, other than the short exposure to vacuum during antechamber transfer into the glovebox. As will be seen later, the difference in these drying procedures plays a critical role in the Raman spectra of analyzed

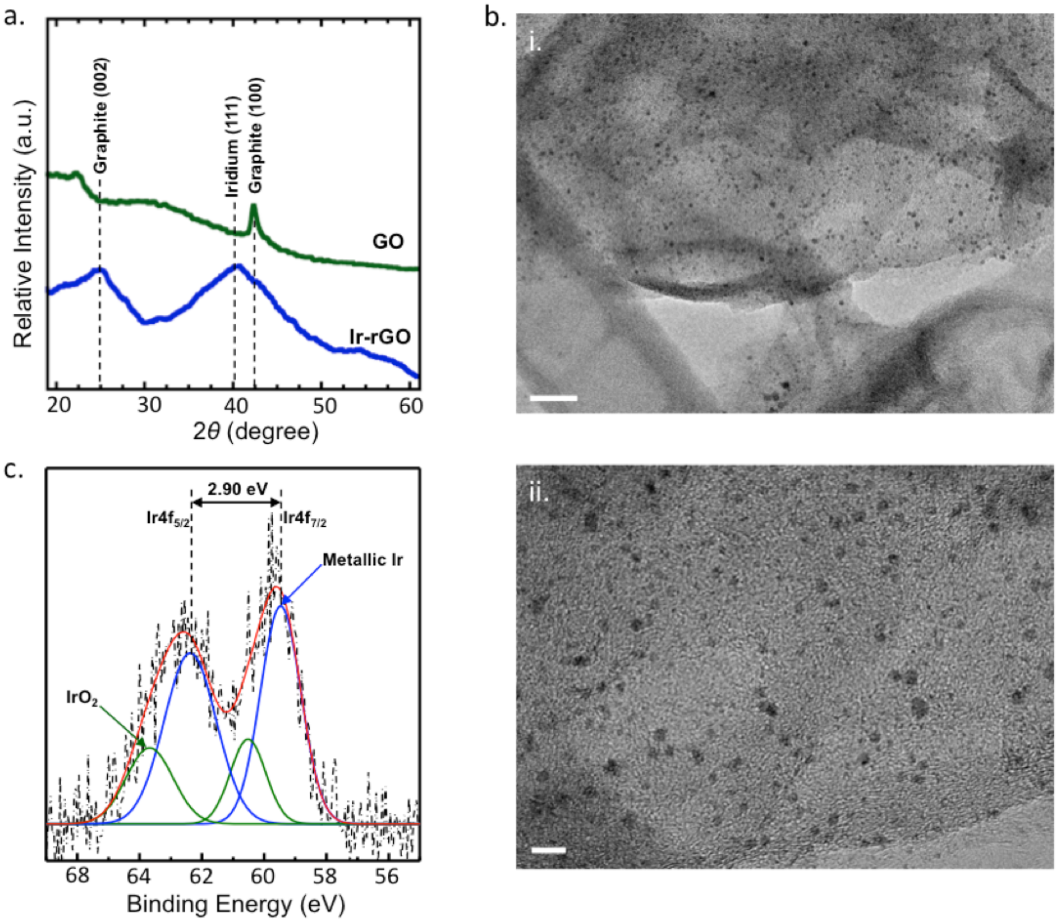

Figure 2.1: Ir-rGO composition characterization. a, PXRD results for rGO and Ir-rGO in which the broad peak centered on 40° is evidence of iridium metal formation. b, TEM images of the prepared Ir-rGO. Iridium nanoparticles are observed as the dark spots in the material. i) scale bar 20 nm; ii) scale bar 5 nm. c, XPS of the Ir-rGO material. Peak deconvolution confirms the presence of primarily metallic iridium on the reduced graphene oxide, with a small amount of IrO_2 also present.

discharged cathodes. Measured after drying, the electrodes had a typical active material (Ir-rGO or XC72) loading of 2 mg on 12 mm diameter electrodes.

2.3.4 Electrochemical Characterization

Electrochemical cells were assembled in a custom-built modified Swagelok-type cell,[57] with a lithium metal anode (7/16" diameter), 1 M lithium bis(trifluorosufonyl imide) (LiTFSI) in 1,2-dimethoxyethane as the electrolyte (80 μL), a glass fiber separator (QMA Whatman), and a cathode (12 mm diameter) backed with stainless steel mesh. Cells were then discharged and charged at a total current of 0.1 mA. Gas consumption and evolution during the electrochemical experiments were monitored using an established pressure decay/rise measurement. Differential electrochemical mass spectrometry (DEMS) was also employed to confirm the analysis provided by pressure monitoring and to quantify individual gases evolved.[57–59] These systems were leak checked by ensuring that the pressure remained stable while the cells were held at OCV (Figure 2.2). Well established iodometric titrations were also used to quantify Li_2O_2 formation during discharge.[40] Of note, no O_2 evolution was observed from electrodes immersed in water during the titration protocol, indicating any titrated H_2O_2 was formed from the dissolution of Li_2O_2 and not a reaction involving LiO_2 (O_2 evolution during this titration has been observed when characterizing sodium superoxide, NaO_2, formation in Na-O_2 batteries.[60])

2.3.5 Raman Characterization of Discharged Cathodes

Raman spectra of the discharged cathodes were acquired by use of a Witec alpha300 S confocal Raman microscope with a fiber-coupled laser operating at 532 nm. Samples were prepared for Raman by first disassembling the cells inside an argon filled glovebox, and then placing the cathodes in an air-tight spectroscopy cell. Prior to placing cathodes in the air-tight cells, any residual electrolyte solvent was evaporated from the cathodes using a vacuum antechamber. Typically 10% of the maximum 50 mW laser intensity was applied, with a collection time of 10-30 s.

2.4 Results and Discussion

A previous report indicated that bulk, stable lithium superoxide, LiO_2, forms on Ir-rGO based cathodes.[47] As LiO_2 forms via a 1 e^-/O_2 process (eqn 1) and Li_2O_2 forms via a 2 e^-/O_2 process (eqns 1,2 and/or 1,3), quantitative gas analysis coupled with coulometry was employed to help identify the possible discharge product. Quantification of oxygen consumption and evolution via online pressure monitoring from cells with Ir-rGO-based cathodes is presented in Figure 2.4. Regardless of binder employed or cathode preparation conditions, a nearly 2 e^-/O_2 process is observed throughout discharge: 2.00 ± 0.05 for the Ir-rGO/PVDF 200 °C cells, 2.01 ± 0.05 for the Ir-rGO/PVDF 25 °C cells, and 2.03 ± 0.05 for the Ir-

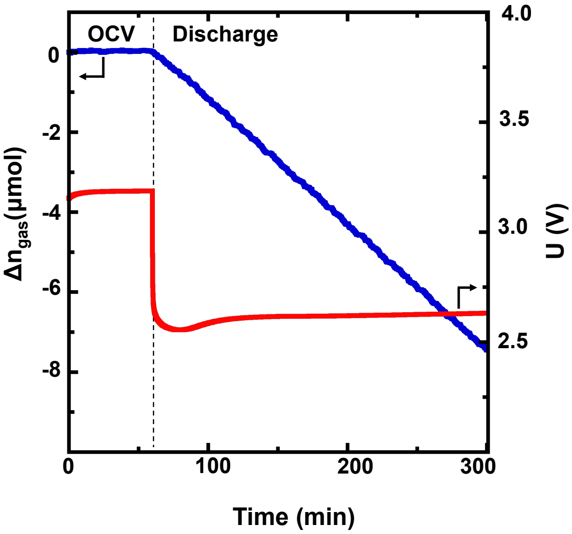

Figure 2.2: Voltage profile and pressure decay for an Ir-rGO/PVDF 200 °C cell. Pressure decay is observed to begin upon initial discharge after 60 minutes of OCV. The current used was 0.1 mA. The average gas consumption rate during discharge was 0.031 µmol/min, which corresponds to 2.0 e^-/O_2.

rGO/PTFE 25 °C cells. The 2 e^-/O_2 ratio is consistent with Li_2O_2 formation as the primary discharge product, although statistical variance in the O_2 consumption measurements may allow for the possibility of perhaps 1-2 mol% of the final product to be LiO_2.

Standard analysis of discharged cathodes via PXRD confirmed the expected presence of Li_2O_2 (Figure 2.3). To further demonstrate the presence of Li_2O_2 as the dominant discharge product, extracted cathodes were immersed in de-ionized water after a 0.5 mAh discharge and the resulting H_2O_2 was titrated using established protocol.

Li_2O_2 was found to form at a 94% yield in cells similar to those characterized in Figure 2.4a, d and 90% in cells similar to Figure 2.4b, e. In comparison, cells employing XC72/PVDF and XC72/PTFE cathodes exhibited 88% Li_2O_2 yield, consistent with previous reports.[40] The increase in Li_2O_2 yield when using Ir-rGO as a cathode material indicates that employing Ir-rGO as the cathode material reduces parasitic side reactions involving Li_2O_2 compared to pure carbon cathodes. This observation is somewhat surprising given iridium's ability to dissociate O_2, which could potentially induce additional parasitic reactions. Further study into this Li_2O_2 yield increase on Ir-rGO cathodes is recommended. Of note, no gas evolution was observed during the immersion in water of any of the discharged electrodes. This is an important finding, as it is expected that if LiO_2 were present in the

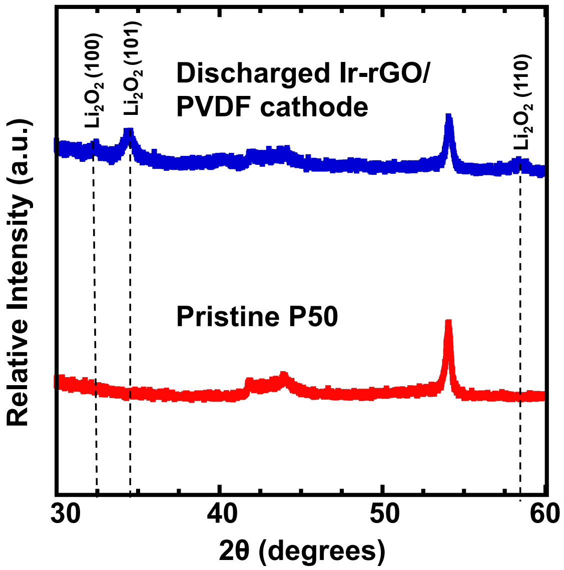

Figure 2.3: XRD pattern of discharged Ir-rGO/PVDF 200 °C cathode and pristine P50 carbon paper. The presence of lithium peroxide is observed for the discharged iridium decorated cathode.

discharged cathodes, it would disproportionate to H_2O_2 and O_2 in water in a similar fashion to the disproportionation reaction clearly observed when a similar quantity of NaO_2 is immersed in water.[60]

On charge, while each voltage profile is slightly different, the gas evolution from all cells studied is consistent with previous reports for Li-O_2 cells, namely an initial gas evolution rate close to what is expected (2 e$^-$/O_2 process), followed by a deviation away from a 2 e$^-$ process (to higher e$^-$/O_2 values) throughout charge.[41] This result was confirmed by DEMS analysis, which provided the identification and quantification of gases evolved during charge (Figure 2.5). In other words, at no point during a typical galvanostatic discharge-charge measurement was a 1 e$^-$/O_2 or a mixed 1 and 2 e$^-$/O_2 process observed in cells employing ether-based electrolytes and Ir-rGO-based cathodes.

Figure 2.6 presents the Raman spectra of cathodes extracted from cells after large capacity (10 mAh/cm^2) discharges. The appearance of two peaks at 1133 and 1525 cm^{-1} are highlighted given that similar peaks have been ascribed to LiO_2 formation previously.[47–50] Although these shifts do not precisely align with those reported in previous studies (1123 cm^{-1} and 1505 cm^{-1}), we suspect that differences in background subtraction could result in slightly different peak shifts, particularly given the large fluorescent background typically observed during initial illumination. Furthermore, background subtraction could more dra-

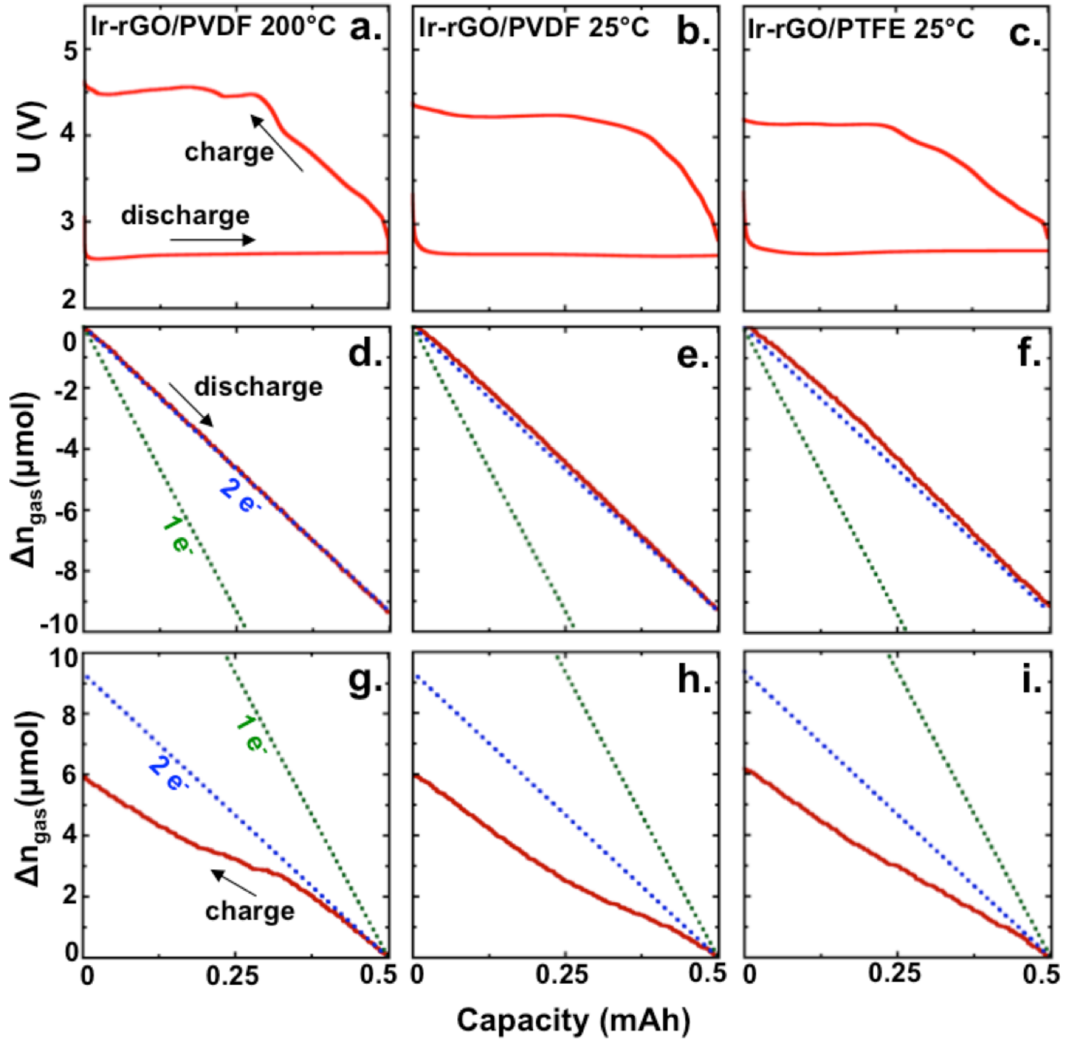

Figure 2.4: Voltage and gas consumption/evolution plots for Ir-rGO cathodes. a,b,c Galvanostatic discharge/charge curves. d,e,f Gas consumption during discharge under oxygen as measured by pressure decay in an isolated, volume calibrated headspace. g,h,i Gas evolution during charge as measured by pressure rise in the same headspace. Dashed blue and green lines in d.-i. are expected O_2 consumption/evolution profiles for a 1 e^-/O_2 and 2 e^-/O_2 process. Discharge/charge capacity: 0.5 mAh; current density: 0.1 mA; active material loading: 2 mg cm^{-2} (12 mm diameter cathode).

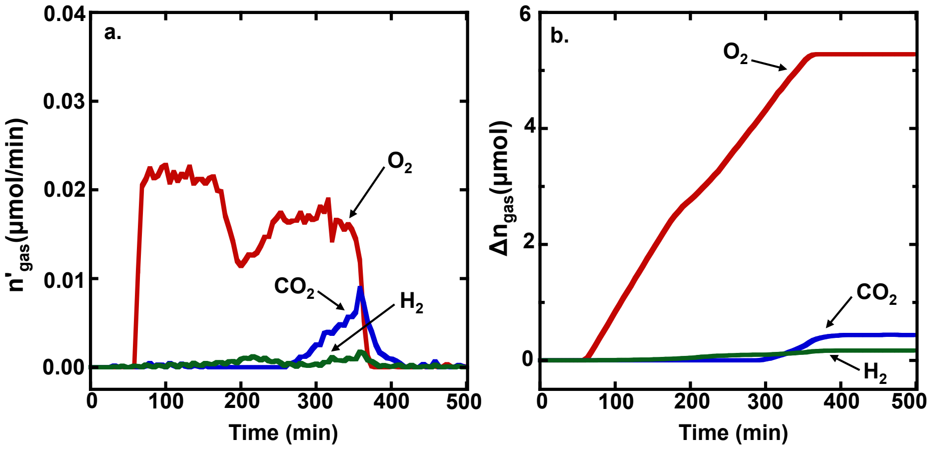

Figure 2.5: a, Gas evolution rates measured using DEMS for a Ir-rGO/PVDF 200 °C cell. 0.031 μmol/min corresponds to a 2 e^{-}/O$_2$ process given the charging current rate (0.1 mA). b, Cumulative gas evolution throughout charge for Ir-rGO/PVDF 200 °C cell as quantified using instrumental calibrations. The total oxygen evolution was measured to be 5.2 μmol, which corresponds to a greater than two electron process (9.3 μmol would correspond to a 2 e^{-}/O$_2$ process for a 0.5 mAh charge). Charging was initiated at 60 min and was halted at 360 min (0.5 mAh).

matically influence the peak at 1525 cm^{-1} given that it slightly overlaps with the carbon G-band (1590 cm^{-1}). It is worth noting that peak shifts of 1128 and 1520 ± 2 cm^{-1} were observed in 'uncontrolled impurity' studies (those discussed in the introduction that eventually led to the replacement of PVDF with PTFE as a binder). Importantly, these two peaks only appear in this study when PVDF is used as a binder, regardless of whether Ir-rGO or XC72-based electrodes are used. When PVDF-bound cathodes are only air-dried during preparation (i.e., Ir-rGO/PVDF 25 °C and XC72/PVDF 25 °C), the 1133 and 1525 cm^{-1} peaks are pronounced and ubiquitous after discharge. However, these peaks are not observed if cathodes are rigorously dried prior to cell assembly (Ir-rGO/PVDF 200 °C and XC72/PVDF 200 °C). Changing the binder to PTFE also eliminated the presence of these peaks, regardless of the cathode drying procedure (Ir-rGO/PTFE 25 °C). These results, in combination with the observed 2 e^{-}/O$_2$ process on discharge for all cells studied (Figure 2.4), indicate that the origin of the Raman peaks at 1133 cm^{-1} and 1525 cm^{-1} is related to a process involving PVDF degradation and not to the formation of stable LiO$_2$.

PVDF alkaline "treatment" to improve its surface hydrophilicity is very common and many previous reports show that such alkaline treatment causes changes in the PVDF surface structure.[61] We confirmed that hydroxyl-induced HF elimination from PVDF is the likely origin of the Raman peaks at 1133 cm^{-1} and 1525 cm^{-1}. PVDF pellets were placed in alkaline

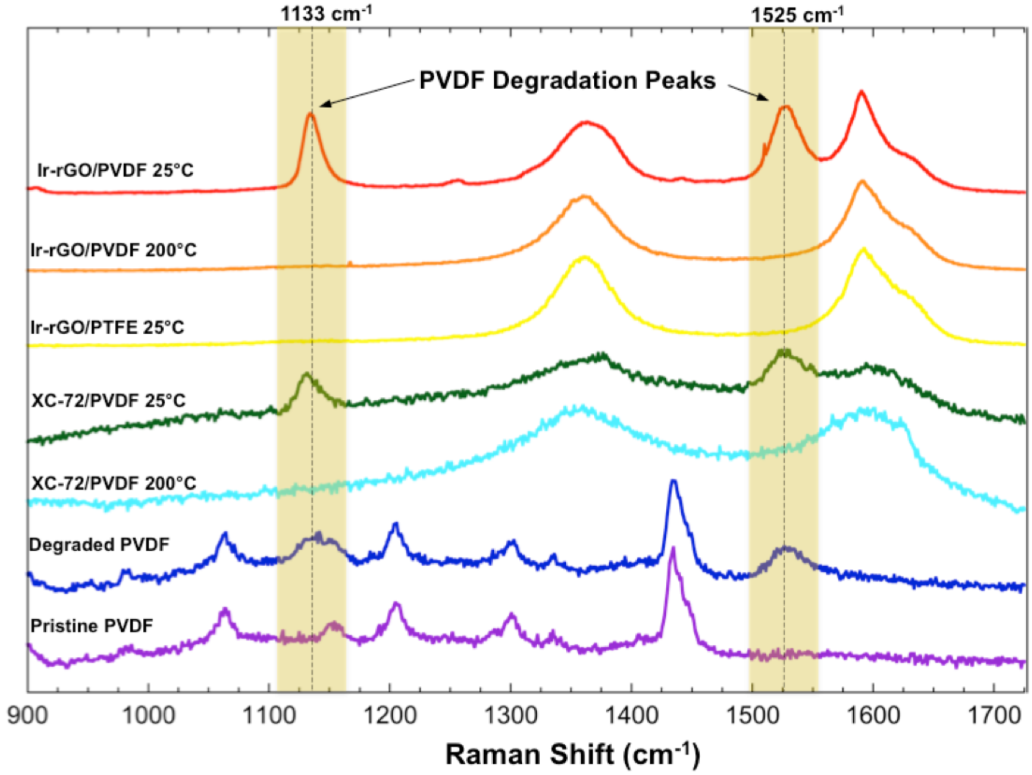

Figure 2.6: Raman spectra (excitation laser wavelength of 532 nm) of discharged electrodes as well as pristine and alkaline degraded PVDF pellets. Discharge/charge capacity: ∼ 10 mAh; current density: 0.1 mA, 12 mm diameter cathodes, ∼ 2 mg active material loading.

solution (12 M KOH) for 3 hours, rinsed, and then characterized using Raman spectroscopy. Peaks at 1133 cm^{-1} and 1525 cm^{-1} are clearly observed ('degraded PVDF' in Figure 2.6) as a result of a chemical change at the surface of the alkaline-soaked PVDF pellets (Raman spectra of pure PVDF pellets are also shown in Figure 2.6). These peaks have been previously ascribed to the formation of —(CH=CF)— species on PVDF's surface during OH- attack, with a C—C band at 1127 cm^{-1} and a C=C band at 1525 cm^{-1}.[29,62] Taken together, these observations present compelling evidence that the peaks previously ascribed to LiO_2 are in fact due to PVDF binder degradation when small water impurities are present in the cell. Note that in Figure 2.6 the pristine PVDF peaks are still present for the degraded sample because the depth of Raman sampling is larger than the thickness of the degraded surface layer on the PVDF pellets tested.

In the batteries tested, the cause of the degradation likely stems from the presence of water, NMP and possible debris on the electrode during preparation that then contributes to the formation of reactive soluble species in the battery. These reactive species then likely attack the PVDF to cause a change in chemical composition that is reflected in the Raman spectra. This degradation can be avoided by carefully preparing electrodes to remove and prevent the presence of water and slurry solvents (NMP). Of course, water impurities can also accumulate through degradation processes involving the electrolyte or electrode. In fact, we note that the 1133 cm^{-1} and 1525 cm^{-1} peaks are observed occasionally in isolated spots at the periphery of the rigorously dried Ir-rGO/PVDF 200 °C cathodes after discharge, presumably resulting from solvent degradation that results in the requisite reactive soluble species necessary to form products that result in these peaks. Due to these occurrences, any future studies that wish to explore the presence of superoxide-like species are encouraged to use alternative cathode binders instead of PVDF (e.g., PTFE).

2.5 Conclusions

In summary, this study showed that preparation technique and binder selection for Ir-rGO cathodes directly influence the Raman spectra observed upon discharge. A 2.0 e^-/O_2 processes was observed during discharge for all cells studied, as is consistent with Li_2O_2 formation. Li_2O_2 as the dominant discharge product is also supported by titrations performed on discharged electrodes. Charge gas evolution in all cells studied is consistent with previous Li-O_2 studies, in which a slightly higher than 2 e^-/O_2 process is observed initially, followed by a deviation to even higher values as charge proceeds. Despite the electrochemistry pointing towards Li_2O_2 as the major product, evidence of Raman peaks were found that were previously ascribed to LiO_2, although only in cells that employ PVDF as a cathode binder and where the cathodes are not rigorously dried. Of particular interest, these peaks can be found for both iridium decorated electrodes and ordinary carbon black electrodes. Slight compositional differences exist between cells studied here and those that reportedly resulted in LiO_2 formation previously: the preparation procedure of the Ir-rGO is not identical, DME (monoglyme) is employed here as an electrolyte solvent rather than tetraethylene glycol dimethyl ether (tetraglyme), and the experimental setups are dissimilar.[57,63] Nevertheless, these slight differences should not result in the dramatic difference in electrochemical behavior reported between these studies. Hopefully further investigation by others will continue to elucidate the cause of the product differences between this and other studies, but emphasize that any spectroscopic characterization absolutely needs to be confirmed with well-established quantitative analysis of gas consumption/evolution and product formation.

Chapter 3

The Role of Gas Evolution in Li-rich Li-ion Batteries

3.1 Abstract

The capacity of a Li-ion battery is limited by the specific quantity of reversible Li available for the intercalation process at the cathode, and a large amount of research has explored ways to increase or supplement the amount of reversible lithium that can be stored in an active material. One straightforward method is to synthesize the cathode material with a stoichiometric excess of lithium in the structure of a disordered rock salt. Originally, this disorder was believed to interrupt Li ion diffusion channels, which would limit attainable material capacity. However, sufficient Li excess has been discovered to allow adequate mobility throughout the active material particle bulk. There are a number of challenges associated with Li-excess caused by enhanced reactivity resulting from high degrees of lithium removal, most of which involve electrolyte degradation at the cathode-electrolyte interface. Gas evolution, especially O_2 evolution, results as Li^+ extracted at high states of charge begins to be compensated by irreversible oxygen oxidation instead of transition metal redox. The monitoring of oxygen oxidation through gas evolution measurements and titration techniques allows strategies for reducing the reactivity of these materials to be tested. Several techniques are explored in this chapter for examining and countering unwanted reactivity in Li-excess cathode materials. These include replacing oxygen content with fluorine and lowering the overall anion valence to aid in mitigating oxygen redox and undesired reactivity. Additional disordered rock salt cathode material compositions showing minimized oxygen evolution and increased stability are also discussed.*

---

*This chapter includes data and ideas with permission that are also utilized in the following publications: Lee et al. *Nat. Commun.* **2017**, 8, 1, 981; Lee et al. *Nature.* **2018**, 556, 7700, 185-190; Lun et al. *Adv. Energy Mat.* **2019**, 9, 2, 1802959

3.2 Introduction

The increasing demand for high density energy storage has led to the investigation of Li-ion cathode materials beyond the $Li_x(Ni–Mn–Co–Al)_{2\text{-}x}O_2$ (NMCA) compositional space.[64–66] NMCA materials have layered rock salt structures allowing for removal and intercalation of Li atoms that are charge compensated by Co or Ni redox.[67] Innovative cathode material research has been largely motivated by reducing Co content as it is expensive and environmentally hazardous.[68] Compounds with greater ratios of Ni or Al have become dominant in modern cathode chemistries, but the NMCA compositional space still provides only limited improvements over current NMCA materials.[68] Despite offering an abundance of options for incorporating new charge compensation mechanisms, disordered rock salt compounds – where instead of alternating Li and transition metal (TM) layers within the rock salt structure, Li and TMs have equal probability of occupying octahedral sites within the crystal lattice – were originally avoided as possible cathode materials as they were believed to have little electrochemical capacity due to very limited Li mobility.[66,69,70] Progress in disordered rock salt research has proven that sufficient lithium excess, where more Li is contained in the material than TMs on a molar basis, in these materials provides adequate Li ion mobility.[69] Additional redox centers including Mn^{2+}/Mn^{4+},[71] Cr^{3+}/Cr^{5+},[69] Mo^{3+}/Mo^{6+},[72] V^{3+}/V^{5+},[73] and many more are able to be incorporated into disordered rocksalt compositions, opening many possible options for increasing the energy density. The required Li excess in these materials has also necessitated the use of high valent transition metals, including Nb^{5+},[74] Sb^{5+},[75] Mo^{6+},[76] and Ti^{6+}[77] for stabilization purposes.

Despite the promise for additional energy capacity in Li-excess disordered rocksalt (LEX-RS) cathode materials, a number of challenges arise when they are used in place of layered transition metal oxides. One of these challenges is that due to the Li-excess, transition metal charge compensation alone often cannot account for the totality of Li removal.[65,66,70] The additional Li reduces the total transition metal content and, unless the transition metal can be oxidized through multiple oxidation states, creates the need for an additional charge compensator.[63] This introduces another issue: the Li-excess and cation disorder can create linear Li-O-Li configurations known to prevent hybridization of O 2p orbitals with TM orbitals.[70] This in turn causes high energy labile O 2p states that are more easily accessed for oxidation.[63,70] The large capacities exhibited by LEX-RS materials are then often partially compensated at the higher capacities by oxygen redox processes.[74]

The reversibility of oxygen redox has recently been a highly investigated area of research, but current results suggest oxygen redox is almost always accompanied by deleterious effects. The most common outcome of such oxygen redox is severe loss of oxygen during charge, often in the form of oxygen gas, that limits cyclability.[65,76,77] Early LEX-RS material candidates including Li–Ni–Ti–Mo, Li-Ti-Fe, and Li-Nb-M (M=Ni, Co, Fe) oxides all delivered high capacities that were largely compensated by oxygen redox, resulting in oxygen loss and large voltage hysteresis between charge and discharge.[66,70,76,78] Therefore, the mitigation of oxygen loss is critically important to improving the cycling performance of LEX-RS materials.

One effective strategy to reduce LEX-RS outgassing is to partially substitute oxygen with fluorine, an anion with a lower valence. This strategy is first investigated with a set of materials including $Li_{1.15}Ni_{0.375}Ti_{0.375}Mo_{0.1}O_2$ (LN15), $Li_{1.2}Ni_{0.333}Ti_{0.333}Mo_{0.133}O_2$ (LN20), and $Li_{1.15}Ni_{0.45}Ti_{0.3}Mo_{0.1}O_{1.85}F_{0.15}$ (LNF15).[79] The incorporation of fluorine and lowering of the average anion valence, enables an increase of (redox active) Ni^{2+} content per formula unit of the Li–Ni–Ti–Mo oxides. By increasing the Ni, and partially eliminating the need of oxygen redox based charge compensation, a large reduction in oxygen loss is observed. The investigated fluorinated (LNF15) compound displays greater capacity retention and less polarization than the similar unfluorinated compounds (LN15, LN20).[79]

Another aim of LEX-RS compounds is to minimize dependence on Co and Ni as charge compensators. While $LiCoO_2$ dominates mobile electronics and NMCs are largely used in the transportation sector, these materials are limited by resource constraints and energy density.[68] Ideally, elements like Fe or Mn that are cheap and naturally abundant would replace Ni and Co. Because transition metals that can exchange two electrons (e.g. Ni^{2+}/Ni^{4+} in NMC cathodes) greatly increase capacity, the Mn double redox Mn^{2+}/Mn^{4+} couple is of particular interest.[27]

While manganese is already used in cathode materials, it is primarily included in its Mn^{4+}, electrochemically inert, state.[80,81] Some early LEX-RS compounds, including $Li_{1.3}Mn_{0.4}Nb_{0.3}O_2$, utilize Mn^{3+} that only slightly contributes to the capacity forcing reliance on oxygen redox.[66] This chapter instead examines the use of the Mn^{2+}/Mn^{4+} redox couple that allows a large capacity without necessitating much oxygen redox.[71] In this method, manganese begins in the cathode in its 2+ state and is oxidized to 4+ on charge. This largely eliminates the often seen massive capacity loss on first charge that is presumed to result from irreversible oxygen loss.

The introduction of Mn^{2+} to a LEX-RS cathode structure is difficult as the lithium excess requires a high average transition metal valence.[69,82] It was shown that the Mn valence can be lowered by both introducing high valent transition metals (Nb^{5+} and Ti^{4+}) and by lowering the average anion valence by substituting fluorine for oxygen.[71] In this chapter, the compounds of this type examined are $Li_2Mn_{2/3}Nb_{1/3}O_2F$ and $Li_2Mn_{1/2}Ti_{1/2}O_2F$, which have a theoretical Mn^{2+}/Mn^{4+} redox capacity of 270 mAh g^{-1} and 230 mAh g^{-1}, respectively. The total capacity observed in these materials is slightly larger than these values (300 mAh g^{-1}), indicating that most Li extraction is expected to be compensated by Mn, but there is still a small amount of oxygen redox contributing to the observed capacity.[71]

A consequential consideration for LEX-RS cathode design is optimization of fluorine substitution levels to improve cycling performance. While small levels of fluorine substitution were found to mitigate severe oxygen loss,[79] a systematic study examining various amounts of fluorine substitution reveals a balance between cyclability and capacity. Therefore, materials were synthesized by collaborators that combined Mn^{3+}/Mn^{4+} redox and Nb^{5+} as charge compensators with fluorination to form Mn^{3+}-Nb^{5+}-based DRX oxyfluorides ($Li_{1.2}Mn^{3+}{}_{0.6+0.5x}Nb^{5+}{}_{0.2-0.5x}\ O_{2-x}F_x$, x = 0, 0.05, 0.1, 0.15, referred to as "LMNO," "LMF05," "LMF10," and "LMF15," respectively). Gas evolution from this series is also examined to determine the influence of fluorine substitution ratios on outgassing.

For all explored LEX-RS, gas evolution measurements alongside oxygen redox probing titration protocols aid in the elucidation of oxygen activity. The influence of fluorine substitution and anion valence lowering on oxygen outgassing can be clearly observed in outgassing results. The effects of incorporation of transition metals with high valence is also examined by these techniques, and the results gathered in this chapter clearly display the importance of gas evolution measurements for LEX-RS cathode design.

3.3 Experimental Methods

3.3.1 Material Synthesis

All materials synthesis was accomplished by collaborators (see abstract footnote), with final materials provided for outgassing analysis. The details of the synthesis methods are described briefly here. $Li_{1.15}Ni_{0.375}Ti_{0.375}Mo_{0.1}O_2$ (LN15), $Li_{1.2}Ni_{0.333}Ti_{0.333}Mo_{0.133}O_2$ (LN20), and $Li_{1.15}Ni_{0.45}Ti_{0.3}Mo_{0.1}O_{1.85}F_{0.15}$ (LNF15) were synthesized by dispersing the precursors in acetone and ball milling for 15 h.[79] The mixture was then dried, pelletized, and calcined at high temperature (750 °C for LN15 and LN20, 700 °C for LNF15) in air before cooling to room temperature and ground into powder. The precursors used for LN15, LN20, and LNF15 were Li_2CO_3, $NiCO_3$, TiO_2, MoO_2, and LiF.

For $Li_2Mn_{2/3}Nb_{1/3}O_2F$, Li_2O, MnO Nb_2O_5, and LiF were used as precursors. For $Li_2Mn_{1/2}Ti_{1/2}O_2F$, Li_2O, MnO, TiO_2, and LiF were used. For each of the materials, Li_2O was used in 10% excess to compensate for possible Li_2O loss during synthesis. Each of the materials were synthesized by loading an Ar-filled stainless steel jar with the respective precursors and ball milling (planetary ball mill, Retsch PM200) for 40 h at a rate of 450 rpm.[71]

The $Li_{1.2}Mn^{3+}{}_{0.6+0.5x}Nb^{5+}{}_{0.2-0.5x}O_{2-x}F_x$ (x = 0, 0.05, 0.1) compounds (LMNO, LMF05, and LMF10) used Li_2CO_3 (5% excess), MnO_2, Nb_2O_5, and LiF as precursors. The materials were synthesized by ball milling for 4 h at a rate of 300 rpm. After milling, the powders were pelletized and sintered at 1000 °C under an argon atmosphere for 7 h, and then quenched in argon atmosphere before being ground into powders.[83]

3.3.2 Electrode Preparation

LN15, LN20, and LNF15 cathodes were composed of active compounds, carbon black, and polymer binder in a weight ratio of 70:20:10. The active compounds and SUPER C65 carbon black were first shaker milled for 1 h using a SPEX 8000M Mixer/Mill. Polytetrafluoroethylene (PTFE) was then added and manually mixed into the powder using a mortar and pestle. Cathode films were then rolled inside an Ar-filled glovebox, and cathodes of ∼1 cm^2 were punched from the film.[79]

LMNOF and LMTOF cathodes were prepared by mixing the active material with SUPER C65 carbon black in a SPEX 8000M Mixer/Mill before adding PTFE and continuing to mix. The mixed powder was composed of active material, carbon black, and polymer binder at a ratio of 70:20:10. The mixture was then ground using a mortar and pestle, and then rolled into a thin film inside an Ar-filled glovebox. Cathodes of ∼1 cm^2 were then cut using a circular punch.[71]

LMNO, LMF05, and LMF10 cathode films were made by first shaker milling the active material with SUPER C65 carbon black for 1 h in argon atmosphere with a SPEX 8000M Mixer/Mill, followed by an additional 40 min shaking with the addition of PTFE. The weight ratio of the components used was 70:20:10 for the active material, carbon, and polyer binder respectively. The powders were then rolled into films inside a glovebox, and cathodes of ∼1 cm^2 were punched.[83]

3.3.3 Differential Electrochemical Mass Spectrometry and Electrochemistry

A differential electrochemical mass spectrometer (DEMS) was used to identify and quantify oxygen and carbon dioxide evolved during charging and discharging. The instrument was also used to monitor evolution of other compounds including fluorine gas. The custom-built DEMS and the cell geometry used was described in depth in previous publications.[41,57] The electrochemical cells used with the DEMS device were prepared in a dry argon glove box (<1 ppm O_2 and H_2O, MBraun USA, Inc.) using modified Swagelok design. 1 M $LiPF_6$ in 1:1 (volume ratio) ethylene carbonate (EC) and dimethyl carbonate (DMC) was used as the electrolyte, glass microfiber filters were used as separators, and Li metal foil was used as the counter electrode.

The assembled cells were charged under a static head of positive argon pressure (∼1.2 bar) after being appropriately attached to the DEMS. Throughout the charge, argon gas pulses periodically swept accumulated gases to a mass spectrometer chamber. The mass spectrometer absolute sensitivity had been calibrated for CO_2 and O_2, and therefore the partial pressures of these gases could be determined. The amount of CO_2 and O_2 evolved was then quantified based on the volume of gas swept to the mass spectrometer per pulse.

3.4 Results and Discussion

3.4.1 Mitigating Oxygen Evolution by Fluorine Substitution

Initial studies on the effect of fluorine substitution on oxygen activity were performed with three compounds: $Li_{1.15}Ni_{0.375}Ti_{0.375}Mo_{0.1}O_2$ (LN15), $Li_{1.2}Ni_{0.333}Ti_{0.333}Mo_{0.133}O_2$ (LN20), and $Li_{1.15}Ni_{0.45}Ti_{0.3}Mo_{0.1}O_{1.85}F_{0.15}$ (LNF15).[79] The rocksalt phase lattice parameters and particle sizes of LN15, LN20, and LNF15 were determined with X-ray diffraction (XRD) and scanning electron microscopy (SEM) respectively.[79] Particle sizes for the compounds were determined as ∼100 nm for LN15, ∼100 nm for LN20, and ∼180 nm for LNF15. Transmission Electron Microscopy (TEM) Energy Dispersive Spectroscopy (EDS) confirmed fluorine substitution in the bulk disordered lattice. LNF15 was also shaker milled to reduce particle size and resulted in S-LNF15 particles of roughly 50 nm in size. This, combined with ^{19}F solid state nuclear magnetic resonance spectroscopy (ssNMR) studies showing spectra for both LiF and LNF15, prove that fluorine substitution in a disordered rocksalt can be achieved in this manner.[79]

The electrochemical properties were assessed by cycling the materials at 20 mA g^{-1} between 4.8 and 1.5 V (Figure 3.1). Each material maintains similar first charge voltage profiles with LN20 demonstrating the highest charge capacity followed by LN15 and LNF15. Both LN15 and LN20 deliver high discharge capacities of around 200 mAh g^{-1}, but a large fraction of the discharge capacity is delivered at only 2 V. This is contrasted by the LNF15 discharge voltage profile that maintains a higher average voltage (∼3.2 V). The low voltage plateau for LN15 and LN20 has previously been assigned to the reduction of surface species including Ti^{4+} and Mo^{6+} that are made accessible by oxygen loss[76]. These materials also show large hysteresis between charge and discharge voltage profiles. The reduced voltage gap and lack of asymmetric discharge plateaus for LNF15 imply that fluorination decreases polarization and enables larger discharge capacities for similar materials. In addition, cycling experiments were performed on these materials as described in Lee et al.[79] that clearly show increased cyclability and capacity retention for the fluorinated LNF15 material.

To assess gas evolution from the LN15, LN20, and LNF15, differential electrochemical mass spectrometry (DEMS) measurements were performed (Figure 3.2). Here it is observed that the fluorinated compound (LNF15) releases significantly less O_2 gas than LN15 and LN20. During the charge to 4.8 V, O_2 gas evolution begins at ∼4.35 V for LN15 and LN20, but is delayed to above 4.5 V for LNF15. The total O_2 evolution for each material was LNF15 (0.09 μmol mg^{-1}), LN15 (0.30 μmol mg^{-1}) and LN20 (0.49 μmol mg^{-1}). The total O_2 evolved for each material corresponds to 2.3%, 3.5%, and 0.7% of the total lattice oxygen for LN15, LN20, and LNF15, respectively.

CO_2 evolution is also measured for LN15, LN20, and LNF15, and for each material it is observed at above ∼4.4 V. Outgassing of CO_2 follows the same trend as for O_2: LNF15 (0.05

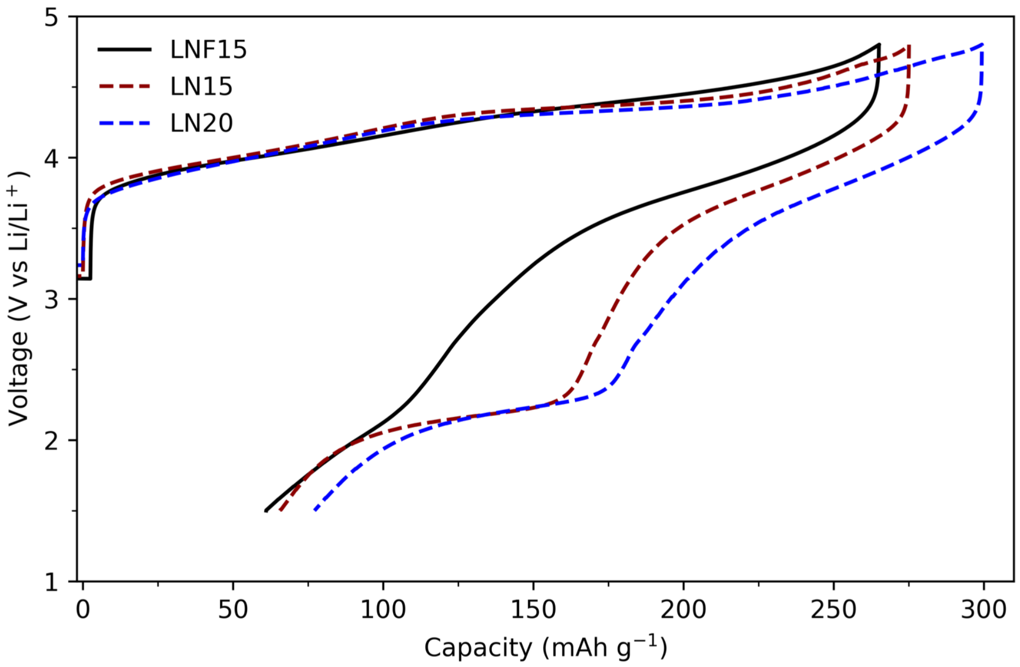

Figure 3.1: First cycle capacities for LNF15 (black line), LN15 (red dashed line), and LN20 (blue dashed line); current rate: 20 mA g^{-1}; active material loading: ∼9 mg/cm^2 (12 mm diameter cathode); binder: PTFE.

μmol mg^{-1}) exhibits significantly less CO_2 evolution than LN15 (0.14 μmol mg^{-1}) and LN20 (0.10 μmol mg^{-1}). The origins of CO_2 are debated, but possible sources of CO_2 outgassing include decomposition of residual carbonate species on the material as well as electrolyte degradation.[84,85] While carbonate titrations were not performed for LN15, LN20, or LNF20, titrations of similar materials reveal significant presence (∼1 wt%) of residual carbonates following synthesis.[71,86] A clear correlation between the quantity of O_2 and CO_2 outgassing appears from the results in Figure 3.2, indicating that some of the CO_2 outgassing may be related to oxygen evolution. It should be noted that for each of these materials, the outgassing follows a trend that is inversely related to the Ni content, as the fluorinated compound (LNF15) enables a higher Ni content. The DEMS measurements for S-LNF15 varied slightly from the trend, likely due to the smaller particle size (∼50 nm) (Figure 3.3).

Both CO_2 and O_2 outgassing was ∼0.11 μmol mg^{-1} during first charge of S-LNF15. While the CO_2 in this case is higher than LNF15, the major finding of reduced O_2 evolution with increased fluorination remains clear. This finding also confirms that the oxygen evolution is not merely an effect of particle size, but is instead primarily related to the TM and

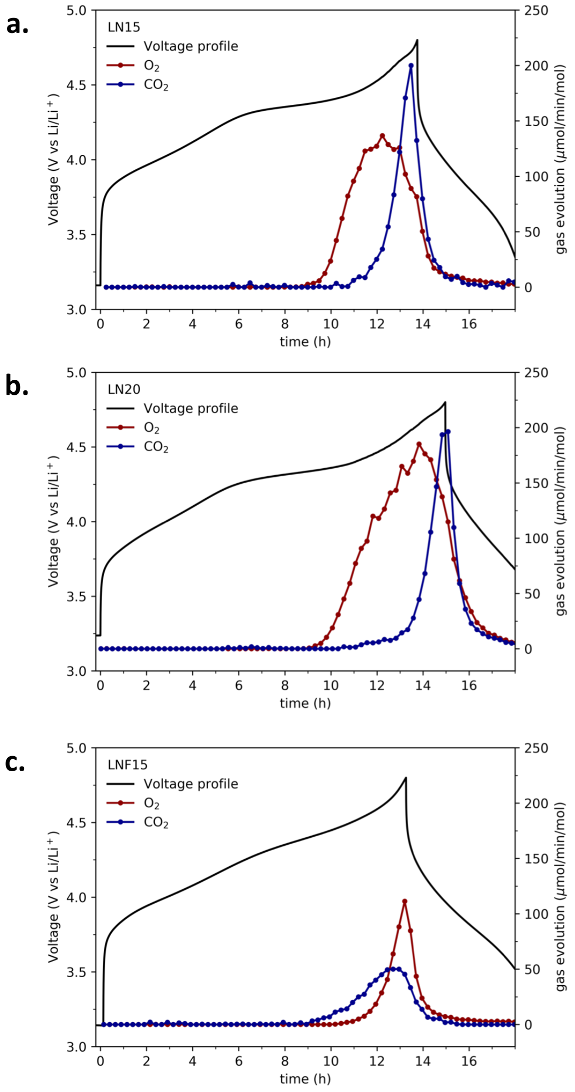

Figure 3.2: Differential electrochemical mass spectrometry (DEMS) O_2 and CO_2 evolution results for the first cycle (4.8-1.5 V) at 20 mA g^{-1} a) LN15, b) LN20, and c) LNF15.

anion chemistry. An additional finding when analyzing gas evolution was that there is no F_2 or other fluorine-containing gas evolution from LNF15 during cycling (Figure 3.4). Future studies to understand whether fluorine dissolution results in soluble species and other degradation products are suggested.

The gas evolution results support the hypothesis that fluorine substitution, and the increased Ni content the substitution allows, result in decreased oxygen loss from LEX-RS

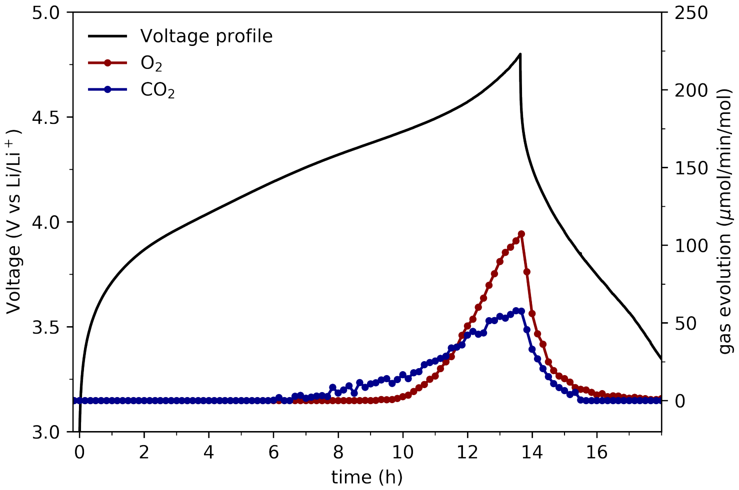

Figure 3.3: Differential electrochemical mass spectrometry (DEMS) O_2 and CO_2 evolution results for first cycle (4.8-1.5 V) at 20 mA g^{-1} of SLNF-15.

cathode materials with high capacities. Additional spectroscopic characterization was performed on these materials to elucidate structural changes and charge compensation mechanisms during electrochemical Li extraction and insertion, including in-situ XRD and soft X-ray absorption spectroscopy (sXAS).[79] XRD patterns for LN20 and LNF15 revealed that the lattice parameter for LN20 very slightly changes during a large section of the charge, supporting the DEMS results by suggesting oxygen loss from the material surface instead of lattice oxygen oxidation to form oxygen dimers, which would necessitate a large structural change in the crystal lattice. sXAS analysis confirmed partial utilization of the Ni redox reservoir for LNF15, and indicated that oxygen redox must contribute to the high capacity observed at the end of charge (i.e., at high degrees of delithiation). In summary, the small about of fluorine substitution did not effect the fractional utilization of the Ni redox reservoir, but did enable a higher total Ni content based on information gained from these additional techniques.[79]

The study of LN15, LN20, and LNF15 presented an important finding: small amounts of fluorine substitution in LEX-RS cathode materials mitigates severe oxygen loss while preserving high capacity.[79] The prevention of oxygen loss is beneficial as it leads to less cation densification at the particle surface and enables better cyclability. The reduced polarization for the LNF15 results in a higher and more beneficial average discharge potential, as well as increased cyclability. These findings opened many possibilities for a new class of fluorinated disordered rock salt materials that will be further studied in the following sections of this chapter.

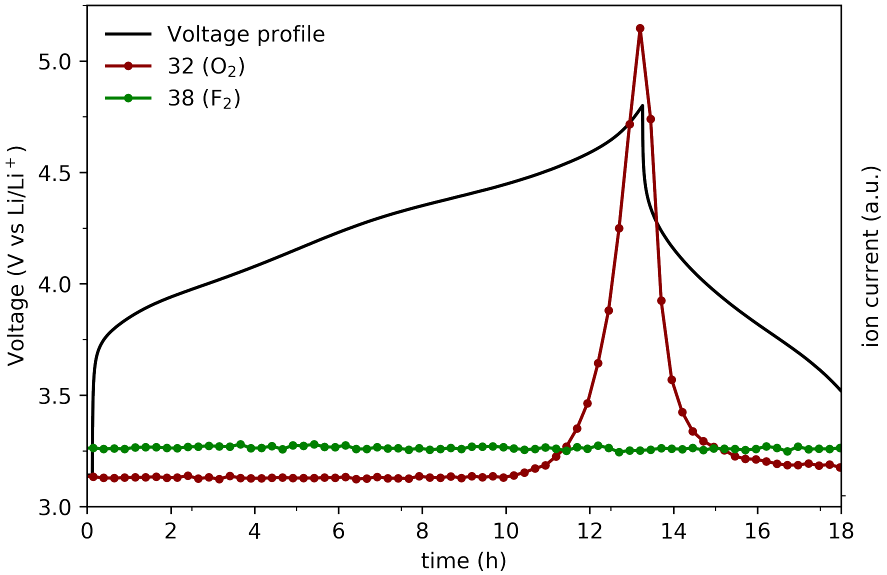

Figure 3.4: Differential electrochemical mass spectrometry (DEMS) raw ion currents results for masses 32 (O_2) and 38 (F_2) for the first cycle (4.8-1.5 V) at 20 mA g^{-1} of LNF-15.

3.4.2 Mn^{2+}/Mn^{4+} Double Redox

As high-energy-density cathode materials are explored, an important consideration is the minimization of the use of certain transition metals.[27] Nickel and cobalt are both limited resources and associated with a number of safety issues in lithium ion batteries.[68,80] The sourcing of cobalt has also been associated with numerous ethical concerns, not to mention it is the most expensive element in common cathode materials.[68] Manganese is a favored alternative to nickel and cobalt as it is low cost, naturally abundant, and provides great stability in the Mn^{4+} state.[27] Another possible benefit of manganese is the double redox available from Mn^{2+} to Mn^{4+}, providing additional charge compensation over the typical single redox in Co.

To explore the possibility of manganese double redox in a Li-ion battery cathode, manganese oxide based disordered rocksalt materials were synthesized by collaborators by a process combining high-valent cations and partial fluorination.[71] First, $Li_{1.333}Mn_{0.444}Nb_{0.222}O_{1.333}F_{0.667}$ (LMNOF) was synthesized by mechanochemical ball milling. This material enables the incorporation of Mn as Mn^{2+} by the combined effects of high valent Nb^{5+} and low valent F^-.[71,87] The Nb^{5+} also promotes the disordered rocksalt phase of the compound.[88] The Mn integration provides a theoretical Mn capacity contribution of 270 mAh g^{-1} in $Li_{1.333}Mn_{0.444}Nb_{0.222}O_{1.333}F_{0.667}$, a value that is almost twice that of a typical Mn based cathode material.[71] The material structure and composition was confirmed with

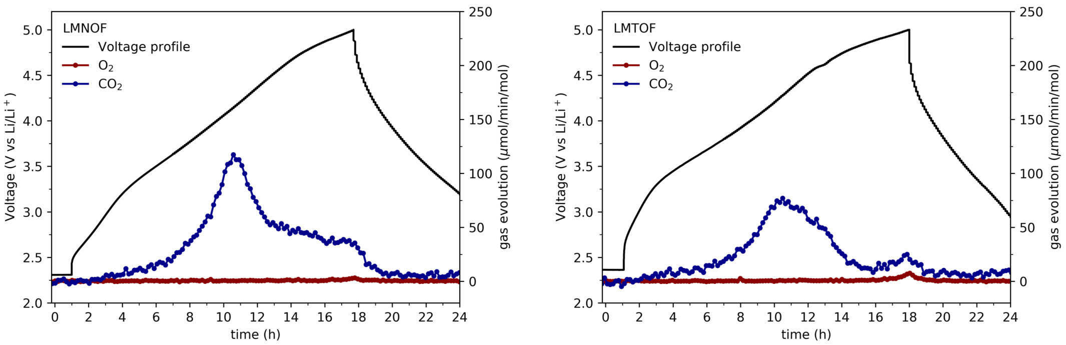

Figure 3.5: Differential electrochemical mass spectrometry (DEMS) O_2 and CO_2 evolution results for LMNOF and LMTOF.

XRD, TEM, and SEM as reported in the published study.[71]

The electrochemical performance of this material was established to provide 304 mAh g^{-1} at 20 mA g^{-1} between the voltage cutoffs 1.5-5 V, and 317 mAh g^{-1} when the rate was decreased to 10 mA g^{-1}. A capacity above 300 mAh g^{-1} for an intercalation material is significant and rarely observed for such materials.[89–91] When the cutoff voltage was reduced to 4.6 V, the discharge capacity was still 238 mAh g^{-1}. Of note, the voltage profile does not show significant hysteresis when cycling except when charging to at least 4.7 V.[71] The increased capacity above the theoretical Mn contribution (270 mAh g^{-1}), implies a least partial contribution by oxygen when the material is charged to a 5 V cutoff.[71]

To explore the effect of the choice of high valent cation, $Li_2Mn_{1/2}Ti_{1/2}O_2F$ (LMTOF) was also synthesized. In this material, Ti^{4+} acted as the high-valent cationic species and also promoted the disordered rocksalt phase as confirmed by XRD in the primary study.[71,88] $Li_2Mn_{1/2}Ti_{1/2}O_2F$ was determined to also deliver very high capacities close to those of $Li_2Mn_{2/3}Nb_{1/3}O_2F$, and in a cycling test between 1.5 V and 5 V yields reversible capacities of 259 mAh g^{-1} at 20 mA g^{-1}.

While both $Li_2Mn_{2/3}Nb_{1/3}O_2F$ and $Li_2Mn_{1/2}Ti_{1/2}O_2F$ deliver extremely high reversible capacities utilizing Mn double redox, the question of oxygen reactivity remains. As the capacities delivered with a high, 5 V charging cutoff exceed the theoretical Mn capacities, oxygen redox or parasitic reactions must play some role, as the 4+/5+ redox of the high valent transition metal is not expected to be accessible below 5 V. The influence of oxygen redox on instabilities in these materials is therefore important to determine, and gas evolution measurements by DEMS allow the observation of any instabilities resulting in gas release. In Figure 3.5, the gas evolution from LMNOF and LMTOF are compared.

Despite the large capacities extracted on charge from these materials, the key observation from the DEMS measurements was a clear lack of oxygen gas release. For both LMNOF and LMTOF less than 0.01 μmol O_2 mg^{-1} was released during the first cycle. CO_2 release observed in the DEMS measurements was modest (0.3 μmol CO_2 mg^{-1} for LMNOF and 0.24 μmol CO_2 mg^{-1} for LMTOF), and comparable to CO_2 evolution from conventional layered NMC transition metal oxides.[86] While the exact origin of the CO_2 outgassing was not further studied, as will be shown for similar materials in subsequent chapters, the CO_2 outgassing is subscribed to a combination of residual surface carbonate degradation, as well as electrolyte degradation at high potentials.[71] The gas evolution measurements provide evidence that the large capacity observed for LMNOF and LMTOF do in fact originate primarily from Mn^{2+}/Mn^{4+} double redox and that any oxygen redox participation does not result in dramatic oxygen loss and material degradation as seen in other materials with similarly high capacities, such as Li_2MnO_3 (to be discussed in later chapters).[71]

3.4.3 Improved Capacity Retention with Fluorine Substitution

The aforementioned studies have proven that disordered rocksalt cathode materials incorporating high valent cations and fluorine substitution demonstrate extraordinarily high capacities.[71,79] However, the optimization of lattice fluorine substitution and a clearer perspective on the impact of fluorine on capacity retention is lacking. Here a disordered rocksalt material, $Li_{1.2}Mn^{3+}{}_{0.6+0.5x}Nb^{5+}{}_{0.2-0.5x}O_{2-x}F_x$ (x = 0, 0.05, 0.1) is examined when substituting different ratios of fluorine.[83]

All materials were synthesized by collaborators via a single pot solid-state method using a Retsch PM200 planetary ball mill. The precursors were then pelletized and sintered at 1000 °C under argon. The structure was confirmed with XRD, and no long-range ordering or impurity peaks were observed.[83] The electrochemical performance was then tested using galvanostatic charge-discharge measurements between 1.5 and 4.8 V. The $Li_{1.2}Mn_{0.6}Nb_{0.2}O_2$ (LMNO) material delivered a discharge capacity of 238 mAh g^{-1}, while $Li_{1.2}Mn_{0.575}Nb_{0.175}O_{1.95}F_{0.1}$(LMF05) and $Li_{1.2}Mn_{0.55}Nb_{0.15}O_{1.9}F_{0.05}$ (LMF10) delivered higher initial discharge capacities of 272 mAh g^{-1} and 252 mAh g^{-1}, respectively. Cycling studies also revealed that fluorination greatly improved capacity retention as the LMF05 and LMF10 retain 84.3% and 92.4% of the initial capacities after 20 cycles compared with only 80.7% for LMNO.[83]

Gas evolution measurements utilizing DEMS support the improved stability of the fluorinated materials over their purely oxide analogs. Figure 3.6 presents the outgassing results for LMNO, LMF05, and LMF10 when charged to 4.8 V at 20 mA g^{-1}. It is observed that LMNO undergoes substantial O_2 outgassing (0.066 μmol mg^{-1}), while LMF05 has little O_2 release (0.005 μmol mg^{-1}) and any O_2 evolution during charge for LMF10 is undetectable. As previously discussed, the origin of oxygen release is likely from oxidized oxygen near the surface of the cathode.[63] These measurements indicate that additional fluorine lattice suc-

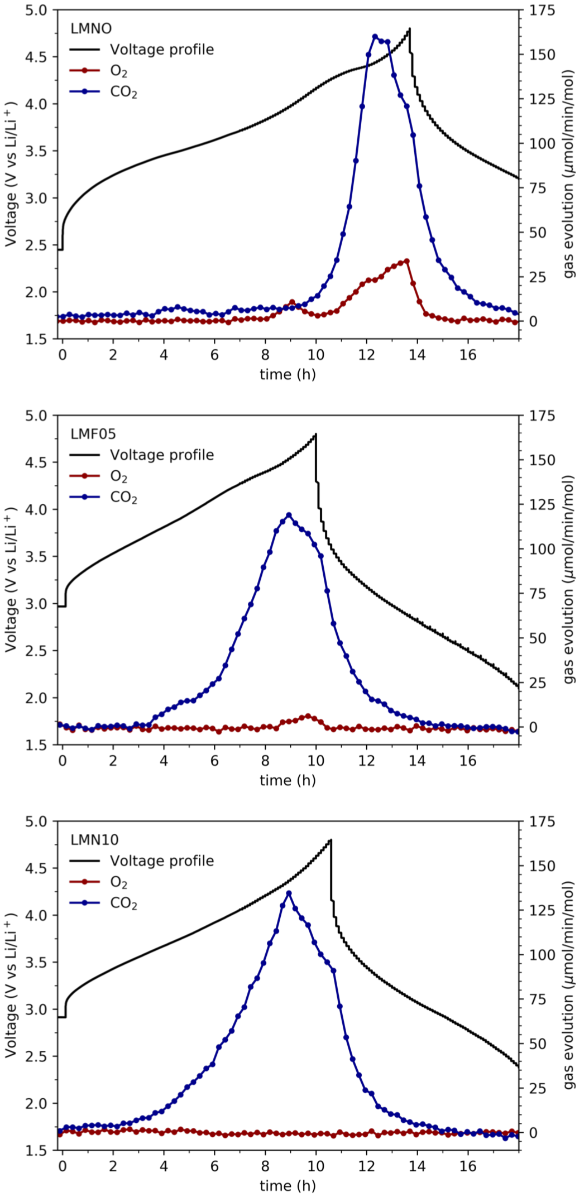

Figure 3.6: O_2 and CO_2 evolution studied using differential electrochemical mass spectrometry (DEMS) for a) LMNO b) LMF05 and c) LMF10. Current rate: 20 mA g^{-1}.

cessfully reduces the reliance on oxygen oxidation, instead shifting the charge compensation towards the active transition metal (Mn), thereby mitigating oxygen loss.

Each of the samples exhibits significant quantities of CO_2 outgassing when charged to 4.8 V. As was described previously, while the origin of CO_2 is convoluted, decomposed surface carbonate species (e.g. Li_2CO_3) likely accounts for a large portion of the observed release.[92] The remainder of the CO_2 likely originates from either lattice oxygen at the surface or electrolyte decomposition which is known to occur at voltages above 4.4 V. From these measurements, it is observed that the total CO_2 gas release slightly decreases as fluorination increases, although the onset voltage for CO_2 gas evolution is similar for LMNO, LMF05, and LMF10. A key difference is that high voltage evolution of CO_2 is much more prominent for LMNO, indicating a possible correlation between CO_2 and O_2 loss at high potentials.

Alongside a number of other techniques published in the full study,[83] the gas evolution measurements for LMNO, LMF05, and LMF10 aid to explain how successfully incorporating fluorine in disordered rock salt structures can increase energy density and improve capacity retention. Outgassing results clearly show decreased oxygen evolution with increased fluorine substitution and support a theory that fluorination shifts charge compensation away from oxygen redox and towards transition metal redox. The decreased oxygen loss, and decreased accompanying degradation of the cathode material, results in a much more useful material with greater capacity retention over many cycles. The encouraging results for LMF05 and LMF10 present possibilities for additional cathode material study incorporating high levels of fluorination.

3.5 Conclusions

This chapter presented studies centered on oxygen activity associated with Li-excess cathode materials, specifically disordered rock salt materials. These materials are shown to deliver extraordinary capacities, well above state of the art commercial materials. While Li-excess materials are often associated with a reliance on oxygen redox that results in poor capacity retention, the studies shown in this chapter propose alternatives to avoid oxygen reactivity. Fluorine lattice substitution along with incorporation of high valent cations were proven to be effective at not only promoting the rock salt structure,[88] but also mitigating the utilization of oxygen redox by reducing the average anion valence. This was shown to allow additional transition metal (Ni) incorporation and redox.

As transition metals like Co and Ni are not as cheap nor plentiful as Mn, this chapter also presented evidence that a Mn redox based lithium excess disordered rock salt material could deliver very high reversible capacities by utilizing the Mn^{2+}/Mn^{4+} double redox. In this case, fluorine substitution and high valent cations (Nb^{5+}, Ti^{4+}) facilitated the incorporation of Mn in its 2+ state and resulted in no significant oxygen loss. While CO_2 evolution was observed from nearly all materials studied, the total amount observed was small, with a major fraction likely being ascribed to residual surface carbonate oxidation. Deconvoluting CO_2 evolution mechanisms (carbonate oxidation, electrolyte degradation, and reactive oxygen release) will be a focus of ensuing chapters. Additionally, materials with higher levels of fluorine substitution were studied to determine the effects of oxygen activity and capacity retention. The mitigation of oxygen loss and the improved capacity retention seen in disordered rock salt materials with fluorine lattice substitution encourage continued study and open many possibilities in cathode material design.

Chapter 4

Quantifying the Capacity Contributions during Activation of Li_2MnO_3

4.1 Abstract

Though Li_2MnO_3 was originally considered to be electrochemically inert, its observed activation has spawned a new class of Li-rich layered compounds that deliver capacities beyond the traditional transition-metal redox limit. Despite progress in our understanding of oxygen redox in Li-rich compounds, the underlying origin of the initial charge capacity of Li_2MnO_3 remains hotly contested. To resolve this issue, differential electrochemical mass spectrometry combined with acid titrations were employed to reveal that O_2 and CO_2 release from electrolyte degradation products account for a large fraction of the observed capacity during the first charge. Spectroscopy results from collaborators at Binghamton and Lawrence Berkeley National Laboratory confirm that oxidation of Mn^{4+} and reversible oxygen redox do not contribute substantially to the charge compensation, with only minor contributions from reduced Mn species on the surface. These studies reveal that, although Li_2MnO_3 is considered critical for promoting bulk anionic redox in Li-rich layered oxides, Li_2MnO_3 by itself does not exhibit bulk oxygen redox or manganese oxidation beyond its initial Mn^{4+} valence.[*]

4.2 Introduction

Originally considered electrochemically inactive,[93] Li_2MnO_3 can deliver substantial capacity during charge, as demonstrated by Kalyani et al.[94] Later, Robertson and Bruce[95] revealed

---

[*] This chapter adapted with permission from previously published work in: J. Rana and J. K. Papp et al. *ACS Energy Lett.* **2020**, 5, 2, 634–641

how Li_2MnO_3 could be activated through the use of nanosized particles. And capacities exceeding 300 mAh g^{-1} have been reported during the first charge activation of Li_2MnO_3.[95–102] The large irreversible capacity observed during the first charge is primarily attributed to irreversible oxygen release,[65,70,73,103–105] which presumably activates lattice oxygen redox along with other degradation mechanisms, ultimately leading to severe capacity fade upon cycling.[95,96,98,99,106] Li-rich layered oxides (LR-NMC), derived from Li_2MnO_3 are often regarded as nanocomposites of Li_2MnO_3 and $LiMO_2$ (M = Ni, Mn, Co) components and exhibit a similar first charge activation plateau at 4.5 V vs Li/ Li^+.[64,103,107–109] In fact, a direct correlation observed between the 4.5 V plateau capacity and Li_2MnO_3 content of LR-NMC[110] has been used to quantify the extent of bulk oxygen redox in LR-NMCs.[111] Unlike Li_2MnO_3, LR-NMCs maintain stable cycling performance with high reversible capacities.[112,113] Meanwhile, lattice oxygen redox in LR-NMCs has been supported by numerous O K-edge resonant inelastic X-ray scattering (RIXS) studies,[63,114,115] with the recent beam exposure studies confirming that the RIXS feature is intrinsic to oxidized lattice oxygen.[116]

While Li_2MnO_3 is regarded as a model compound for describing bulk oxygen redox activity in LR-NMCs, recent RIXS studies did not detect similar spectroscopic signatures of oxidized lattice oxygen in Li_2MnO_3.[117] Additionally, an alternative scenario explaining the origin of anomalous capacity in LR-NMCs has been proposed by Radin et al.[111] According to this new perspective based on first-principle calculations, the reversible formation of molecular oxygen or peroxide ions in combination with Mn^{4+}/Mn^{7+} redox could explain the characteristic electrochemical behavior of LR-NMCs. Meanwhile, the appearance of O K-edge RIXS feature for numerous conventional Mn-free layered oxides questions the role of Li_2MnO_3 in activating lattice oxygen redox in LR-NMCs.[118,119] Additionally, oxygen and carbon dioxide evolution have been qualitatively observed from LR-NMCs in prior reports, highlighting the importance of understanding the role of irreversible surface processes (oxygen release and electrolyte degradation) on charge compensation. This study aims to answer the following two fundamental questions regarding the charge compensation mechanism during delithiation of Li_2MnO_3: (1) should Li_2MnO_3 be regarded as a model compound describing anionic redox activity and (2) what charge compensation mechanisms explain the electrochemical activity of Li_2MnO_3?

To resolve these issues, all possible charge compensation mechanisms including bulk oxygen redox, Mn^{4+}/Mn^{7+} redox, and surface degradation are considered. This investigation, in collaboration with colleagues at SUNY-Binghamton and LBNL, employed a combination of spectroscopic techniques sensitive to oxygen oxidation (O K-edge RIXS) Mn oxidation (operando Mn K-edge X-ray absorption spectroscopy (XAS)) and gas evolution (differential electrochemical mass spectroscopy (DEMS)). Importantly, it was found that gas evolution (O_2 and CO_2) almost entirely accounted for the observed capacity during the first charge activation, with minor contributions from lattice oxygen redox, carbonate decomposition, and oxidation of reduced Mn species on the surface. In support of this finding, no significant evidence of Mn^{7+} and/or oxidized lattice oxygen were observed by X-ray spectroscopy, although surface carbonates were found to form after immersing the pristine Li_2MnO_3 powder in the electrolyte. These surface carbonates then oxidize upon charge to evolve the observed CO_2. Despite being considered critical for understanding bulk oxygen redox activity in LR-NMCs, the parent Li_2MnO_3 itself does not exhibit this exotic charge compensation mechanism. Instead, irreversible oxygen release and electrolyte degradation during activation likely paves the way for further degradation on subsequent cycles, which will be discussed in Chapter 5.

4.3 Results and Discussion

Figure 4.1a shows the XRD pattern of the as-synthesized Li_2MnO_3, where all reflections can be indexed in the monoclinic system with the space group C2/m.[120] In the layered structure of Li_2MnO_3, the interslab octahedral sites are occupied by Li^+ only, while the octahedral sites within the $[Li_{1/3}Mn_{2/3}]O_2$ slabs are ordered with Li^+ and Mn^{4+} in a ratio of 1:2, which is indicated by the superlattice reflections in the 2θ range from 20 to 34°. However, these superlattice reflections appear convoluted into a broad asymmetric peak as highlighted in Figure 4.1a. Previously, the intensity and asymmetry of these super-lattice reflections were correlated with the degree of disorder in the stacking sequence of $[Li_{1/3}Mn_{2/3}]O_2$ slabs along the c- direction of the monoclinic lattice.[121] Moreover, the SEM micrograph of the as-synthesized material in Figure 4.1b reveals the agglomerated primary particles of less than 100 nm in size. Thus, the observed asymmetric superlattice reflection in the XRD pattern confirms an increased degree of stacking faults in the nanocrystalline Li_2MnO_3 synthesized in the present study. Figure 4.1c demonstrates the voltage profile of Li_2MnO_3 in the first cycle at a rate of C/50 (1 C = 230 mA g^{-1} assumed). A very large capacity (360 mAh g^{-1}) is observed during charge to 5 V, whereas a much lower discharge capacity is observed (180 mAh g^{-1}). This large difference between charge and discharge capacities is a characteristic electrochemical feature of Li_2MnO_3, and the general consensus is that the difference is due to irreversible oxygen release.[65,73,103–105]

While the irreversible component of the first cycle capacity could be attributed to gas evolution,[65,73,103–105] no definitive data exists that conclusively confirms this hypothesis. While quantitative gas evolution data will be presented shortly, spectroscopic work performed by collaborators will first be discussed to place the confusion regarding charge compensation mechanisms in Li_2MnO_3 into context. Besides irreversible degradation processes, only two possible sources of reversible charge compensation mechanisms exist: oxidation of Mn^{4+} and/or lattice oxygen redox.[111] Both can be probed using various X-ray spectroscopies. O K-edge XAS and RIXS are used to probe bulk redox activity of oxygen anions in Li_2MnO_3. Figure 4.2a shows the O K-edge spectra in the bulk sensitive total fluorescence yield (TFY) mode for the pristine Li_2MnO_3 and electrodes charged to 5 V vs Li/Li^+. Corresponding RIXS maps for the charged electrodes are shown in Figure 4.2b,c. The pre-edge peaks at 529.6 and 531.9 eV are attributed to the hybridization of Mn 3d–O 2p orbitals into t_{2g} and e_g states.[122] At these excitation energies, RIXS maps show two broad density of state (DOS)-

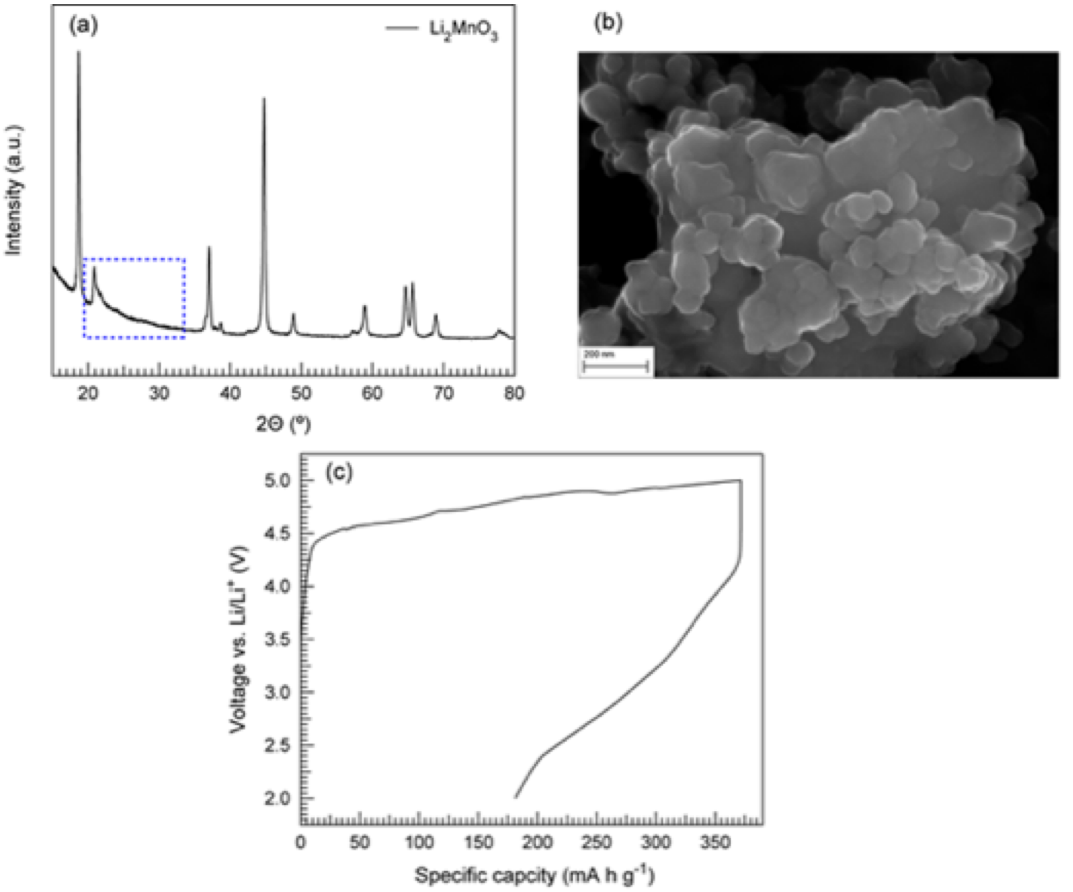

Figure 4.1: Structure and electrochemistry of Li_2MnO_3. (a) XRD pattern and (b) SEM image showing particles morphology of Li_2MnO_3 synthesized at 600 °C. (c) The first cycle voltage profile in a coin half cell (i.e., Li metal is used as the anode).

like features that are associated with the hybridized Mn–O states. The emergence of RIXS loss feature at 523.5 eV due to X-ray absorption at 531 eV is regarded as a spectroscopic signature of bulk oxygen redox activity.[114,115,118,123] The RIXS maps show no evidence of this feature for the charged electrodes, matching a recent Li_2MnO_3 study,[117] which rules out substantial bulk oxygen redox activity in Li_2MnO_3. The increased weight observed at 531 eV in the O K-edge XAS correlates with broadening of the hybridized t_{2g} and e_g states in the corresponding RIXS maps (Figure 4.2b,c).

These results are further complemented by a quantitative measure of oxide oxidation using an acid titration of extracted Li_2MnO_3 cathodes. Previous studies on NMC cathode materials have found that O_2 evolves from partially delithiated cathodes when exposed to water if oxygen redox participated in charge compensation. The oxygen evolved from these electrodes is closely related to the well established titrations of lithium peroxide,[86] following the reaction:

$$Li_2O_2 + H_2O \rightarrow 2LiOH + 1/2O_2 \tag{4.1}$$

Therefore, to quantify oxidized oxygen in a state similar to that in Li_2O_2, titrations were used with electrodes extracted at various states of charge (SI Table 4.2). An indication of the degree of “reversible” oxygen redox was estimated by comparing electrodes extracted at the top of the first charge and the bottom of the first discharge. Here it was found that these titrations demonstrate minimal contributions from bulk oxygen redox (only 10 mAh g^{-1}), which is in agreement with the lack of spectroscopic feature corresponding to oxidized oxygen in the RIXS measurements (Figure 4.2b,c).

Operando Mn K-edge XAS was used to probe bulk Mn redox activity in Li_2MnO_3 involving Mn^{4+}/Mn^{7+} redox as proposed by Radin et al.[111] However, the experimental verification of the proposed Mn^{4+}/Mn^{7+} redox is considered to be extremely challenging due to fragility of Mn^{7+} under X-ray irradiation.[111] Synchrotron XAS data of $KMnO_4$ was collected to inspect the susceptibility of Mn^{7+}-containing oxides to beam damage. Experimental data could successfully reproduce all major spectral features predicted by calculations from the Materials Project (SI Figure 4.4).[124] Furthermore, the Mn K- edge XAS data of $KMnO_4$ (SI Figure 4.4) are consistent with those reported by others.[97,125,126] These indicate that Mn^{7+}, if present, would be experimentally detected in operando XAS experiments. Notwithstanding this and as an added safeguard, the pouch cell was cycled off-line and exposed to X-rays for data collection only at the predetermined states of charge/ discharge, instead of continuously acquiring data by irradiating the cell throughout the entire charge/discharge cycle.

Parts d and e of Figure 4.2 show operando Mn K-edge X-ray absorption near-edge structure (XANES) and extended X-ray absorption fine structure (EXAFS) data of Li_2MnO_3. At 5.0 V, no clear shift of the main edge beyond that of the pristine state is observed, which rules out the oxidation of Mn^{4+}. The splitting of Mn 3d orbitals into t_{2g} and e_g levels by an octahedral field of the surrounding oxygen can be seen in the pre-edge region, which becomes more intense upon charging to 5.0 V. Meanwhile, reduction in the amplitude of

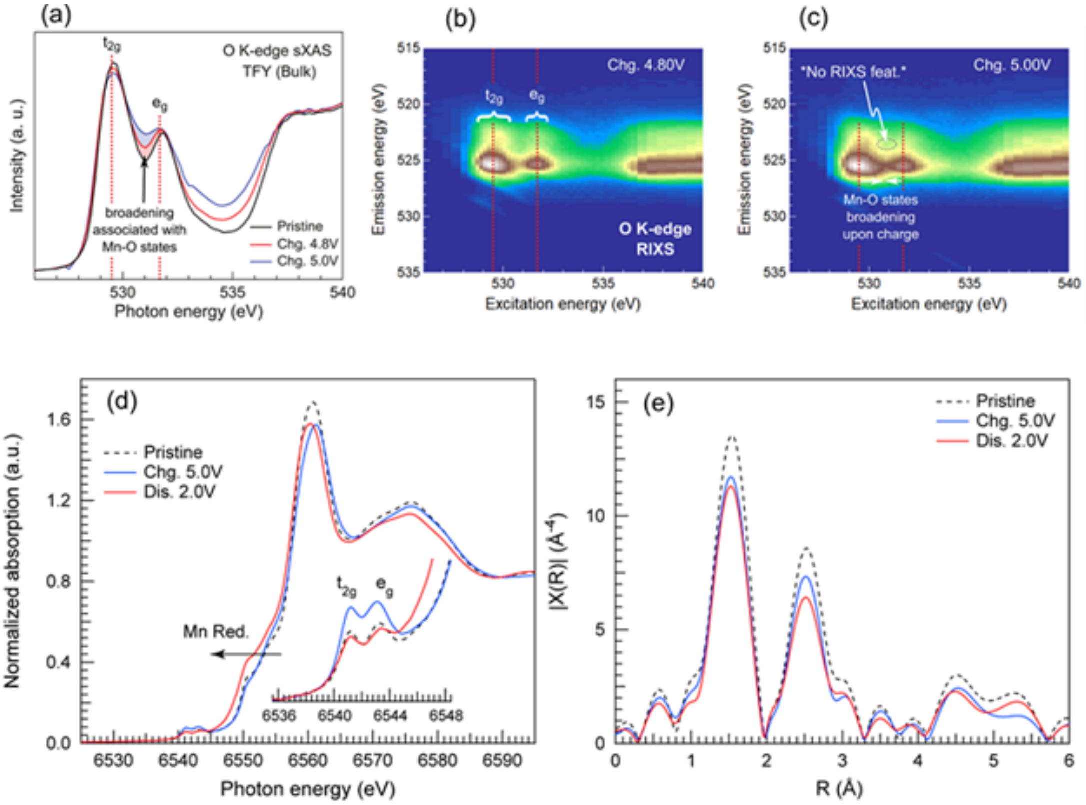

Figure 4.2: Bulk O and Mn redox activity in Li_2MnO_3. O K-edge TFY XAS data (a), and RIXS maps of Li_2MnO_3 electrodes charged to 4.8 V (b) and 5.0 V (c). Operando Mn K-edge XANES (d) and EXAFS (e) data for charged and discharged states during the first cycle.

the EXAFS signal observed upon charging to 5.0 V corresponds to increased disorder in the system.[97,102] Indeed, the observed increase in the intensity of the pre-edge region can now be correlated to major restructuring during activation. This restructuring also likely accounts for the observed broadening of the O K-edge spectral features in Figure 4.2a–c.[127,128] Upon discharge to 2.0 V, the main edge shifts slightly toward lower energy with respect to that of the charged state, which indicates reduction of Mn^{4+} during lithium reinsertion. To further clarify these trends, the investigation was extended to the second cycle. Similar trends are observed for the charged/ discharged states of the second cycle (see SI Figure 4.5), except that the second discharge shows even more reduction of Mn^{4+} than the first discharge. These results are in direct agreement with those reported by Croy et al.[102] and confirm that Mn does not oxidize beyond the 4+ oxidation state during charge but undergoes reduction during discharge. These reduced Mn species would then be oxidized during Li extraction on subsequent charge.

Without oxidation of Mn^{4+} and/or reversible participation of lattice oxygen in charge-compensation processes, the remaining possibilities for charge compensation are irreversible processes involving electrolyte degradation and oxidation of lattice oxygen to oxygen gas. DEMS was employed to monitor gas evolution from Li_2MnO_3 during the first charge (Figure 4.3a). Upon application of current, CO_2 was immediately detected, which quickly rose to a sharp peak in evolution rate. As the voltage plateau region was reached, oxygen gas became the dominant evolution product, though CO_2 continued to evolve at a lower rate. Total gas evolved across the first charge summed to be 38 mmol of CO_2 per mol of active material and 113 mmol of O_2 per mol of active material. Note that higher applied currents (20 mA g^{-1}) during DEMS experiments due to instrument availability, as well as variation in the cell design, led to the decreased first charge capacity of 177 mAh g^{-1} compared to the data in Figure 4.1c.

The source of oxygen gas is the formation of oxidized lattice oxygen species followed by gas evolution,[73] as no O_2 evolution results from electrolyte degradation or carbonate oxidation.[86] O_2 evolution from the oxide lattice is a 4 electron process, such that the irreversible oxygen contriubtion to capacity can be calculated from the total oxygen evolved as 125 mAh g^{-1} , or 71% of the total first charge capacity. This oxygen evolved on the first charge accounts for 9.1% of the total oxygen present in the pristine active material. After an initial delay, oxygen evolution proceeds at a rate near that of 4 electrons per molecule oxygen gas released. A 4 electron process involving molecular oxygen would require an oxygen gas release rate of 363 μmol min^{-1} mol^{-1} if oxygen gas accounted for the entire first charge capacity, as is denoted by the dotted red line in Figure 4.3a.

Note that the CO_2 evolution is remarkably high for a transition metal oxide material. The large quantity of CO_2 evolved (Figure 4.3c) could originate from a variety of mechanisms, including electrolyte reaction with generated singlet oxygen,[129] surface peroxo species at high voltages, or the oxidation of carbonate impurities in the as-prepared material. To understand the origin of CO_2 evolution, acid titrations and X-ray photoemission spectroscopy (XPS)/hard X-ray photoemission spectroscopy (HAXPES) studies were performed on the extracted electrodes. Acid titrations revealed the presence of 0.4 wt% (6.2 mmol mol^{-1}) of carbonates in the pristine material used for the DEMS study, which is much lower than the total CO_2 evolution observed during galvanostatic charge (38 mmol mol^{-1}). This suggests that electrolyte degradation is the dominant contributor to CO_2 evolution. Interestingly, a titration study on a separate batch of Li_2MnO_3 electrodes both in its pristine state and after simply immersing it in electrolyte revealed that carbonate content increased by 69% (SI Table 4.3) as a result of exposing the material to the electrolyte, indicating that the electrolyte largely decomposes and deposits a solid degradation product on the material surface. This is consistent with the XPS O 1s region of the pristine material (Figure 4.3b) showing a peak between 531.5 and 534 eV binding energy due to the formation of surface carbonates.[130–134] Note the absence of a similar peak in the bulk sensitive HAXPES O 1s region of the pristine material. Meanwhile, Mn L_3-edge TEY XAS data reveal the presence

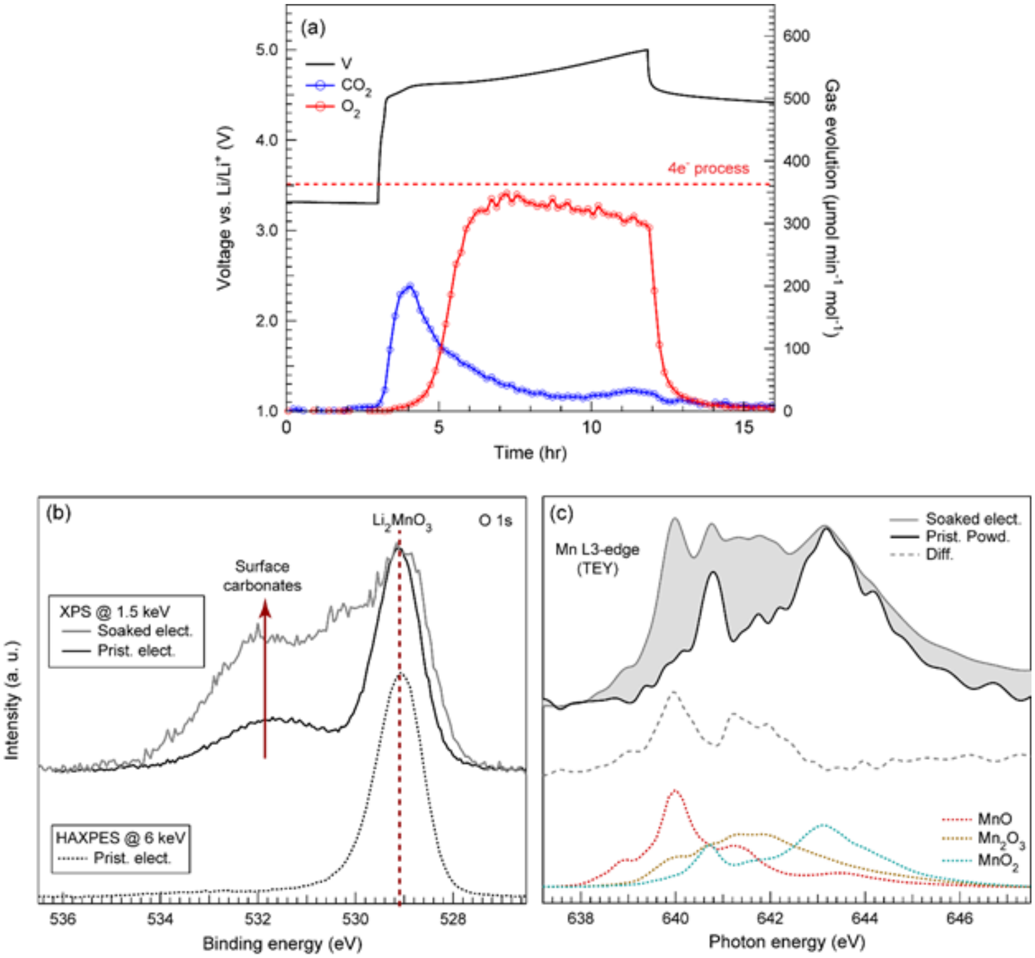

Figure 4.3: Gas evolution and surface studies of Li_2MnO_3. (a) DEMS for the first charge and (b) XPS/HAXPES data and (c) Mn L3-edge TEY data for the pristine and electrolyte-soaked material.

First Charge Capacity Contributions	
gas evolution	
O_2	125 mAh g^{-1}
CO_2	17 mAh g^{-1}
"reversible" oxygen redox (OR)	10 mAh g^{-1}
(O_2 + CO_2 + OR)/electrochemistry total	152/177 mAh g^{-1}
other contributions	25 mAh g^{-1}

Table 4.1: Capacity contributions as determined using gas evolution and titration techniques compared to the total first charge capacity of the cell run on the DEMS system.

of reduced Mn species on the surface of pristine material (Figure 4.3c). The amount of surface carbonates and reduced Mn species greatly increased once the electrode is exposed to the electrolyte (Figure 4.3b,c), which can be attributed to higher surface reactivity of Li_2MnO_3.[135] It is this chemical process that may be the dominant electrolyte degradation mechanism throughout the first charge, although future studies employing isotopic labeling and $^1O_2$ detection are needed to fully understand electrolyte degradation. Nevertheless, the results strongly suggest that the predominant origin for CO_2 evolution is the continuous degradation of the electrolyte to solid surface species, which then oxidize at high voltages to evolve CO_2.

The first charge capacity for Li_2MnO_3 as observed during the DEMS measurement can now be analyzed in terms of the contributions from the processes examined in this study (Table 4.1). O_2 evolution originating from oxygen oxidation accounts for roughly 70% of the total charge capacity. CO_2 evolution originating from the decomposition of carbonates both present in the initial material as well as formed by electrolyte decomposition accounts for another 10% of the charge capacity. Titrations probing the "reversible" oxygen oxidation (O_2^{-1}/O^{-1}) revealed about 6% contribution to the total charge capacity. The remaining 14% of the first charge capacity (Table 4.1) likely results from a combination of processes including electrolyte decomposition given the high cutoff voltage, as well as the oxidation of reduced Mn species in the near surface region (Figure 4.3c). Electrolyte decomposition was regarded as a likely source of protons for the previously proposed Li^+/H^+ exchange in Li_2MnO_3.[95,97,136] However, like those previous studies, the X-ray techniques employed in the present study are not directly sensitive to structural protons. Meanwhile, a recent NMR study by Dogan et al.[99] found significant evidence for proton-containing species on the surface of the charged electrode due to side reactions but ruled out insertion of structural protons in Li_2MnO_3.

4.4 Conclusions

In summary, using the combination of operando Mn K-edge XAS, O K-edge RIXS, XPS, and DEMS, the capacity contributions observed during electrochemical activation of Li_2MnO_3 are interpreted and quantified. Taken together, the first charge capacity of Li_2MnO_3 originates primarily from oxygen release, with much smaller contributions from reversible lattice oxygen redox, decomposition of surface carbonates and oxidation of reduced Mn species on the surface. Furthermore, these results conclude that Li_2MnO_3 does not exhibit the recently proposed Mn^{4+}/Mn^{7+} redox. For Li_2MnO_3, the octahedrally coordinated Mn prefers not to oxidize beyond 4+ at high voltages consistent with the lack of Mn^{7+} signatures in delithiated LR-NMCs reported thus far. Interestingly, Ceder and co-workers[70] attributed bulk oxygen redox to the labile oxygen states resulting from the Li–O–Li correlations as in Li_2MnO_3. However, the lack of RIXS feature in the charged samples clearly ruled out significant contribution from bulk oxygen redox in Li_2MnO_3. In contrast, the conventional layered oxides without Li–O–Li correlations demonstrated a RIXS feature indicating the onset of bulk oxygen redox at higher degrees of delithiation.[118,119,137] These reports suggest that increased covalency afforded by highly oxidized Ni and Co ions is an important precursor to promoting bulk oxygen redox.[70,138–140] Simply put, the Li_2MnO_3 component in LR-NMC nanocomposites acts as a reservoir of excess Li ions, facilitating capacity beyond the conventional transition-metal (TM) redox by utilizing the inherent TM-O covalency-driven bulk oxygen redox at higher potentials.

4.5 Supplementary Information

4.5.1 Material Synthesis and Electrochemical Characterization

Li_2MnO_3 was synthesized by collaborators using the modified Pechini method detailed elsewhere.[141] Cathodes for electrochemical characterization shown in Figure 4.1c and for charge electrodes in Figure 4.2 and 4.3b and c were prepared by mixing 75 wt% active material, 15 wt% acetylene black (Alfa Aesar) and 10 wt% polyvinylidene di-fluoride (Sigma Aldrich) binder in the N-methyl-2-pyrrolidone solvent (Sigma Aldrich). The resultant slurry was tape-cast on to an aluminum current collector and dried at 80°C in vacuum oven overnight. After drying, circular discs of about 12 mm diameter with active mass loading of 5-6 mg cm^{-2} were punched out, which acted as the cathode. Electrochemical testing was carried out using CR2325-type coin cells. Cell assembly was carried out inside the He-filled glovebox using lithium metal chip as the anode, a solution of 1 mol $LiPF_6$ in EC:DMC (1:1) organic solvents as the electrolyte and a Celgard 2325 membrane as a separator. The cells were cycled between 2 V and 5 V vs. Li/Li^+ with a constant current density of 4.6 mA g^{-1} (i.e., C/50 with 1C = 230 mA g^{-1} assumed) during the first charge and of 23 mA g^{-1} (i.e., C/10) during the subsequent cycles using VMP multichannel potentiostat (Bio- Logic). Cathodes used in differential electrochemical mass spectrometry (DEMS) measurements were prepared by mixing 75 wt% active material, 15 wt% acetylene black (Alfa Aesar) and 10 wt% polytetrafluoroethylene (Sigma Aldrich) binder, followed by pressing the resulting paste onto stainless steel current collector meshes to achieve an active mass loading of 5-6 mg cm^{-2}. DEMS cells were charged at a current density of 20 mA g^{-1} in 1 M $LiPF_6$ in EC:DMC using a Li metal counter electrode. More details about the DEMS setup and protocol can be found in Ref. 15.

4.5.2 Operando Mn K-edge XAS

Operando XAS measurements at the Mn K-edge of Li_2MnO_3 were carried out at beamline 6BM of National Synchrotron Light Source-II (NSLS-II) by collaborators using a pouch cell configuration, whose voltage profiles are presented in SI Figure 4.6. Measurements were carried out in the transmission mode using the Si(111) double crystal monochromator. An unfocussed incident beam with a spot size of 6 mm x 1 mm was used. Absolute energy calibration of the monochromator was carried out by measuring reference foil of pure Mn simultaneously with the pouch cell. Gas-filled ionization chambers were used to record the intensities of the incident beam and the beams transmitted through the pouch cell and the reference foil. Data processing such as background subtraction and normalization was carried out as described elsewhere4 using the software ATHENA of the package IFEFFIT

4.5.3 XPS/HAXPES Measurements

Lab-based X-ray photoelectron spectroscopy (XPS) using an Al Kα source (1.486 keV) was performed at the Analytical and Diagnostics Laboratory (ADL), Binghamton University. Hard X-ray photoelectron spectroscopy was collected at beamline I09 at the Diamond Light Source Ltd. (DLS), UK, using a photon energy of hv $\approx$ 5940 eV (which will be referred to as 6 keV). The variation in kinetic energy of the outgoing electrons at these two energies provided insight into oxygen chemical environments near-surface (1.486 keV) and subsurface (6 keV) regions. A combination of the C 1s peak C–C associated with carbon black (284.5 eV) and Mn 2p/3p peaks associated with the Li_2MnO_3 material were used to calibrate the binding energy axis of the XPS and HAXPES O 1s spectra.

4.5.4 Mn L-edge and O K-edge XAS/RIXS Measurements

Soft X-ray absorption spectroscopy measurements of the Mn L-edge and O K-edge were conducted at the iRIXS endstation, beamline 8.0.1, at the Advanced Light Source by collaborators. Bulk O K-edge XAS spectra were collected in total fluorescence yield (TFY) mode. Resonant inelastic X-ray scattering (RIXS) maps of the O K-edge were collected for the high state of charge electrodes (4.8 V and 5.0 V). The Mn L-edge was collected in total electron yield (TEY) mode. Previously reported reference spectra of the Mn Ledge of MnO, Mn_2O_3, and Li_2MnO_3 are included for identification of the near-surface Mn oxidation state.

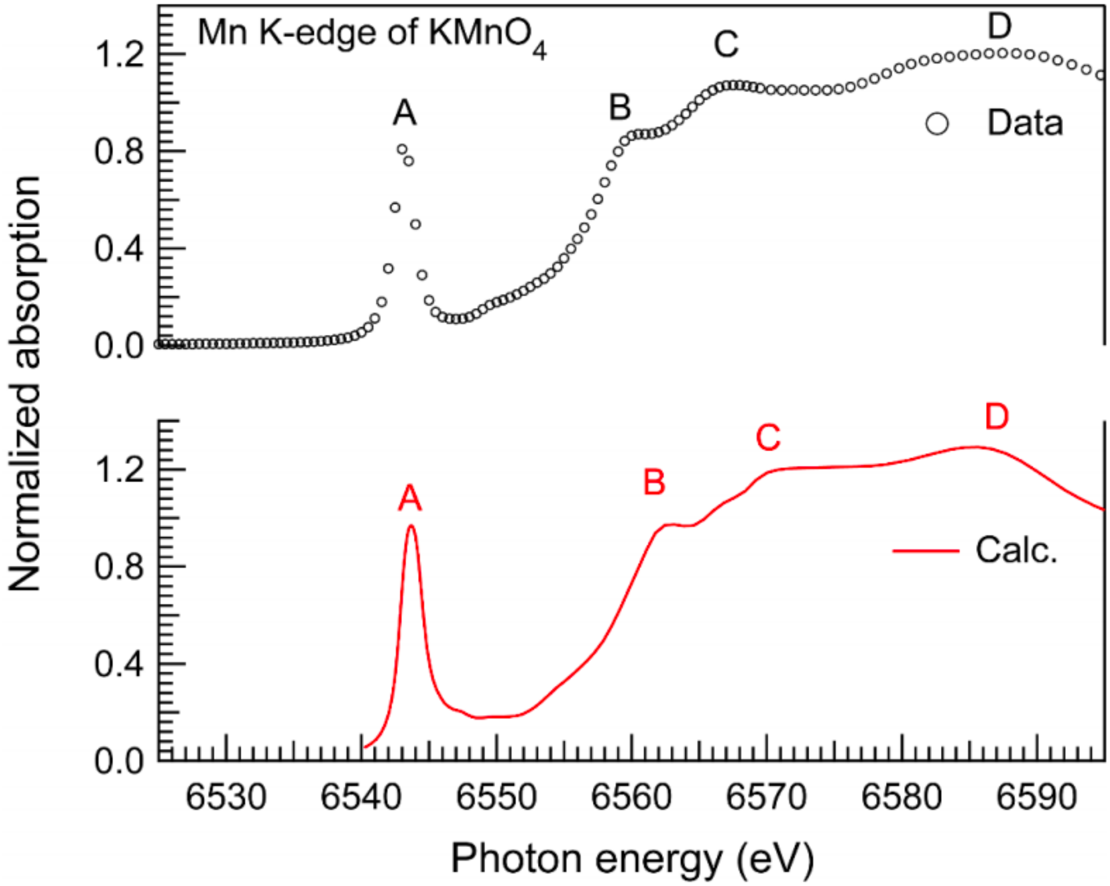

Figure 4.4: Comparison of the calculated (Materials Project) Mn K-edge absorption spectrum with the experimental data. All major features (A, B, C, and D) predicted by the calculations are reproduced by the experimental data.

A TiO_2 reference was used to calibrate energy axis for the O K- and Mn L-edges. Emission energy was calibrated from the elastic peak. Disassembled electrodes were mounted in an argon glovebox on conductive carbon tape and transferred to the measurement chamber using a vacuum suitcase for XPS, HAXPES and XAS/RIXS measurements. All electrodes were washed with DMC for 5 min in a glovebox post-disassembly.

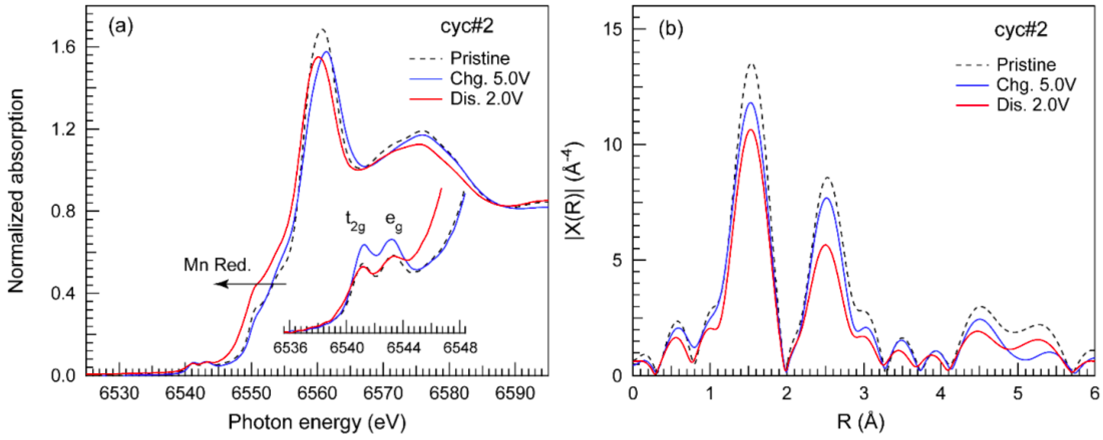

Figure 4.5: Operando Mn K–edge XANES (a) and EXAFS (b) data for the 2nd cycle.

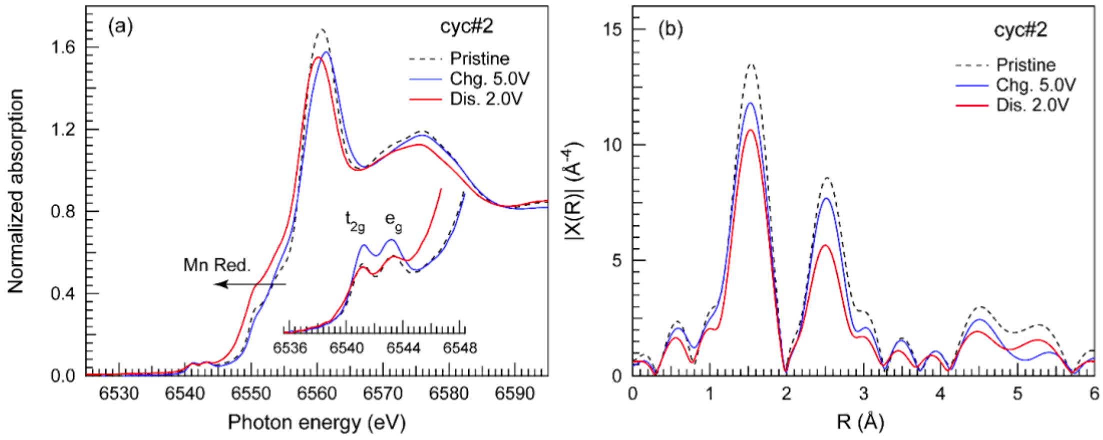

Figure 4.6: Voltage profiles of Li_2MnO_3 pouch cells during operando Mn K–edge XAS measurements (1st cycle in black and 2nd cycle in red)

Titrated Material	**mmol O_2/mol active material**
C 5.0 V	10.5
C 5.0; D 2.8 V	1.3

Table 4.2: Reversible oxygen redox titrations. Oxygen gas evolution quantities for peroxide-like oxygen titrations for Li_2MnO_3

Titrated Material	**mmol CO_2/mol active material**	**Calculated wt% Li_2CO_3**
Pristine powder	6.25	0.40
Pristine electrode*	14.0	0.88
Soaked electrode*	23.7	1.50

*made with a separate batch of synthesized LMO

Table 4.3: Carbonate content titrations. Carbonate gas evolution quantities and calculated Li_2CO_3 wt% for pristine and electrolyte for Li_2MnO_3.

Chapter 5

A Comparison of High Voltage Outgassing of $LiCoO_2$, $LiNiO_2$, and Li_2MnO_3 Layered Li-ion Cathode Materials

5.1 Abstract

One method of increasing the energy density of Li-ion batteries is to access reversible Li intercalation in conventional transition metal oxides cathode materials at high potentials (4.3-5 V vs. Li/Li^+), and thus allow more electrochemical capacity per volume of active material. This comes at the cost of increased interfacial reactivity and often results in capacity fade over many cycles. Tracing gas evolution during lithium extraction and insertion provides a useful strategy to understand this high voltage reactivity. In this chapter, outgassing during Li extraction is examined in the parent materials of current state-of-the-art layered oxides ($LiCoO_2$, LCO; $LiNiO_2$, LNO; and Li_2MnO_3, LMO). Key differences in the outgassing of each material are highlighted. Whereas negligible O_2 release is found in LCO and LNO, even with voltage holds at 5 V vs. Li/Li^+, O_2 release is found to account for a large portion of the electrochemical capacity and persist over many cycles in LMO. CO_2 outgassing is observed to varying extents, following the trend of LMO >> LNO > LCO, and is due to a combination of residual solid carbonate oxidation and electrolyte degradation. Taken together, these results show the importance of quantitative analysis in understanding the role of transition metal composition on the chemistry of conventional Li-ion battery materials.

5.2 Introduction

Li-ion batteries optimally combine energy density, lifetime, safety, and cost compared to alternative rechargeable battery chemistries. These favorable characteristics are in part contributed by the cathode, commonly a layered lithium transition metal oxide capable of highly reversible lithium removal and intercalation. Modern cathode stoichiometries are typically composed of transition metal oxides combining Co, Ni, and/or Mn in varying ratios to form NMC ($LiNi_xMn_yCo_zO_2$, x+y+z=1) compounds. These NMC materials exhibit properties related to their parent compounds — lithium cobalt (III) oxide ($LiCoO_2$, LCO), lithium nickel(III) oxide ($LiNiO_2$, LNO), and lithium manganese(IV) oxide (Li_2MnO_3, LMO) — and the stoichiometries can be adjusted to optimize desired traits. Demand for increased energy density and capacity continues as car owners seek to transition away from internal combustion vehicles to electric vehicles powered by Li-ion batteries. To access more electrochemical capacity per volume of active material, conventional transition metal oxides can be operated into high potentials (4.3-5 V vs Li/Li^+).[142] However, many challenges exist in the high voltage regime that are often related to bulk material deterioration and surface instabilities.[85,143] Despite many studies reporting operation to 4.5 V or even 5 V vs Li/Li^+, many questions remain about the high voltage reactivity for cathode materials of even simple stoichiometry.[144,145] Using the three well-known parent oxide materials, LCO, LNO and LMO, this study quantifies outgassing with differential electrochemical mass spectrometry (DEMS) to further the understanding of cathode interfacial reactivity in the high voltage region.

Lithium cobalt oxide (LCO), the most well-studied Li-ion battery cathode material, is known to operate with extreme reversibility in the voltage region of 3.0-4.2 V.[3] Lithium nickel oxide (LNO), once hoped to be a cheaper alternative to LCO given their structural and charge compensation similarities, is also electrochemically active in this voltage region.[146] When these materials are operated at higher potentials, the prevailing theory is that oxygen dimerization and O_2 gas release results in irreversible cathode degradation.[143,147–149] With detailed gas evolution measurements, this chapter shows that negligible O_2 gas and little CO_2 release are observed from LCO, even up to 5 V vs Li/Li^+. Gas evolution measurements also reveal the important role of residual surface carbonates on outgassing, particularly CO_2, when operated at high voltages. Using acid titrations and isotopic labeling, it is further demonstrated that negligible oxygen dimerization through oxide oxidation occurs, challenging this mechanism for LCO and LNO degradation.

Lithium manganese oxide (Li_2MnO_3), LMO, is not typically used as a cathode material by itself, but is instead used as a precursor for Li-rich cathode materials given the high starting oxidation state of Mn (4+). In fact, LMO was long believed to be electrochemically inactive due to the high starting oxidation state of manganese.[93] However, when charged to 5 V, an extensive first charge capacity can be accessed.[22,95,150] This has lead to several theories of charge compensation, ranging from oxygen compensation (both irreversible and reversible) to further manganese oxidation to the +7 state.[111] The previous chapter has shown that the first charge capacity can be almost entirely attributed to irreversible processes, but left in question the recovered capacity on subsequent cycles.[151] In this chapter, charge compensation mechanisms for cycled LMO are also explored and find that O_2 and CO_2 evolution persists over many cycles. Furthermore, O_2 evolved in closed cells (e.g., coin cells) on charge is shown to be consumed on discharge in a manner similar to a carbonate-solvent based Li-O_2 battery, where electrolyte degradation participates in the oxygen electrochemistry.

Taken together, these high voltage outgassing measurements and accompanying characterizations are valuable as cathode materials with higher energy densities are researched. The insights gained from LCO, LNO, and LMO outgassing may help guide the design of future cathode materials and challenge previous assumptions for a better understanding of high voltage reactivity.

5.3 Experimental Methods

5.3.1 Electrode Preparation

LCO and LNO cathodes were composed of active materials, Super P (Timcal), and polytetrafluoroethylene (PTFE, DuPont, Teflon 8A) at a weight ratio of 80:10:10. LMO cathodes were composed of active materials, acetylene black, and PTFE at a weight ratio of 75:15:10. To make the cathodes, 90 mg of active materials/carbon black in the ratios provided above were well mixed using a mortar and pestle inside an Ar-filled glovebox for 20 min. PTFE was later added and manually mixed with the mixture for 20 min. The components were then rolled and pressed onto discs of stainless steel mesh (1 cm^2) inside the glovebox. The loading density of the films was approximately 7-8 mg cm^{-2} based on active materials. The specific capacities were then calculated based on the weight of active materials in the cathode films.

5.3.2 Differential Electrochemical Mass Spectrometry

The custom-built DEMS, cell geometry, and instrument operation is described in detail in previous publications.[15,152] Custom Swagelok cells were assembled inside a glovebox and tested on the DEMS system at room temperature. 1 M $LiPF_6$ in ethylene carbonate (EC) and dimethyl carbonate (DEC) solution (volume ratio 1:1) was used as the electrolyte. Glass microfiber (Whatman) and Celgard 2500 (one of each) were used as separators, with the Celgard in contact with the cathode. Li-metal foil was used as the anode. The assembled cells were charged under a head of positive argon pressure (around 1.2 bar) after being appropriately attached to the DEMS, and the headspace was swept to the mass spectrometer at regular intervals. The mass spectrometer was previously calibrated to quantify O_2 and CO_2.

5.3.3 X-ray Photoelectron Spectroscopy

The X-ray photoelectron spectroscopy (XPS) was acquired with a Thermo Fischer K-Alpha Plus instrument at the Molecular Foundry at Lawrence Berkeley National Laboratory. Sample cathodes were acquired from cell disassembly inside a glovebox after the associated electrochemical measurement. Extracted cathodes were then washed drop-wise with DMC, and dried under vacuum. The extracted cathodes were then placed in an air-tight XPS sample holder and transferred to the instrument for measurements. Background subtraction and energy calibration was performed using CasaXPS software.

5.3.4 Material Synthesis

$LiNiO_2$ was prepared by ball milling $Ni(OH)_2$ and Li_2CO_3 (Sigma Aldrich) for 3 h, followed by annealing under an oxygen atmosphere (flow rate: 5 cfm) at 750 °C for 12 h. Powder X-ray diffraction (XRD) patterns were collected on a Bruker D2-Phaser with Cu Kα radiation ($\lambda = 1.54178$ Å).[153] LMO was prepared by combining solutions of manganese acetate, citric acid, and lithium hydroxide in water. The water was boiled off to form a gel, which was then freeze dried to produce a dry powder. The powder was subjected to a two-step calcination process, heating first at 450 °C for 10 h followed by 700 °C for 20 h under dry air (nitrogen and oxygen only).

5.3.5 ^{18}O Substitution

$LiCoO_2$ was enriched with ^{18}O by heating powder samples to 800 °C under a $^{18}O_2$ (Sigma Aldrich) and N_2 headspace for 6 hours. $LiNiO_2$ was enriched with ^{18}O by heating powder samples to 600 °C for 6 hours under identical headspace conditions. For a full description of the isotopic enrichment process see the Supporting Information of reference 86.

5.4 Results and Discussion

5.4.1 Lithium Cobalt Oxide ($LiCoO_2$), LCO

Lithium cobalt oxide is known to operate reversibly up to potentials of 4.2 V vs Li, or the removal of roughly half the total lithium.[3] Overdelithiation results in severe capacity loss on subsequent cycles and is caused by the phase transition of Li_xCoO_2, oxygen loss,[143,148] Co dissolution,[154] and side reactions with the electrolyte.[155]

Upon delithiation of the cathode, oxidation of Co ($3d^6$ (${t_{2g}}^6{e_g}^0$)) in $LiCoO_2$ is accomplished by electron removal from the t_{2g} orbital. As delithiiation continues, the migration of the 3d band into the 2sp band of oxygen has been theorized to activate the oxidation of oxygen.[21] Therefore, charge compensation at high degrees of $LiCoO_2$ delithiation is believed to be achieved by both O and Co redox simultaneously, resulting in dimerization of oxygen and O_2 gas release.[143,148,156] There are few studies characterizing gas release for LCO, but it has now been shown that oxygen evolution is not always a characteristic of LCO overdelithiation. In particular, studies by Novak et al.[85] and Abruña et al.[157] have studied qualitative gas evolution during cyclic voltammetry measurements for LCO. Both studies demonstrated CO_2 release and only negligible or no oxygen release during CV measurements. The lack of substantial oxygen release is surprising given the proposed mechanisms for a high voltage LCO phase transition.[147] In this study, additional electrochemical methods are combined with quantitative measurements of gas evolution and peroxo-like oxygen formation to understand this discrepancy more completely.

Figure 5.1 presents quantitative gas evolution measurements on a LCO electrode during the first three constant current cycles (C/10 between 3.4 V and 5 V), cyclic voltammetry (0.05 mV s^{-1} between 3-5 V), and a C/10 constant current charge followed by a voltage hold at 5 V. Each measurement was performed using electrochemical cells with 1 M $LiPF_6$ EC/DEC electrolyte, a glass fiber separator, and a Li metal anode. Up to 5 V, negligible O_2 gas release is observed during each of these measurements, with perhaps a barely perceptible (but non-quantifiable) amount of oxygen evolution in the cycling measurements at high voltages. Instead, a small but significant amount of CO_2 is the dominant gas evolved; for example, 4.7 mmol CO_2 per mol LCO is evolved during the first charge to 5 V, and 12.2 mmol CO_2 per mol LCO is released during the CV to 5 V (Table 5.1), with the discrepancy likely due to the larger duration spent above 4.6 V in the CV measurement. On the first cycle (Figure 5.1a), CO_2 evolution commences at $\sim$4.1 V and is bimodal, with a small first peak in CO_2 evolution below 4.6 V, followed by a sharp increase in CO_2 evolution above 4.6 V. These observations are roughly in agreement with the CV measurement (Figure 5.1b), where CO_2 evolution commences at 4.15 V and strongly increases above 4.6 V. On subsequent constant current cycles, the CO_2 evolution peak initially observed below 4.6 V is not present, and the sharp CO_2 evolution peak above 4.6 V attenuates after the second cycle. Furthermore, the onset of CO_2 evolution shifts to higher potentials ($\sim$4.3 V) on the second and third cycles.

Two possibilities for the origin of CO_2 are electrolyte oxidation or decomposition of residual carbonate that remains on the LCO surface after synthesis, handling, and electrode preparation. Both XPS (SI Figure 5.7) and an acid titration of the pristine LCO electrode reveal the presence of surface carbonates, although the acid titration quantification indicates only 0.1 wt% carbonates (1.5 mmol per mol LCO) in the as-prepared electrode. Note that this is an exceptionally low amount of residual carbonate compared to many other oxide active materials that have been similarly characterized, including NMC, LNO and LMO (as discussed later).[92,158,159] If all of the residual surface carbonate were to oxidize at high voltages to evolve CO_2, 1.5 mmol CO_2 per mol LCO would be expected. As indicated in Table 5.1, the total CO_2 evolved on the first cycle (Figure 5.1a) below 4.6 V is 3.3 mmol mol^{-1} and 4.7 mmol mol^{-1} throughout the entire first charge. These values are substantially larger than the values expected from surface carbonate oxidation alone, indicating that electrolyte degradation, rather than residual carbonate oxidation, is the dominant contributor to CO_2

evolution at all potentials. A key question is then raised: does electrolyte degradation result from reactive oxygen release (e.g., singlet oxygen or surface peroxo-like species formation) from the LCO oxide lattice, or does the electrolyte simply degrade electrochemically at the LCO surface at high voltages? Oxygen activity at high voltages is now considered to answer this question.

	LCO		LNO		LMO		
Initial Li_2CO_3	1.5		3		14		mmol mol^{-1}
Outgassing during x	O_2	CO_2	O_2	CO_2	O_2	CO_2	
Ch to 4.2V	<1	<1	<1	<1	<1	<1	
Ch to 4.6V	<1	3.3	<1	3.8	<1	4.0	
1st cycle	<1	6.2	2.4	64	140	36	mmol mol^{-1}
3 cycles	<1	13	2.5	67	160	67	
Ch to 5.0V and hold	<1	100	6.1	78	300	170	
1st Cycle CV (5.0-3.0V)	<1	12	1.8	110	110	72	

Table 5.1: Outgassing quantities summarized for LCO, LNO, and LMO during specified measurements.

Given the surprising lack of O_2 evolution during LCO delithiation over multiple cycles (Figure 5.1a), a C/10 constant current charge to 5 V followed by a voltage hold at 5 V was performed until the current decayed to C/100 (Figure 5.1c) in an intentional (and severe) attempt to oxidize the LCO lattice. Even with an extended 5 V hold, no detectable O_2 was evolved within instrument resolution, but a sizable amount (88 mmol mol^{-1}) of CO_2 was evolved. The total capacity recovered from the charge and voltage hold in Figure 1c was 313 mAh g^{-1}, implying that Li removal alone could not be the only source of electrochemical capacity, as the theoretical capacity of fully delithiating LCO ($LiCo(III)O_2 \rightarrow Li^+ + Co(IV)O_2$) is 272 mAh g^{-1}. Assuming CO_2 is evolved from electrolyte degradation in a 2 electron per molecule CO_2 process, 88 mmol CO_2 mol^{-1} corresponds to an electrochemical capacity of 47 mAh g^{-1}, which infers that electrolyte degradation entirely accounts for the difference in observed capacity (313 mAh g^{-1}) and the theoretical full delithiation capacity (272 mAh g^{-1}). The observation of negligible O_2 release also infers that oxide lattice oxygen is not participating in charge compensation during delithiation.

To further probe oxide oxidation, a titration protocol that can accurately estimate the presence of peroxo-like oxygen was used to determine formation of such species during charge. Extracted electrodes were titrated according to a procedure described in depth in a previous study (see Experimental Methods section).[159] No significant peroxo-like oxygen species were formed within titration detection limits, even at high levels of delithiation during the first charge to 5 V or after the 5 V hold. Ultimately, the lack of oxygen release and O dimerization indicates that neither contributes significantly to LCO decomposition. This also implies that

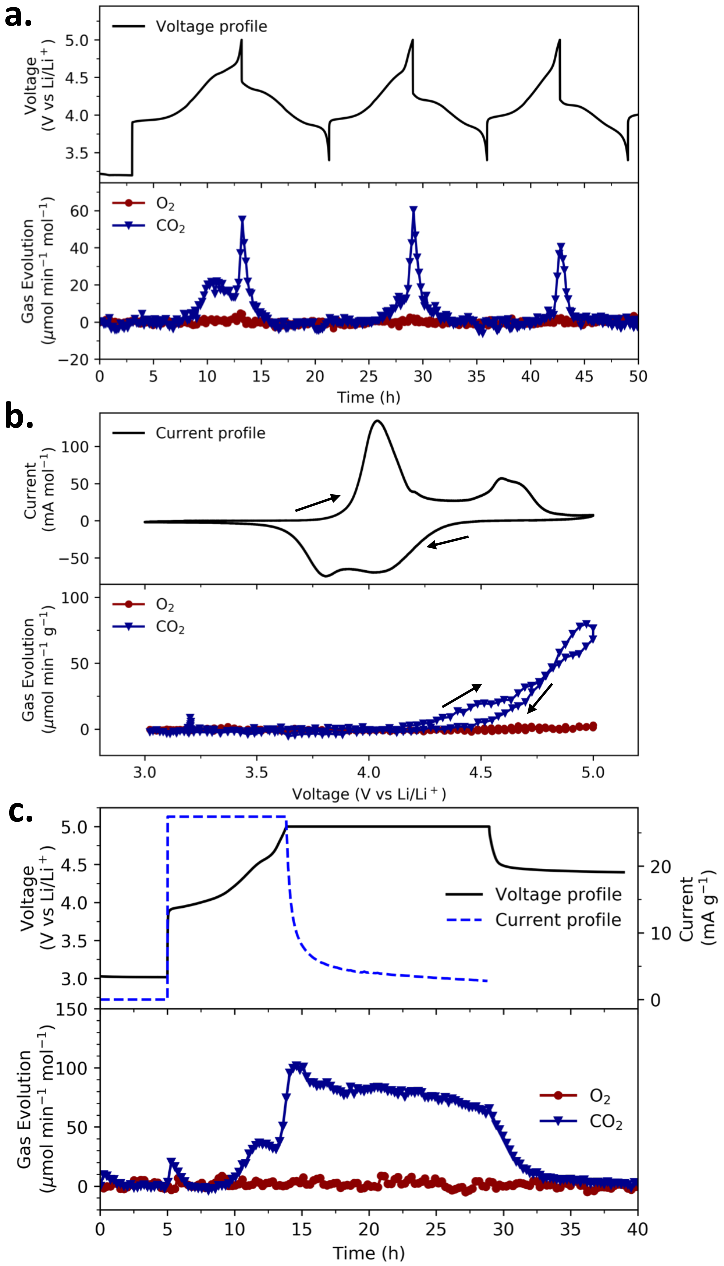

Figure 5.1: Gas evolution from LCO electrodes. Gas evolution measured during (a) first three cycles at C/10, (b) cyclic voltammetry at 0.05 mV/s, and (c) a charge to 5 V at C/10 followed by a voltage hold under the rate decayed to C/100. C-rates are based on theoretical full delithiation of $LiCoO_2$.

reactive oxygen release does not contribute to electrolyte degradation at LCO surfaces: if O-dimerization is not observed, then singlet oxygen and peroxo-like species cannot form and react with the electrolyte, as has been observed in NMC materials.[159,160]

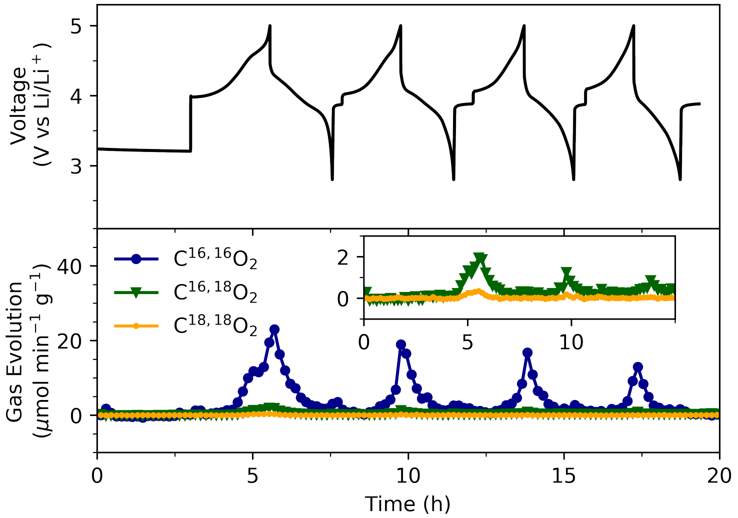

Figure 5.2: CO_2 outgassing as measured for ^{18}O labeled LCO during the first four cycles at a rate of 100 mA g^{-1} (C/2.7).

	$C^{16,16}O$	$C^{16,18}O$	$C^{18,18}O$	Total (mmol mol^{-1})
Initial Li_2CO_3 titration	0.83	0.06	<0.01	0.90
Total CO_2 evolved (DEMS)	4.19	0.06	<0.01	4.25

Table 5.2: CO_2 evolved from acid titrations on ^{18}O enriched LCO powder and the first four C/2.7 cycles shown in Figure 5.2.

To bolster this argument, evolution measurements at LCO electrodes enriched with ^{18}O were performed. The ^{18}O enrichment is performed by heating LCO powder under an $^{18,18}O_2$ environment to a temperature just below the material synthesis annealing temperature. This enrichment procedure labels not only the surface of the oxide, but also the residual surface carbonate. An acid titration indicates that roughly 7% of the O in the surface carbonate is ^{18}O labelled after the enrichment procedure, and 0.9 mmol surface carbonate per mol LCO is present. Unfortunately, the isotopic labelling of the LCO lattice could not be quantified due to the lack of oxygen release or oxygen activity that are typically employed to measure ^{18}O exchange. However, it is expected that ^{18}O enrichment near the LCO surface will be similar to the residual carbonate ^{18}O concentration, as has been observed for many other oxides that have been studied.[158,159] Figure 5.2 shows the evolution of the three CO_2 isotopes ($C^{16,16}O_2$, $C^{16,18}O_2$, and $C^{18,18}O_2$) during the first four constant current cycles at C/2.7 between 2.8-5 V, and Table 5.2 summarizes the isotopic breakdown of the three CO_2 isotopes evolved during cycling and acid titration of the residual carbonate. Of particular interest, all ^{18}O contained in the evolved CO_2 (0.06 mmol per mol LCO) can be accounted for by the initial amount of ^{18}O (0.06 mmol per mol LCO) in the residual surface carbonate. If O release from the LCO oxide lattice resulted in electrolyte degradation and CO_2 evolution, it is likely that the evolved CO_2 would be enriched in ^{18}O beyond what can be accounted for by residual carbonate oxidation, and this is not the case. Furthermore, no organic fragments containing peroxo groups (R-O-O) are observed during acid titrations of LCO electrodes charged to 5 V, as have been observed in other systems where reactive oxygen release has been postulated. R-O-O species have been theorized to form during delithiation of many oxide materials where oxide lattice oxidation occurs,[161] and observations supporting this formation will be expounded in a future study.

The outgassing and titration measurements on LCO cathodes provide evidence that no O_2 release or O dimerization occurs, and no LCO lattice oxygen participates in the production of CO_2. Ultimately, these findings strongly suggest that electrolyte degradation at LCO electrodes occurs due to an electrocatalytic effect of LCO towards electrolyte oxidation rather than due to reactive oxygen release from LCO.

5.4.2 Lithium Nickel Oxide ($LiNiO_2$), LNO

In the early 1990s, LNO was proposed as a viable replacement for LCO as it is isostructural to LCO, has a slightly lower operating voltage, and is significantly less expensive.[146] In principle, the redox chemistry of $LiNiO_2$ is straightforward, because Ni^{3+}/Ni^{4+} redox can perfectly accommodate 1 Li^+ extraction/insertion during the charge and discharge. In contrast to LCO, upon delithiation of layered LNO the oxidation of Ni^{3+} ($3d^7$ ($t_{2g}{}^6e_g{}^1$)) to a tetravalent state removes the electron from the e_g orbital. Therefore, electron transfer from the O 2p band is theorized to occur only at highly charged states or low Li^+ content. However, the full oxidation of Ni^{3+} and full removal of 1 Li^+ from $LiNiO_2$ are difficult because the realization of pure Ni^{4+} in the system is challenging.[153] Further challenges that prevent the widespread use of LNO including cation migration, difficulty achieving precise stoichiometry during synthesis, and extreme reactivity with air and moisture. Nevertheless, given the move toward Ni-rich layered oxides as next generation cathode materials, understanding the high voltage stability of $LiNiO_2$ is important.

Phase-pure $LiNiO_2$ was synthesized by a solid-state reaction as reported elsewhere.[153] It exhibits a typical layered α-$NaFeO_2$ structure ($R\bar{3}m$) with negligible Li/Ni intermixing (1.4%) in the final product based on Rietveld refinement results (Figure S2). The synthesized LNO was used to make cathodes for cycling, cyclic voltammetry, and voltage hold gas evolution measurements similar to those already presented for LCO. The outgassing for LNO for the first three constant current cycles between 2-5 V at C/10, the cyclic voltammetry from 3-5 V at 0.05 mV/s, and a C/10 charge followed by a voltage hold at 5 V are shown in Figure 5.3.

For the first cycle and CV outgassing measurements, any O_2 evolution is greatly eclipsed by large quantities of CO_2 evolution. A small but significant amount of CO_2 release begins to occur at 3.9 V, followed by a massive spike in evolution rate at > 4.4 V. O_2 gas evolution quantities for constant current charging and cyclic voltammetry were 2.5 mmol mol^{-1} and 2 mmol mol^{-1} respectively, while CO_2 gas evolution reached 51 mmol mol^{-1} for the first LNO cycle and 112 mmol mol^{-1} for the LNO CV, where similar to LCO, this discrepancy can be attributed to the time the electrode spends at potentials above 4.6 V, where CO_2 evolution is dramatic. When the LNO cell was held at 5 V after the first charge (Figure 5.3c), slightly more oxygen evolved, while CO_2 evolution quickly diminished, particularly when compared to the attenuation observed in LCO, implying that near-surface restructuring of LNO results in faster passivation at high voltages. An acid titration revealed that the residual carbonate in the pristine LNO powder was 0.2 wt% (2.5 mmol Li_2CO_3 mol^{-1} LNO), which is low, but still roughly twice that of LCO. The presence of carbonate species was also confirmed by XPS (SI Figure 5.7). Clearly, these data suggest that electrolyte degradation, rather than surface carbonate oxidation, dominates CO_2 evolution in LNO, particularly at high voltages. However, unlike the LCO results, the small O_2 evolution implies that reactive oxygen release from the LNO lattice could be playing a role in electrolyte degradation at high voltages. To examine the contribution of oxide lattice oxidation to the outgassing observed for LNO, further studies were conducted utilizing ^{18}O isotopic labeling.

Similarly to LCO, the enrichment of LNO was performed by heating LNO powder under an $^{18,18}O_2$ environment to a temperature (600 °C) just below that of the material synthesis annealing temperature. For LNO, this procedure increased the quantity of surface carbonates, as a titration of the ^{18}O labeled LNO powder revealed 17 mmol Li_2CO_3 mol^{-1} LNO (1.3 wt%) in which roughly 31% of the O in the surface carbonate was ^{18}O.

Surprisingly, the heat treatment also influenced both the voltage profile and the total CO_2 outgassing of the ^{18}O labelled LNO. The observed charging capacity of the ^{18}O labelled LNO was approximately 20 mAh g^{-1} greater than that of the unlabelled LNO, while the CO_2 outgassing was roughly half that of the unlabelled material (Figure 5.4, Table 5.1 and Table 5.3). Although we cannot definitively state the cause of outgassing suppression, it is likely due to either passivation related to the newly deposited surface carbonate, or a structural reorganization and subsequent decrease in degradation activity of the LNO surface due to slight delithiation. Studies are currently underway to understand the effects of heat treatment and the gas evolution decrease, which we hope can provide a promising strategy to improve LNO stability.

Outgassing from cathodes made with the enriched LNO during the first three cycles shows

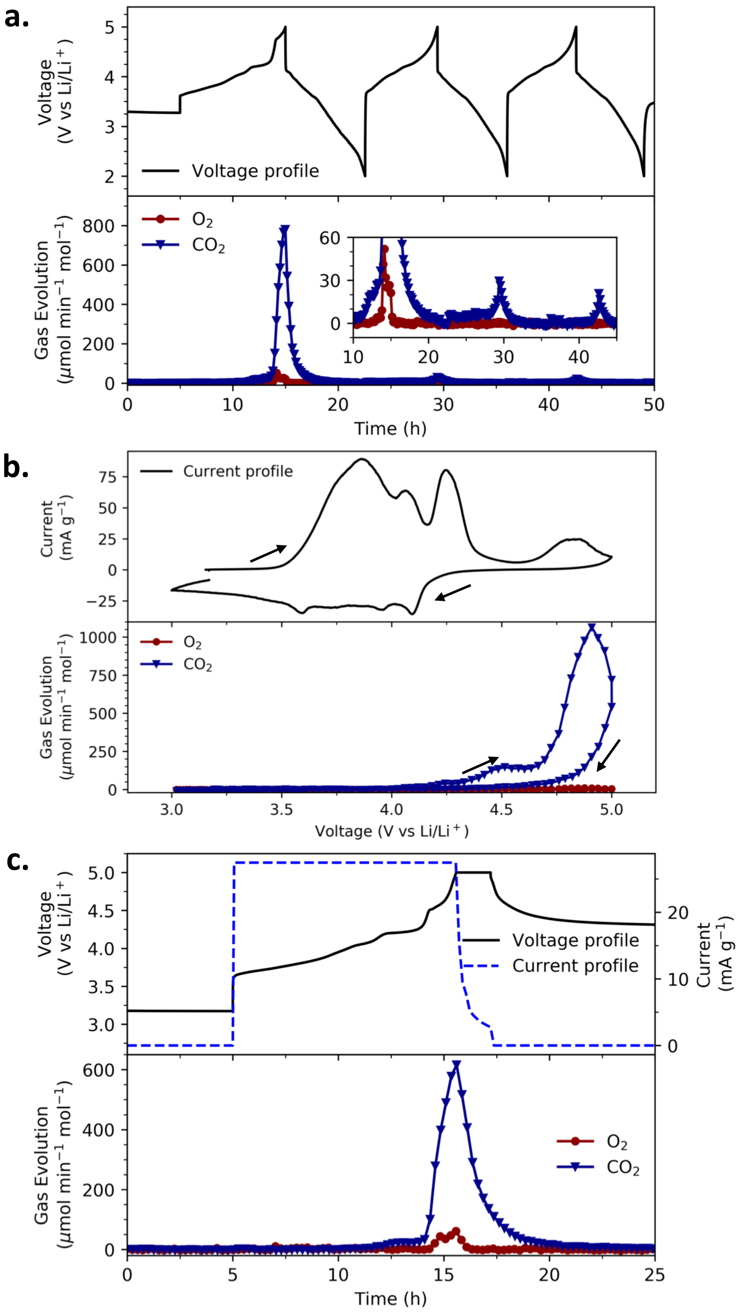

Figure 5.3: Gas evolution from LNO electrodes. Gas evolution measured during (a) the first three cycles at C/10, (b) cyclic voltammetry at 0.05 mV/s, and (c) a C/10 constant current charge to 5 V, followed by a voltage hold until the current reached C/100. C-rates are based on theoretical full delithiation of $LiNiO_2$.

significant $C^{16,18}O_2$ and $C^{18,18}O_2$ (Figure 5.4). Table 5.3 presents the isotopic breakdown of the total CO_2 evolved during the measurement presented in Figure 5.4, as well as the isotopic breakdown of the surface Li_2CO_3 present on the LNO powder after the labelling procedure. While the total CO_2 evolved is almost twice the Li_2CO_3 initially present, indicating that electrolyte degradation contributes to CO_2 evolution, nearly all ^{18}O integrated into evolved CO_2 can be accounted for by ^{18}O originally contained in the Li_2CO_3. If a sizable amount of LNO lattice oxygen (which is also enriched in ^{18}O) was released and subsequently reacted with the electrolyte, a larger percentage of ^{18}O in the evolved CO_2 would be expected, implying that this mechanism only accounts for, at most, a minor fraction of the overall electrolyte degradation. Instead, as with the LCO, electrolyte degradation occurs primarily through high voltage electrocatalysis on the LNO surface. Nevertheless, these results indicate that reactive oxygen release does occur to a slight extent in LNO, unlike LCO where no evidence of reactive oxygen release was observed. Unfortunately, we were unable to quantify the formation of peroxo-like species formed at various states of charge for LNO because the acid titration we employ to do so resulted in direct oxygen evolution from the oxide lattice, including from the as synthesized powder, where clearly no peroxo-like species should be present (SI Table 5.4). This large oxygen evolution is likely coupled to Ni reduction back to its +2 state, and future studies will describe this mechanism in detail. Nevertheless, in a prior study, a small amount of peroxo-like oxygen was observed in LNO upon charge to 5 V using resonant inelastic X-ray spectroscopy (RIXS), in agreement with this study.[153]

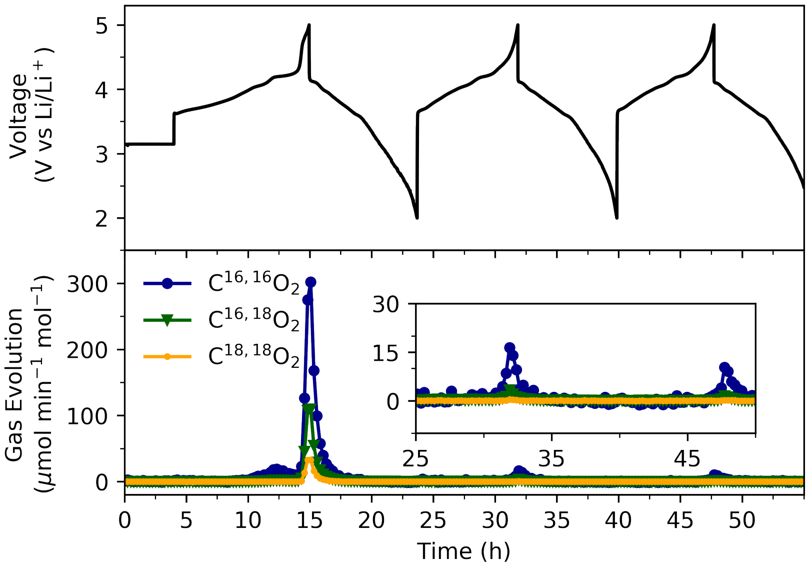

Figure 5.4: Gas evolution at a ^{18}O labeled LNO electrode measured during the first three cycles at C/10.

	$C^{16,16}O$	$C^{16,18}O$	$C^{18,18}O$	Total (mmol mol^{-1})
Initial Li_2CO_3 titration	8.5	6.4	2.1	17.0
Total CO_2 evolved (DEMS)	21.0	7.3	2.0	30.4

Table 5.3: Total CO_2 outgassing quantities summarized for ^{18}O labeled LNO shown in Figure 5.4.

When comparing LNO and LCO outgassing, a marked difference is the order of magnitude higher total CO_2 evolution observed in LNO on the first cycle (Table 5.1). Yet, O_2 and CO_2 evolution in the second and third cycles is less for LNO than LCO, and O_2 evolution is barely perceptible. Additionally, when comparing the 5 V voltage holds (Figure 5.1c and 5.3c), LCO is able to support a current for a longer period than LNO, where the current attenuates quickly. These findings imply that while LCO has a lower native electrocatalytic activity for electrolyte degradation, LNO more readily forms a passivation layer that inhibits its high native electrocatalytic activity. In support of this theory, acid titrations of extracted LNO and LCO cathodes after charging determined that large quantities of solid carbonate are deposited on the LNO surface due to electrolyte degradation after charging to 5 V, whereas very little carbonate is deposited on the LCO (SI Table 5.4). Additionally, our previous studies have shown impedance growth as well as counter intuitive Ni reduction as a result of charging LNO to high voltages,[153] both of which also support the possibility of the formation of a passivating carbonate layer on the LNO cathode surface.

5.4.3 Lithium Manganese Oxide (Li_2MnO_3), LMO

As will be shown here, LMO's electrochemistry is substantially different from LNO and LCO. The large first charge capacity and relatively good capacity retention upon cycling led to several theories for LMO charge compensation, including oxygen redox and extended manganese redox.[111,151,162] In fact, LMO is considered critical for promoting bulk anionic redox in Li-rich oxides. However, gas evolution results (Figure 5.5, Table 5.1) demonstrate that both O_2 and CO_2 evolution can account for the majority of the first charge capacity, in agreement with our prior study[151]. In Figure 5.5a, we show the gas evolution for the first three cycles of LMO. When compared to LNO and LCO, the amount of both CO_2 and, in particular, O_2 evolution from LMO during cycling is substantial (Table 5.1). The first cycle initially shows a large CO_2 peak, followed by an even larger amount of sustained O_2 evolution. The CO_2 was shown in our previous study to evolve from solid carbonate that forms on LMO after its initial exposure to the carbonate electrolyte[151]. We note that the quantity of CO_2 evolved is variable from cell-to-cell, likely depending on the exposure time to the electrolyte and the charge rate (e.g., Figure 5.5c shows an initial peak evolution nearly 4 times higher than in Figure 5.5a). O_2 evolution commences after the CO_2 peak subsides, where it was found to account for ~80% of the electrochemical capacity during the remainder of the first charge (reasonably assuming it evolves via a 4 electron process).

In subsequent cycles, both CO_2 and O_2 evolution continue at values much greater than observed in LCO or LNO. While O_2 does continue to attenuate from cycle-to-cycle, CO_2 persists at high evolution rates in the second and third cycles, an indication that there is substantial electrolyte degradation on each cycle. It is highly likely that the chemical reactivity of LMO with the electrolyte results in a solid carbonate containing surface layer, which undergoes oxidation to CO_2 at high voltages. Upon oxidation, the exposure of LMO to the electrolyte results in further electrolyte degradation, and hence the continuous CO_2 release observed from cycle-to-cycle.

Cyclic voltammetry reveals similarly high amounts of O_2 and CO_2 outgassing. Only a small anodic wave (compared to LCO and LNO) is observed at high potentials during the positive-going scan, while no current wave is developed during the negative-going scan, implying that negligible redox processes (Mn or O redox) occur during reduction when gases are continuously swept out of the cell. Also plotted in the upper panel of Figure 5.5b is the partial current for O_2 and CO_2 evolution from the values given in the lower panel, assuming each evolves via a 4 and 2 electron process, respectively. Both of these values are reasonably assumed for O_2 evolution from an oxide and CO_2 from a carbonate.[159] Clearly, the positive-going wave is largely a result of these gas evolution processes, particularly at voltages greater than 4.6 V. Furthermore, a voltage hold measurement was also performed for LMO to observe reactivity at continued high voltage (Figure 5.5c). Similarly to the CV measurement, the partial current for O_2 and CO_2 evolution assuming respective 4 and 2 electron processes, are plotted along with measured current. We again observe that during the voltage hold and current decay, the sum of gas evolution partial currents accounts for a large fraction of the current at any time. During the measurement shown in Figure 5.5c, a total of 411 mAh g^{-1} was extracted, equal to almost 90% lithium removal if the capacity was wholly related to lithium removal. 300 mmol O_2 per mol LMO and 160 mmol CO_2 per mol LMO was evolved (Table 5.1), which assuming a 4 electron process for O_2 evolution and a 2 electron process for CO_2 evolution, correspond to 277 mAh g^{-1} and 75 mAh g^{-1} respectively. By comparison, 86% of the total capacity can be ascribed to these gas evolution processes.

To further show the parasitic reactivity of LMO, it is important to consider electrochemistry in closed cells, where gas can accumulate (e.g., coin cells). As the DEMS measurements presented in Figure 5.5 involve the continuous removal of evolved gas from the cell headspace to a mass spectrometer, we also performed simple cell headspace pressure monitoring measurements. Here, the evolved gas remains in the isolated headspace of a custom Swagelok cell across 5 cycles while the pressure was monitored (Figure 5.6). The cell headspace volume has been calibrated, allowing a simple calculation of total molar gas evolution by knowing the headspace pressure, temperature, and volume. These pressure rise/decay measurements are similar to those described in our prior Li-O_2 reports.[163]

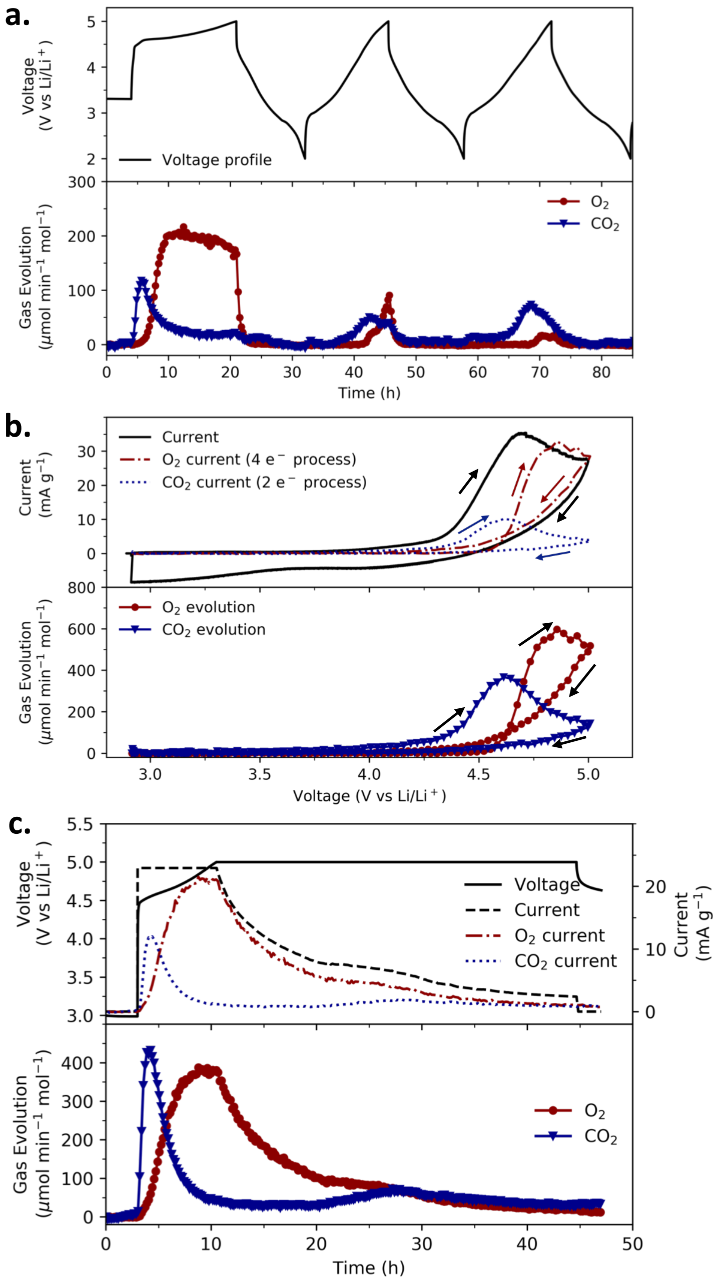

Figure 5.5: Gas evolution from LMO electrodes. Gas evolution measured during (a) the first 3 cycles at C/20 (11.5 mA g^{-1}), (b) cyclic voltammetry at 0.05 mV/s, and (c) a C/10 charge to 5 V, followed by a voltage hold to C/100. In b and c, the partial O_2 and CO_2 current are plotted assuming that the measured O_2 evolution occurs via a 4 electron process and CO_2 evolution occurs via a 2 electron process. C-rates are based on theoretical full delithiation of Li_2MnO_3.

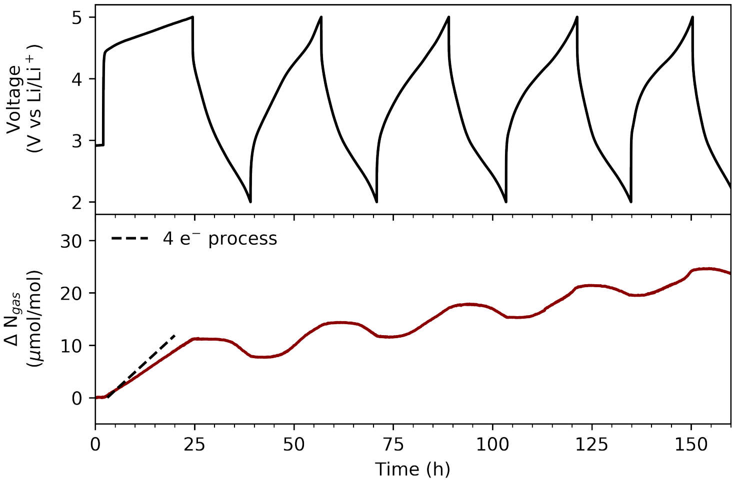

Figure 5.6: Headspace pressure monitoring for the first 5 cycles at C/20 (11.5 mA mg^{-1}) for Li_2MnO_3. The difference in total moles of gas and initial moles of gas contained in the cell headspace at any time is plotted in the bottom panel.

The observed pressure reveals that the cell derives some discharge capacity in a manner similar to a primitive Li-O_2 battery. The pressure rise on the first charge agrees well with the DEMS results, indicating that a sizable fraction of the pressure rise is due to O_2 evolution. On discharge, a clear decrease in total gas contained in the cell headspace is observed below 2.5 V. This is likely caused by the consumption of oxygen evolved during charge, similar to a Li-O_2 battery. Previously studied Li-O_2 batteries utilizing carbonate based electrolytes reveal a near 3 electron process per O_2 consumed on discharge,[15] similar to what is observed in Figure 5.6. This process is entirely irreversible and is related to an electrochemical reaction involving the carbonate solvent, O_2, and Li^+ to form solid Li alkyl carbonates. This process repeats itself to provide additional capacity on subsequent cycles. Note that we do see a greater rate of capacity fade for our cell than previously studied coin cells, which we believe is related to the geometry and greater headspace volume in the set up used for this study. Mn3s XPS measurements also revealed slight Mn reduction on the surface during discharge (SI Figure 5.8) that is likely a participant in the charge compensation above 2.5 V during discharge.

5.5 Conclusions

This study of reactivity at high potentials for LCO, LNO, and LMO leads to a greater understanding of cathode instability, and provides insights for the design of cathodes with greater capacities and higher operating voltages. The major finding for LCO is the lack of evidence for significant oxygen outgassing or oxo-dimer formation, even when the voltage is held at 5 V. This challenges the widely held theory that oxygen loss activated at high potentials is a major cause of capacity fade in the LCO system. When compared to LCO, LNO has much higher native activity towards electrolyte degradation, yet passivates quickly after a couple cycles due to a large deposited carbonate degradation layer. Oxygen release is also very limited for LNO and reactive oxygen (singlet or peroxo-like oxygen) likely contributes only negligibly to electrolyte degradation. It is likely that the growth of a surface carbonate layer results in the cycle-to-cycle interfacial impedance increase typically observed for LNO. Unlike LCO and LNO, LMO's electrochemistry is dominated by irreversible gas release due to oxide oxidation and electrolyte degradation. This study shows that irreversible processes in LMO continue for subsequent cycles, including continued gas evolution and consumption as evidenced by pressure monitoring. Ultimately, this study reveals the high relative stability and limited electrolyte degradation activity of LCO compared to LNO or LMO. To further suppress reactivity in transition metal oxides, a useful strategy is the use of a gradient material with a Co-rich surface while limiting both Ni and Mn near the surface. Such gradient materials have focused primarily on reducing only Ni content at the surface, leaving Mn and Co enriched.[164] These results reveal that Mn(IV) is also likely a key contributor to electrolyte degradation, perhaps even more so than Ni. The direct chemical reactivity of Mn(IV) towards carbonate electrolytes clearly decreases overall material stability, and this chemical reaction is likely the cause of observed reduced surface Mn even after high voltage charges in NMC materials.[165] Other coating layers, such as alumina or titania, may have the benefit of ensuring limited Mn(IV) and Ni(IV) exposure to the electrolyte, and should also continue to be pursued as strategies to further reduce the high voltage reactivity of these transition metal oxides.

5.6 Acknowledgements

Support of this work was provided by the Energy & Biosciences Institute through the EBI-Shell program. This work was also supported by the Graduate Research Opportunities Worldwide (GROW) program with project number 040.15.067, which is partially financed by the National Science Foundation and the Swedish Research Council (SRC). Dr. Ning Li synthesized LCO and LNO as well as performed structural characterization of those materials. Lori Kaufman synthesized the LMO material. Prof. Reza Younesi and Dr. Andrew J. Naylor at Uppsala University offered valuable advice for XPS operation and data analysis. J.K.P. acknowledges support from the National Science Foundation Graduate Research Fellowship under grant no. DGE 1106400.

5.7 Supplementary Information

5.7.1 Carbonate and Peroxo-like Species Titrations

Titrations of powders and electrodes were performed to quantify the amount and isotopic distribution of residual carbonate as well as peroxo-like species. The titration protocol is well-described in previous publications, but a brief overview is presented here. A known amount of TMO powder was placed in a glass cell and attached to the DEMS, afterwhich a baseline was recorded. 1 mL of 10 M H_2SO_4 was then injected into the cell through a septa-sealed port and reacted according to the following reactions:

$$Li_2CO_3 + H_2SO_4 \longrightarrow Li_2SO_4 + H_2O + CO_2 \tag{5.1}$$

.

$$Li_2O_2 + H_2O \longrightarrow 2LiOH + 1/2O_2 \tag{5.2}$$

All gas fragments were monitored with time and integrated to determine the total amount of surface Li_2CO_3 and Li_2O_2-like species. Titrations were performed for LCO, LNO, and LMO. However, titrations of LNO cathodes resulted in excessive O_2 evolution even in their pristine form. Continued studies of this phenomenon suggest that the oxygen evolution is likely coupled to Ni reduction back to its +2 state. Future studies will describe this mechanism in additional detail.

Electrode	O_2 (mmol mol^{-1})	CO_2(mmol mol^{-1})
LCO 5 V	1.8	2.5
LCO 4.6 V	1.6	3.0
LCO OCV	1.1	1.6
LNO 5 V	480	75
LNO OCV	348	42
LMO 5 V	0.8	13
LMO 4.6 V	15.7	41
LMO OCV	0.9	28.0

Table 5.4: Outgassing quantities summarized for 10 M H_2SO_4 titrations of extracted LCO, LNO, and LMO cathodes charged (C/10) and held at various potentials until the current reached C/100 or held at OCV for 24 h.

5.7.2 X-ray Photoelectron Spectroscopy of Cathode Materials

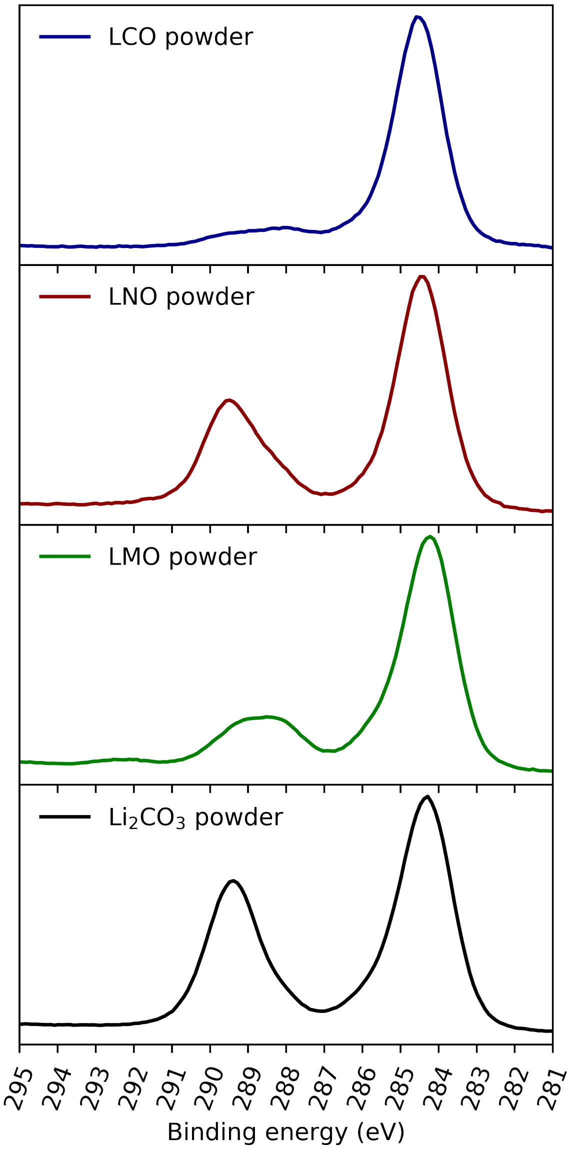

Figure 5.7: C1s XPS spectra gathered for $LiCoO_2$, $LiNiO_2$, Li_2MnO_3, and Li_2CO_3 powders.

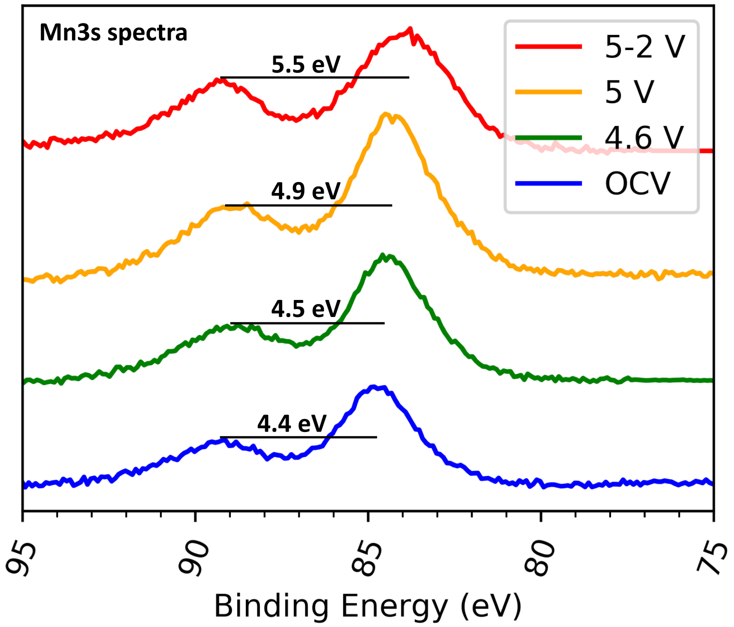

Figure 5.8: Mn3s XPS spectra gathered for Li_2MnO_3 cathodes (OCV, charged to 4.6 V, charged to 5.0 V, and charged to 5.0 V followed by a discharge to 2 V). Increased peak gap between multiplet split components corresponds to reduction of Mn.[166]

Chapter 6

Unusual Oxygen Activity in Partially Substituted Li_2O based Cathode Materials

6.1 Abstract

To mitigate challenges arising from continuous oxygen gas consumption and evolution in Li-O_2 batteries, a highly desirable chemistry would elicit oxygen redox while remaining wholly in the solid phase. Several attempts have been made to create materials that undergo reversible oxygen redox in the solid phase, and one class of materials has been reported with moderate success. High capacities, likely originating from oxygen redox, are observed for minimally transition metal substituted Li_2O Li-ion cathode materials. While Li_2O is not electrochemically active, substitution of a small percentage of the Li with certain transition metals by mechanochemical ball milling results in greatly increased activity. This unusual activity highlights the benefits of an oxygen redox based battery, but also demonstrates additional challenges associated with oxygen activity. In this chapter, Li_2O substituted with Co, Cu, Ni, or Zn by planetary ball milling are examined as cathode materials for lithium batteries. Electrochemical behavior, gas evolution, and the effects of ball milling are discussed for these materials. Studying each transition metal/Li_2O environment aids in elucidating the effect of the transition metal on oxygen redox activity in more traditional Li-ion systems.

6.2 Introduction

While Li-O_2 batteries have extremely high theoretical energy densities (3500 Wh kg^{-1}), a host of challenges accompany their realization. Not least among these challenges is the requirement of a pure oxygen reservoir as atmospheric oxygen is accompanied by detrimental moisture and carbon dioxide, which when exposed to the battery, lead to parasitic side-reactions that reduce the efficiency of the cell. Either a pure oxygen tank or a gas purification system would prohibitively reduce the battery's energy density.[167] Alternative forms of a Li-O_2 battery have been proposed such that these challenges can be avoided by eliminating the need for a pure oxygen gas source.[24,168] One interesting class of materials, which relies on energy storage entirely through solid phase oxygen redox, is composed of small amounts of transition metal substituted in Li_2O.[168–170] This lithium-oxygen type solid phase redox avoids the need for oxygen gas consumption and evolution.[168,169] This transition metal substituted Li_2O material draws on a "Li_2O_2 reservoir" instead of O_2, and still boasts a very large theoretical capacity (2500 Wh kg^{-1}). The overall cell reaction proposed is:

$$2Li^{+} + Li_2O_2 + 2e^{-} \longrightarrow 2Li_2O,\ E_0 = 2.87\,V \tag{6.1}$$

However, the actual electrochemical reactions are likely much more complex and not as straightforward as that shown in equation 6.1. While the desired electrochemistry during material delithiation would involve minimal gas evolution, large quantities of gas evolve during charging of these materials to high capacities. Studies by Mizuno et al.[168,169] have shown that an initial region of electrochemical oxidation without outgassing is possible, but high capacities are always accompanied by sizable oxygen evolution. This proposed material class is intriguing because Li_2O is known to be electrochemically inactive, as a simple Li_2O cathode demonstrates negligible capacity during delithiation attempts to 5 V. The electrochemical activation is then made possible by a substitution of only very small amounts of transition metal (e.g., 1 transition metal atom for every 10 lithium atoms).

Interestingly, the studies presented in this chapter show that the amount of outgassing, as well as the capacity observed, is strongly dependent on the transition metal substituent incorporated. Even neighboring elements on the periodic tables such as Co, Ni, and Cu result in enormous delithiation capacity differences. This chapter focuses on a series of materials incorporating Li_2O substituted with Co, Cu, Ni or Zn by mechanochemical planetary ball milling synthesis. The synthesis methods are similar to those used for Li-excess Li-ion cathode materials, but instead utilize only Li_2O and small amounts of transition metal oxide as precursors. Some of the resulting cathode materials exhibit enhanced electrochemical activity that is accompanied by unusual outgassing. The study of these materials has not yet resulted in a battery any more practical than a typical Li-O_2 battery, but instead has demonstrated the importance of a greater understanding of transition metal influence on oxygen activity in Li-ion battery cathode materials.

6.3 Experimental Methods

6.3.1 Materials Preparation and Characterization

Transition metal substituted Li_2O was synthesized similarly to previous studies by mechanochemical planetary ball milling. The precursor materials for each composite were first placed in a zirconia milling pot with zirconia milling balls in an Ar-filled glovebox. After loading, the composites were mechanochemically synthesized using a Restch PM100 planetary ball mill. The Cu substituted Li_2O composites were made using CuO and Li_2O precursors such that the elemental ratio of Cu to Li was 1:10 (1.88 g Li_2O per 1 g CuO) or 3:10 (0.63 g Li_2O per 1 g CuO). Co substituted Li_2O used Co_3O_4 as the Co source for a Co:Li elemental ratio of 1:10 (1.86 g Li_2O per 1 g Co_3O_4). Ni substituted Li_2O utilized NiO as the Ni source with a Ni:Li elemental ratio of 1:10 (2.0 g Li_2O per 1 g NiO). Finally, ZnO was used as the Zn source for Zn substituted Li_2O such that again the Zn:Li elemental ratio was 1:10 (1.84 g Li_2O per 1 g ZnO). After milling, the resulting powder was removed in the Ar-filled glovebox before characterization or measurements were performed.

To examine the effectiveness of ball milling, powder X-ray diffraction (XRD) was performed. Powder XRD is shown in Figure 6.1 for Cu substituted Li_2O during synthesis at various milling times. The measurements show the effect of milling in eliminating the CuO phase. After 50 h of ball milling, only a single broad peak at 34^o is observed, which is ascribed to Li_2O (111), indicating full integration of Cu into the Li_2O crystal lattice, in agreement with literature results.[170] Based on the XRD results, it can be assumed that first the CuO reacts with Li_2O to form a Li_2CuO_2 phase that then continues to react to form Cu-doped Li_2O at longer milling times. The exact structure of the synthesized material is unknown, although Kobayashi et al.[170] who worked with a similar material theorize that the arrangement of oxide ions surrounding the copper ion are distorted slightly from tetrahedral to square-planar. The broadened peaks of the XRD measurements of milled samples also indicate that the final material has poor crystalinity. Scanning electron microscopy (SEM) images were also taken that show the powder size after milling the Cu substituted Li_2O composite (Figure 6.2). From the SEM images, the primary particle size was estimated to be 3-5 μm in secondary agglomerates of 30-250 μm.

6.3.2 Electrochemistry

The transition metal substituted Li_2O and pure Li_2O cathodes were made by first mixing with conductive carbon black and a polytetrafluoroethylene (PTFE) binder, typically in a 70:20:10 weight ratio. Mixing of carbon was performed by either extended ball milling after the addition of carbon black, or by thoroughly mixing using a mortar and pestle. PTFE binder was always incorporated immediately prior to forming electrodes using a mortar and pestle. The mixture for each material was then pressed and rolled onto stainless steel mesh (1 cm^2). Finally, electrochemical cells were assembled by stacking prepared cathodes with

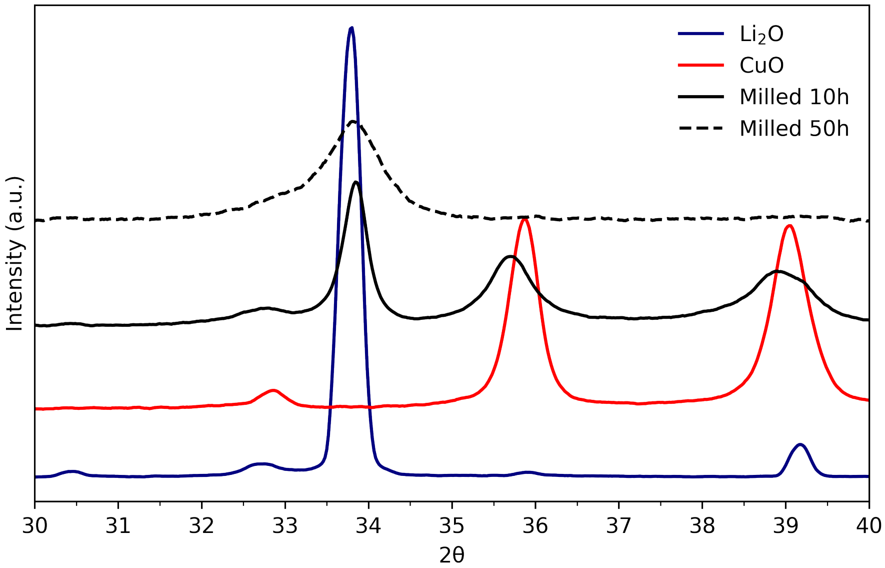

Figure 6.1: XRD measurements for pristine Li_2O, pristine CuO, the composite ball milled for 10 h, and the composite ball milled for 50 h. The Cu substituted composite had an elemental ratio of Cu:Li = 1:10

1M $LiPF_6$ EC:DEC electrolyte soaked glass fiber separators and Li metal anodes. Cell casings and current collectors were of modified Swagelok design, as described in previous publications.[41,57]

6.3.3 Differential Electrochemical Mass Spectrometry and Pressure Rise/Decay Measurements

A differential electrochemical mass spectrometer (DEMS) was used to identify and quantify oxygen and carbon dioxide evolved during charging and discharging. Other gases (H_2, CO) comprised only a minor fraction of total gas evolution. The custom-built DEMS and the cell geometry used was described in depth in previous publications.[41,57] The electrochemical cells used with the DEMS device were prepared in a dry argon glove box (<1 ppm O_2 and H_2O, MBraun USA, Inc.) using a custom Swagelok design. 1 M $LiPF_6$ in 1:1 (volume ratio) ethylene carbonate (EC) and diethyl carbonate (DEC) was used as the electrolyte, glass microfiber filters were used as separators, and Li metal foil was used as the counter electrode.

The assembled cells were charged under a static head of positive argon pressure (∼1.2 bar) after being appropriately attached to the DEMS. Throughout the charge, argon gas pulses periodically swept accumulated gases to a mass spectrometer chamber. The mass

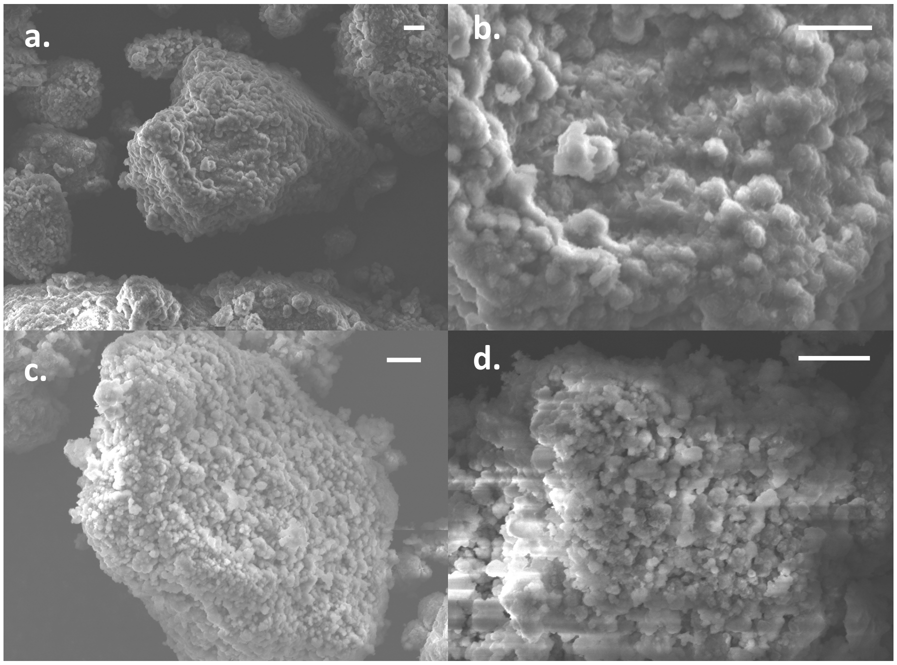

Figure 6.2: SEM images taken of Cu substituted Li_2O (Cu:Li = 1:10) where each scale bar (top right of each image) is 10 μm

spectrometer absolute sensitivity was calibrated for CO_2 and O_2, and therefore the partial pressures of these gases could be determined. The amount of CO_2 and O_2 evolved was then quantified based on the volume of gas swept to the mass spectrometer per pulse.

Total gas evolution can also be quantified by monitoring pressure rise/decay in an isolated cell headspace.[163] Using the same gas handling unit and cell as the DEMS, the attached cell is valved off from the gas inlet, and an in-line pressure transducer records pressure measurements within the closed cell headspace. The cell headspace volume is calibrated using gas expansion in combination with sample loops of known volumes such that the total gas within the cell at any time can be calculated.

6.4 Results and Discussion

Synthesis (ball milling) effects, electrochemistry, and outgassing were investigated for Cu, Co, Ni, and Zn substituted Li_2O cathodes. Measurements presented reveal key differences between the effects of the substituted transition metals, as well as general trends for this type of material. Results are divided into sections discussing the results first for pure Li_2O and Li_2O with Cu substitution followed by Co substituted Li_2O, and finally a brief discussion of

Ni and Zn substituted Li_2O. Broad comparisons between materials and potential directions of future study are discussed in the conclusion of this chapter.

6.4.1 Li_2O and Cu Substituted Li_2O

Li_2O is known to be electrochemically inactive as shown in studies of Li-O_2 batteries.[15] However, due to the surprising studies mentioned in the section above,[168,170] where a small (<10 mol%) inclusion of transition metal ions into the Li_2O structure allowed reversible solid state oxygen redox, a simple control was performed on cathodes made using ball milled pure Li_2O as the active material, mixed with carbon black and PTFE binder. Cells comprised of these pure Li_2O electrodes were then attached to a gas handling system that allows the headspace pressure to be monitored. Results of the pressure rise/decay measurements are shown for a single charge-discharge cycle between 4.7 - 1.5 V in Figure 6.3. At a charge rate of 50 mA g^{-1}, the Li_2O cathode had a charging capacity of 30 mAh g^{-1} and a discharge capacity of ~10 mAh g^{-1}. A small increase in headspace pressure was observed beginning at ~4.1 V, roughly the potential at which any adventitious carbonates are expected to oxidize to evolve CO_2.[92] The total molar evolution during charge corresponded to only .07 μmol mg^{-1}, an almost negligible amount of gas evolution. On discharge, the monitored pressure was observed to decrease, indicating a slight consumption (0.05 μmol mg^{-1}) of any gas evolved during charge. These measurements clearly show that cathodes made of pure Li_2O have insignificant electrochemical activity, particularly compared to some of the materials discussed below.

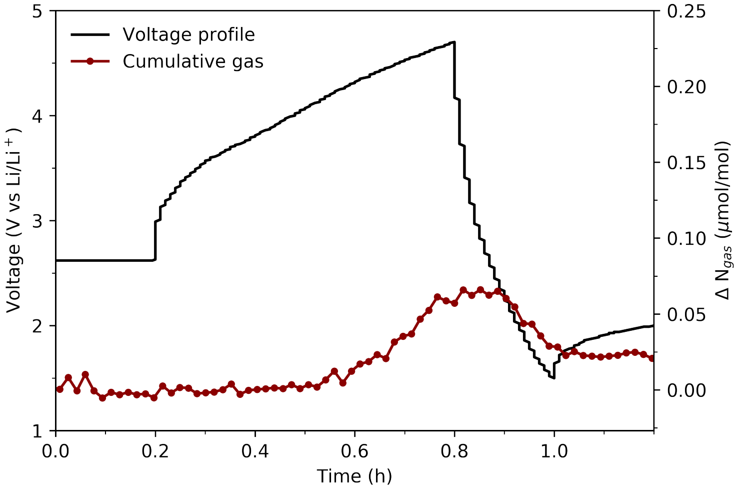

Figure 6.3: Gas evolution and consumption during first cycle of pure, ball-milled Li_2O based electrode (50 mA g^{-1}). Gas evolution and consumption was monitored using pressure rise/decay in a cell of known headspace volume.

Cu-substituted Li_2O was then synthesized as described in detail in the Experimental Methods section, with ball milling time as the variable. Prepared materials were then used to make cathodes that were then electrochemical analyzed. Cells comprised of the Cu-substituted Li_2O cathodes and Li metal anodes were cycled at 20 mA g^{-1} (4.0 - 1.5 V potential window, Figure 6.4). A clear trend is observed of increasing first charge (and discharge) capacity with increasing mill times. For example, the material milled for 5 hours only demonstrated a capacity of 32 mAh g^{-1}, while the sample milled for 35 hours reached over 265 mAh g^{-1}. The influence of mill time on observed capacity seems to indicate an activation of the electrochemical activity of Li_2O by phase disruption of the substituted transition metal (Cu). Observed XRD patterns for similar materials indicate that the room temperature milling and low CuO content during synthesis produce a Li_2O structure with low crystallinity in which Cu ions to distort the Li_2O structure slightly from tetrahedral to square planar.[170] These distortions might raise oxygen orbital energy levels to allow for oxygen redox participation, but additional structural characterization is needed. In addition to ball milling duration, the Cu/Li ratio in the material was also varied, and composites of Cu substitution Cu:Li = 3:10 (mol:mol) were found to have slightly greater charge capacity and used for more detailed electrochemical analysis as follows.

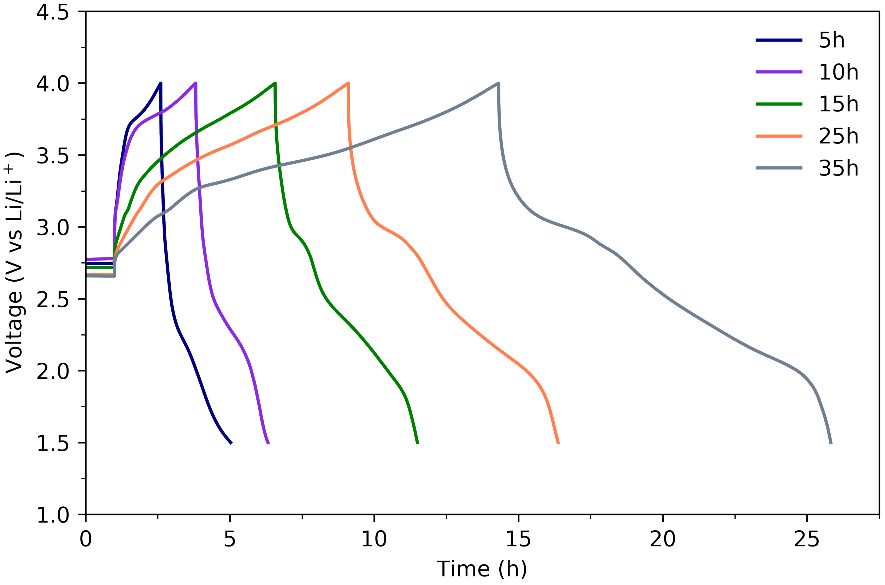

Figure 6.4: First cycle capacities for Cu substituted Li_2O (Cu:Li = 1:10) at various ball milling duration during material synthesis (20 mA g^{-1}, 4.0 - 1.5 V).

A galvanostatic intermittent titration technique (GITT) measurement was also performed for Cu-substitued Li_2O such that 30 minutes of applied current was followed by 3 hours of cell relaxation (Figure 6.5a). On charge, two clear plateaus are observed, the first is accessed in the initial 300 mAh g^{-1} capacity and has a corresponding potential of 3.4 V, and then the second plateau commences at ~400 mAh g^{-1} with an average voltage of 4.1 V. Polarization is shown to increase with greater capacity extracted on charge (i.e., at capacities greater than 4 V). On discharge, a gently sloping voltage profile is observed until the voltage cutoff, which occurs at roughly half the capacity of the charge as a result of increasing polarization. The GITT measurement suggests a single reversible electrochemically active phase, and a degradation mechanism that is activated in the upper voltage region on charge. Unfortunately, as is shown in Figure 6.5b, both charge plateaus are actually related to irreversible gas evolving processes.

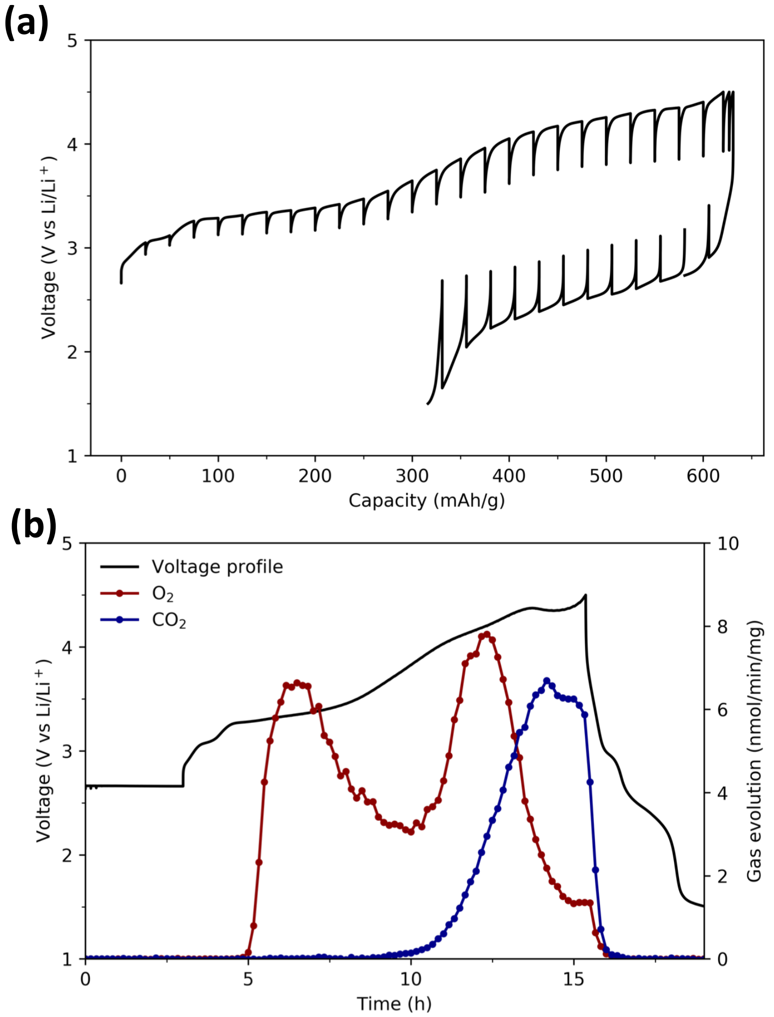

Figure 6.5: (a) GITT measurement and (b) gas evolution during charging (50 mA g^{-1}) of Cu substituted Li_2O (Cu:Li = 3:10).

Figure 6.5b presents outgassing for Cu substituted Li_2O charged at 50 mA g^{-1} up to 4.5 V. The charging capacity was observed to be 618 mAh g^{-1}, of which Cu^{2+}/Cu^{3+} redox could account for up to 115 mAh g^{-1}. A study of Li_2CuO_2 showed that lithium extraction from that material proceeds to $LiCuO_2$ via $Li_3Cu_2O_4$, and therefore a Cu oxidation state of $> 2.5+$ (and a capacity contribution of > 57 mAh g^{-1}) is unlikely.[171] Oxygen outgassing began at roughly 108 mAh g^{-1}, suggesting that Cu^{2+}/Cu^{3+} redox accounted for the initial cell capacity. The evolution appears to be bimodal such that the rate of evolution quickly peaks, drops back to roughly half the max rate, and then peaks again as 4 V is reached. The evolution of oxygen at such low potentials as 3.3 V is unusual for Li-ion batteries, and is reminiscent of charging in a Li-O_2 battery, where Li_2O_2 is oxidized to oxygen gas. The total oxygen evolved during charge was 2.77 μmol O_2 per mg active material, and evolved at a near 4 electron rate (7.8 nmol min^{-1} mg^{-1}) at the peak rates. Additionally, large amounts of CO_2 evolution were observed toward the end of charge (1.25 μmol CO_2 per mg active material), indicating that severe electrolyte degradation occurs at these high voltages, reminiscent again of a carbonate electrolyte-based Li-O_2 battery.[15] These results indicate that this material's electrochemistry is dominated by irreversible gas release beyond the expected Cu redox. Nevertheless, it is intriguing that such substantial O_2 release is observed from this material given the relative inactivity of pure Li_2O. In an attempt to understand the origin of this gas release, additional materials were synthesized utilizing substitutions of other transition metals.

6.4.2 Co Substituted Li_2O

Co substituted Li_2O was synthesized via 35 h ball milling of Co_3O_4 and Li_2O in a ratio that result in a 1:10 Co:Li molar ratio. Similar Co substituted Li_2O has previously been reported to exhibit reversible capacities of 190 mAh g^{-1} with little gas evolution up to 3.6 V.[168] The reversible capacities are claimed to be contributed almost entirely by equation 6.1.

In this study, the synthesized Co substituted Li_2O exhibited a charge capacity of 610 mAh g^{-1} up to a voltage cutoff of 4 V at a rate of 50 mA g^{-1}(Figure 6.6a). However, DEMS measurements for this material determined that O_2 evolution began almost immediately upon applying current (corresponding to voltages as low as 3.5 V). Another key difference between the study here and that performed by Okuoka et al. is the potential at the first plateau during charging. The referenced study reports an initial plateau at only 3.1 V,[168] while it was observed here that a plateau is not reached until 3.5 V. These differences highlight an important difficulty of mechanochemical synthesis: the near impossibility to completely replicate synthesis conditions. Planetary ball milling involves a large number of variables including size and utilized volume of the milling jar, the size and number of milling balls, speed and time of milling, as well as numerous mill settings such as cooling breaks and rotation direction changes. While the electrochemical activity was not exactly the same as reported in previous literature,[168] the achieved material and activity is still of great interest due to the large capacities and gas evolution observed. Gas evolution for Co-substituted Li_2O was composed primarily of O_2, and evolved at slightly above an 8 electron rate (0.0039

μmol min^{-1} mg^{-1}). Near the voltage cutoff at ~3.9 V, CO_2 evolution is also observed. The total amounts of gas evolution are 2.86 μmol mg^{-1} for O_2 and 0.07 μmol mg^{-1} for CO_2.

O_2 evolution observed in Co substituted Li_2O, similarly to Cu substituted Li_2O, has to be due to oxidation of oxygen in the active material that leads to irreversible gas evolution. However, the 8 electron process observed for O_2 evolution indicates that charging capacity cannot be attributed completely to irreversible oxygen evolution as in the case of a 4 electron process. The charge contribution for this Co substituted Li_2O therefore remains in question, with the most likely capacity origins being formation of semi-stable peroxo-like species, or the formation of degradation products that remain in the liquid or solid phase. The small amount of CO_2 observed likely originates from electrolyte degradation that is known to begin at ~3.9 V for EC:DEC solvent mixtures.

A Co substituted Li_2O cell was also then cycled at 100 mA g^{-1} five times between 4.5 - 1.5 V while the headspace pressure was monitored (Figure 6.6b). A very large first charge capacity of over 1400 mAh g^{-1} is observed when the voltage cutoff is raised to 4.5 V, however no substantial discharge capacity was observed for Co substituted Li_2O for cells charged to 4 or 4.5 V. The lack of any significant discharge capacity indicates that all charge compensation during charging is due to irreversible processes. Pressure monitoring demonstrates again that gas evolution proceeds at a steady and significant rate near that of an 8 electron process for the entire charge. The pressure drop on discharge also indicates that gas, most likely O_2 akin to a primitive Li-O_2 battery, is consumed and contributes almost the entire observed discharge capacity.

Co substitution in Li_2O clearly promotes oxygen activity, an interesting finding due to the lack of oxygen activity observed for $LiCoO_2$ as discussed in the previous chapter. Additional study is therefore warranted for Co substitution in Li_2O to more clearly understand oxygen activity in similar materials. While not undertaken in this study, titrations similar to those discussed in previous chapters that probe the peroxo-like species present would be useful here. The effect of electrolyte also likely plays an important role. Okuoka et al. report using a superconcentrated 4 M LiFSA electrolyte in acetonitrile, while the findings present here utilized a simple 1 M LiPF6 EC:DEC electrolyte. The differences observed between the two studies might be partially due to the choice of electrolyte, and further investigation would be valuable. Study of the reactivity of oxidized oxygen in this material with the utilized electrolyte would also be valuable. Unfortunately due to the extreme irreversible oxygen outgassing of these materials (both the Cu- and Co- substituted materials), their use as practical battery materials is unlikely.

6.4.3 Ni and Zn Substituted Li_2O

Ni and Zn substituted Li_2O materials were also synthesized by ball milling NiO or ZnO with Li_2 to produce a powder with a 1:10 transition metal:Li ratio. Both Ni and Zn substituted

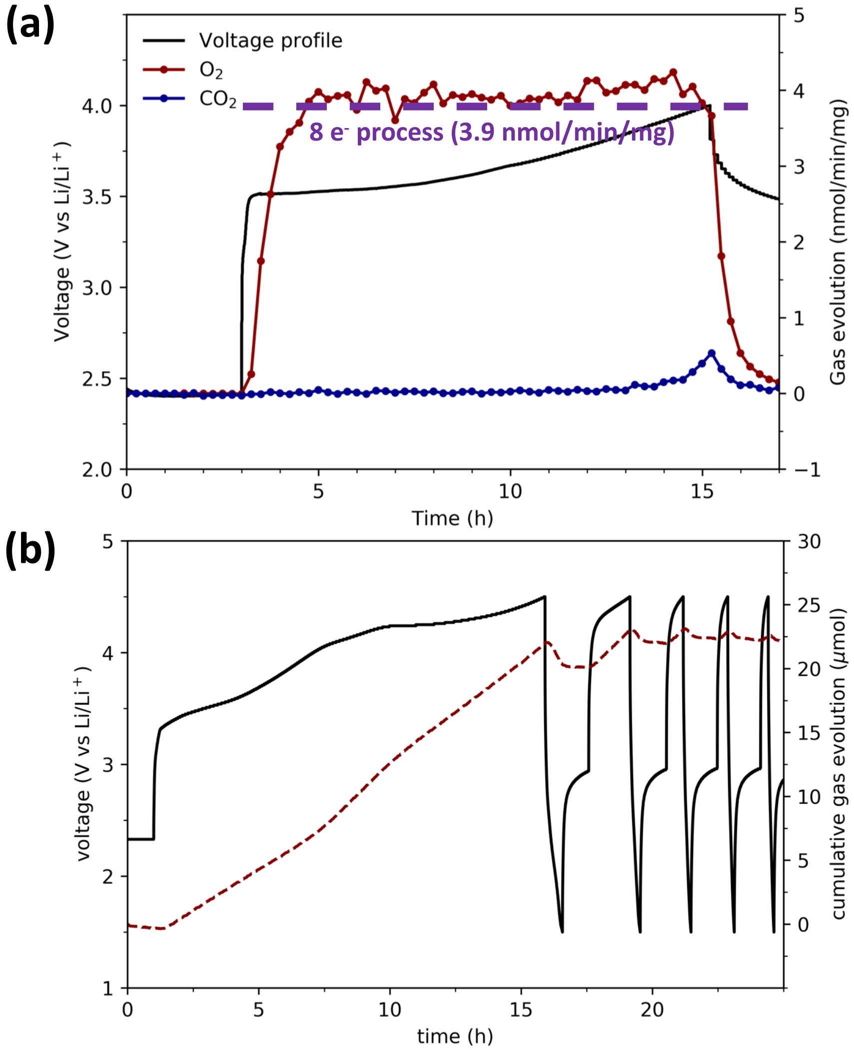

Figure 6.6: (a) Gas evolution during charging (50 mA g-1) and (b) pressure monitoring during the first five cycles (100 mA g-1) of Co substituted Li_2O (Co:Li = 1:10).

Li_2O did not exhibit significant electrochemical capacities, even when milled for extended periods of time (> 35 h). Ni substituted Li_2O headspace pressure measurements were taken during the first 4 cycles of charge/discharge between 4.8-1.5 V (Figure 6.7), and only ∼25 mAh g-1 was observed on charge, and < 10 mAh g-1 on the first discharge, making their electrochemical performance nearly identical to unsubstituted Li_2O. Capacities decreased on subsequent cycles, indicating that no practical Li extraction occurs in this material. Zn substituted Li_2O produced similar results and, which are not shown. The capacities for both Ni and Zn substituted Li_2O are no greater than observed for unsubstituted Li_2O electrodes.

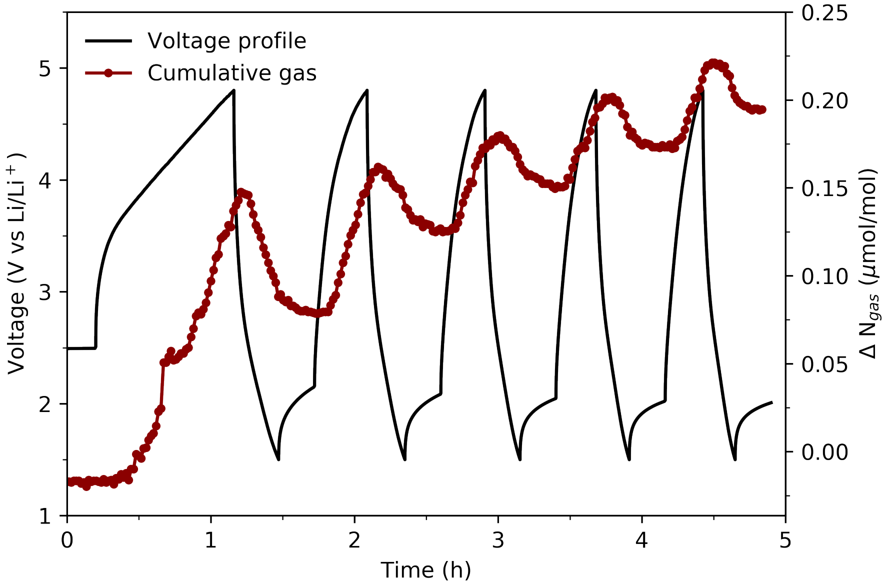

Figure 6.7: Gas evolution measured via pressure monitoring of the cell headspace during first three cycles of Ni-substituted Li_2O (Ni:Li = 1:10) at 50 mA g^{-1}.

The lack of observed charging capacity for Ni and Zn substituted Li_2O is significant given the large capacities observed for the similarly synthesized Cu and Co substituted materials. It is appears that simple disruption of the Li_2O structure is not sufficient to induce oxygen activity, but that specific transition metals are conducive to promoting it.

6.5 Conclusions

The measurements presented in this chapter demonstrate that Li_2O substituted with even very small amounts of transition metal can become activated for oxygen redox. The activation does not occur for every transition metal, and a large disparity in observed first charge and first discharge capacities are observed for different transition metals (Table 6.1).

The result of the electrochemical activation and gained capacity is, unfortunately, accompanied by significant quantities of oxygen loss and, in the case of the highest capacity material (that with Co substitution), significant CO_2 evolution from electrolyte degradation. This oxygen loss has been quantified and analyzed here for several transition metal substitutions. Copper substitution of Li_2O results in the most substantial reversible capacities among the transition metals studied, and is likely related to $Cu^{2+/3+}$ redox. First charge capacities as great as 618 mAh g^{-1} have been determined for Cu substituted Li_2O,, of which irreversible oxygen outgassing occurred at varying rates across the charge and accounted for nearly 300

Material	**1st charge capacity (mAh g^{-1})**	**1st discharge capacity (mAh g^{-1})**	**Voltage Range**
Li_2O	30	10	4.7 - 1.5
Cu substituted	618	235	4.5 - 1.5
Co substituted	1450	70	4.5 - 1.5
Ni substituted	48	15	4.7 - 1.5
Zn substituted	33	15	4.5 - 1.5

Table 6.1: Observed first charge and first discharge capacities for transition metal substituted Li_2O.

mAh g^{-1}. Co substituted Li_2O displayed a very large charge capacity, but irreversible oxygen outgassing at a near constant rate accounted for roughly half of the observed capacity. Both Ni^{2+} and Zn^{2+} substitution resulted in negligible capacity increases over unsubstituted Li_2O. This study revealed the importance of a greater understanding of the influence of transition metal effects on oxygen redox. Research on transition metal substituted Li_2O should continue to more clearly identify the electronic effects and structural changes associated with the substitution, which could potentially provide insight into strategies to harness oxygen redox activity in more conventional layered transition metal oxide cathode materials.

Chapter 7

Conclusion

This dissertation explored the high voltage reactivity in several types of lithium battery chemistries. The studies presented in the previous chapters focused on reactivity as detected by outgassing, particularly in the first electrochemical cycle. By combining gas evolution measurement techniques with additional characterization, the high voltage instabilities of Li-O_2 battery cathodes, Li-excess disordered rock salt cathodes, and more traditional layered transition metal oxide cathodes were thoroughly analyzed.

The first study presented in this dissertation analyzed the instability of the fluorine based electrode binder, poly(vinylidene fluoride) (PVDF), in the presence of the Li-O_2 battery discharge product, lithium peroxide (Li_2O_2), and its reactive intermediates. Of particular importance, when impurities (e.g., water and N-methyl pyrrolidone) are not rigorously removed from porous carbon electrodes during their preparation, the PVDF binder will degrade to form a Raman spectroscopy-active product. The Raman signatures reported for this product can be easily confused for Raman signatures of lithium superoxide (LiO_2), a discharge product that has been reported to stably form at iridium electrodes, but is not stable at room temperature (making this prior report rather surprising).[47] It was shown that only a 2 e^-/O_2 process actually occurs at iridium electrodes to form Li_2O_2, making the degradation of PVDF a key artifact when characterizing the formation products of Li-O_2 batteries. If PVDF-bound cathodes are rigorously dried prior to their integration into cells, no such Raman artifacts were observed, although to entirely avoid ambiguity in the assignment of spectroscopic signatures, the use of alternative binders, such as polytetrafluoroethylene, is encouraged.

Another important finding presented here was that Li-excess disordered rocksalt materials not only provide extremely high capacities in Li-ion batteries, but that high voltage oxygen release can be mitigated by fluorine substitution and incorporation of high valent cations. Capacity retention during cycling was also shown to benefit from fluorine substitution due to reduced oxygen activity and resulting cathode degradation. These findings encourage the search for high capacity lithium ion battery cathode materials consisting of lithium excess disordered rocksalts.

Reactivity at high potentials was also explored in layered transition metal oxides. While materials like $LiCoO_2$ (LCO) and $LiNiO_2$ (LNO) are extremely well studied, the high voltage instability mechanisms of these materials remain poorly understood. In Chapter 5, it was determined that despite material phase changes and theorized oxygen dimerization at high voltages, little oxygen outgassing occurs for either LCO or LNO. Reactivity was also studied for layered lithium-rich Li_2MnO_3 in Chapters 4 and 5, and it was determined that oxygen evolution takes the primary role of charge compensator during the first charge and that dominant irreversible processes continue across many cycles.

Finally, unusual oxygen activity and outgassing was detected in Li_2O cathodes with minor transition metal substitution. This oxygen activity was unexpected as Li_2O is generally electrochemically inactive. The observed trends for induced activity with small quantities of transition metal substitution inspires additional study to understand the role of transition metal coordination for oxygen activity.

Bibliography

[1] J. B. Goodenough and Y. Kim. “Challenges for rechargeable Li batteries”. *Chemistry of Materials* 22.3 (2010), pp. 587–603.

[2] J. M. Tarascon and M. Armand. “Issues and challenges facing rechargeable lithium batteries”. *Materials for Sustainable Energy: A Collection of Peer-reviewed Research and Review Articles from Nature Publishing Group*. World Scientific, 2011, pp. 171–179.

[3] J. M. Tarascon and M. Armand. “Issues and challenges facing rechargeable lithium batteries”. *Nature* 414.6861 (Nov. 2001), pp. 359–367. ISSN: 1476-4687.

[4] M. Broussely et al. “Li_xNiO_2, a promising cathode for rechargeable lithium batteries”. *Journal of Power Sources* 54.1 (1995), pp. 109–114.

[5] M. D. Radin et al. “Narrowing the gap between theoretical and practical capacities in Li-ion layered oxide cathode materials”. *Advanced Energy Materials* 7.20 (2017), p. 1602888.

[6] G. G. Amatucci, J. M. Tarascon, and L. C. Klein. “CoO_2, the end member of the Li_xCoO_2 solid solution”. *Journal of The Electrochemical Society* 143.3 (1996), p. 1114.

[7] J. N. Reimers and J. R. Dahn. “Electrochemical and in situ X-ray diffraction studies of lithium intercalation in Li_xCoO_2”. *Journal of the Electrochemical Society* 139.8 (1992), p. 2091.

[8] T. Ohzuku and A. Ueda. “Solid-state redox reactions of $LiCoO_2$ (R3m) for 4 volt secondary lithium cells”. *Journal of The Electrochemical Society* 141.11 (1994), p. 2972.

[9] T. Ohzuku, A. Ueda, and M. Nagayama. “Electrochemistry and structural chemistry of $LiNiO_2$ (R3m) for 4 volt secondary lithium cells”. *Journal of the Electrochemical Society* 140.7 (1993), p. 1862.

[10] J. R. Dahn, U. von Sacken, and C. A. Michal. “Structure and electrochemistry of $Li_{1\pm y}NiO_2$ and a new Li_2NiO_2 phase with the $Ni(OH)_2$ structure”. *Solid State Ionics* 44.1-2 (1990), pp. 87–97.

[11] M. M. Thackeray, A. de Kock, and W. I. F. David. “Synthesis and structural characterization of defect spinels in the lithium-manganese-oxide system”. *Materials Research Bulletin* 28.10 (1993), pp. 1041–1049.

[12] J. M. Tarascon et al. “The spinel phase of $LiMn_2O_4$ as a cathode in secondary lithium cells”. *Journal of the Electrochemical Society* 138.10 (1991), p. 2859.

[13] F. Schipper and D. Aurbach. “A brief review: past, present and future of lithium ion batteries”. *Russian Journal of Electrochemistry* 52.12 (2016), pp. 1095–1121.

[14] G. Girishkumar et al. “Lithium-air battery: promise and challenges”. *The Journal of Physical Chemistry Letters* 1.14 (2010), pp. 2193–2203.

[15] B. D. McCloskey et al. “Solvents’ critical role in nonaqueous lithium–oxygen battery electrochemistry”. *The Journal of Physical Chemistry Letters* 2.10 (2011), pp. 1161–1166.

[16] V. Viswanathan et al. “Electrical conductivity in Li_2O_2 and its role in determining capacity limitations in non-aqueous Li-O_2 batteries”. *The Journal of Chemical Physics* 135.21 (2011), p. 214704.

[17] C. C. Chan and Y. S. Wong. “Electric vehicles charge forward”. *IEEE Power and Energy Magazine* 2.6 (2004), pp. 24–33.

[18] J. O. Besenhard and H. P. Fritz. “Cathodic reduction of graphite in organic solutions of alkali and NR4+ salts”. *Journal of Electroanalytical Chemistry and Interfacial Electrochemistry* 53.2 (1974), pp. 329–333.

[19] A. Kraytsberg and Y. Ein-Eli. “Higher, stronger, better… A review of 5 volt cathode materials for advanced lithium-ion batteries”. *Advanced Energy Materials* 2.8 (2012), pp. 922–939.

[20] D. Aurbach et al. “Review on electrode–electrolyte solution interactions, related to cathode materials for Li-ion batteries”. *Journal of Power Sources* 165.2 (2007), pp. 491–499.

[21] P. Rozier and J. M. Tarascon. “Li-rich layered oxide cathodes for next-generation Li-ion batteries: chances and challenges”. *Journal of The Electrochemical Society* 162.14 (2015), A2490.

[22] A. R. Armstrong et al. “Demonstrating oxygen loss and associated structural reorganization in the lithium battery cathode $Li[Ni_{0.2}Li_{0.2}Mn_{0.6}]O_2$”. *Journal of the American Chemical Society* 128.26 (2006), pp. 8694–8698.

[23] M. Sathiya et al. “Reversible anionic redox chemistry in high-capacity layered-oxide electrodes”. *Nature Materials* 12.9 (2013), pp. 827–835.

[24] Z. Zhu et al. “Anion-redox nanolithia cathodes for Li-ion batteries”. *Nature Energy* 1.8 (2016), pp. 1–7.

[25] L. Trahey et al. “Energy storage emerging: A perspective from the Joint Center for Energy Storage Research”. *Proceedings of the National Academy of Sciences* 117.23 (2020), pp. 12550–12557.

[26] Y. Ding et al. “Automotive Li-ion batteries: current status and future perspectives”. *Electrochemical Energy Reviews* 2.1 (2019), pp. 1–28.

[27] N. Nitta et al. “Li-ion battery materials: present and future”. *Materials Today* 18.5 (2015), pp. 252–264.

[28] J. Christensen et al. “A critical review of Li/air batteries”. *Journal of the Electrochemical Society* 159 (2012), R1.

[29] A. C. Luntz and B. D. McCloskey. “Nonaqueous Li air batteries: a status report”. *Chemical Reviews* 114 (2014), p. 11721.

[30] D. Aurbach et al. “Advances in understanding mechanisms underpinning lithium-air batteries”. *Nature Energy* 1 (2016), p. 16128.

[31] N. B. Aetukuri et al. “Solvating additives drive solution-mediated electrochemistry and enhance toroid growth in non-aqueous Li–O_2 batteries”. *Nature Chemistry* 7.1 (2015), pp. 50–56.

[32] C. O. Laoire et al. “Influence of nonaqueous solvents on the electrochemistry of oxygen in the rechargeable lithium-air battery”. *The Journal of Physical Chemistry C* 114 (2010), p. 9178.

[33] C. O. Laoire et al. “Elucidating the mechanism of oxygen reduction for lithium-air battery Applications”. *The Journal of Physical Chemistry C* 113 (2009), p. 20127.

[34] L. Johnson et al. “The role of LiO_2 solubility in O_2 reduction in aprotic solvents and its consequences for Li-O_2 batteries”. *Nature Chemistry* 6 (2014), p. 1091.

[35] Z. Peng et al. “Oxygen reactions in a non-aqueous Li^+ electrolyte”. *Angewandte Chemie* 50 (2011), p. 6351.

[36] A. C. Luntz et al. “Tunneling and polaron charge transport through Li_2O_2 in Li–O_2 batteries”. *The Journal of Physical Chemistry Letters* 4.20 (2013), pp. 3494–3499.

[37] V. Viswanathan et al. “Electrical conductivity in Li_2O_2 and its role in determining capacity limitations in non-aqueous Li-O_2 batteries”. *The Journal of Chemical Physics* 135 (2011), p. 214704.

[38] J. S. Hummelshoj et al. “Elementary oxygen electrode reactions in the aprotic Li-air battery”. *The Journal of Chemical Physics* 132 (2010), p. 071101.

[39] O. Gerbig, R. Merkle, and J. Maier. “Electron and ion transport in Li_2O_2”. *Advanced Materials* 25 (2013), p. 3129.

[40] B. D. McCloskey et al. “Combining accurate O_2 and Li_2O_2 assays to separate discharge and charge stability limitations in nonaqueous Li-O_2 batteries”. *The Journal of Physical Chemistry Letters* 4 (2013), p. 2989.

[41] B. D. McCloskey et al. “Limitations in rechargeability of Li-O_2 batteries and possible origins”. *The Journal of Physical Chemistry Letters* 3 (2012), p. 3043.

[42] V. S. Bryantsev et al. “The identification of stable solvents for nonaqueous rechargeable Li-air batteries”. *Journal of the Electrochemical Society* 160 (2013), A160.

[43] V. S. Bryantsev et al. “Predicting solvent stability in aprotic electrolyte Li–air batteries: nucleophilic substitution by the superoxide anion radical ($O_2^{\bullet-}$)”. *The Journal of Physical Chemistry A* 115.44 (2011), pp. 12399–12409.

[44] M. Leskes et al. “Direct detection of discharge products in lithium–oxygen batteries by solid-state NMR spectroscopy”. *Angewandte Chemie* 124.34 (2012), pp. 8688–8691.

[45] M. Leskes et al. “Monitoring the electrochemical processes in the lithium–air battery by solid state NMR spectroscopy”. *The Journal of Physical Chemistry C* 117.51 (2013), pp. 26929–26939.

[46] H. K. Lim et al. “Toward a lithium–“air” battery: the effect of CO_2 on the chemistry of a lithium–oxygen cell”. *Journal of the American Chemical Society* 135.26 (2013), pp. 9733–9742.

[47] J. Lu et al. “A lithium-oxygen battery based on lithium superoxide”. *Nature* 529 (2016), p. 377.

[48] D. Zhai et al. “Interfacial effects on lithium superoxide disproportionation in Li-O_2 batteries”. *Nano Letters* 15 (2015), p. 1041.

[49] J. Yang et al. “Evidence for lithium superoxide-like species in the discharge product of a Li-O_2 battery”. *Physical Chemistry Chemical Physics* 15 (2013), p. 3764.

[50] D. Zhai et al. “Raman evidence for late stage disproportionation in a Li-O_2 battery”. *The Journal of Physical Chemistry Letters* 5 (2014), p. 2705.

[51] L. Andrews. “Matrix infrared spectrum and bonding in lithium superoxide molecule LiO_2”. *Journal of the American Chemical Society* 90 (1968), p. 7368.

[52] B. D. McCloskey et al. “Mechanistic insights for the development of Li-O_2 battery materials: addressing Li_2O_2 conductivity limitations and electrolyte and cathode instabilities”. *ChemComm* 51 (2015), p. 12701.

[53] T. A. Galloway and L. J. Hardwick. “Utilizing in situ electrochemical SHINERS for oxygen reduction reaction studies in aprotic electrolytes”. *The Journal of Physical Chemistry Letters* 7 (2016), p. 2119.

[54] W. S. Hummers and R. E. Offeman. “Preparation of graphitic oxide”. *Journal of the American Chemical Society* 80 (1958), p. 1339.

[55] Y. Xu et al. “Self-assembled graphene hydrogel via a one-Step hydrothermal process”. *ACS Nano* 4 (2010), p. 4324.

[56] S. Kumar, S. Chinnathambi, and N. Munichandraiah. “Ir nanoparticles-anchored reduced graphene oxide as a catalyst for oxygen Electrode in Li-O_2 Cells”. *New Journal of Chemistry* 39 (2015), p. 7066.

[57] B. D. McCloskey et al. “Solvents’ critical role in nonaqueous lithium-oxygen battery electrochemistry”. *The Journal of Physical Chemistry Letters* 2 (2011), p. 1161.

[58] S. C. Ma et al. "Reversibility of noble metal-catalyzed aprotic Li-O_2 batteries". *Nano Letters* 15 (2015), p. 8084.

[59] Y. L. Zhang et al. "Amorphous Li_2O_2: chemical synthesis and electrochemical properties". *Angewandte Chemie* 55 (2016), p. 10717.

[60] B. D. McCloskey, J. M. Garcia, and A. C. Luntz. "Chemical and electrochemical differences in nonaqueous Li–O_2 and Na–O_2 batteries". *The Journal of Physical Chemistry Letters* 5 (2014), p. 1230.

[61] D. M. Brewis et al. "Pretreatment of poly(vinyl fluoride) and poly(vinylidene fluoride) with potassium hydroxide". *International Journal of Adhesion and Adhesives* 16 (1996), p. 87.

[62] G. J. Ross et al. "Surface modification of poly(vinylidene fluoride) by alkaline treatment 1. the degradation mechanism". *Polymer* 41 (2000), p. 1685.

[63] X. Luo et al. "Protocol of electrochemical test and characterization of aprotic Li-O_2 battery". *Journal of Visualized Experiments* (2016), e53740.

[64] M. M. Thackeray et al. "Li_2MnO_3-stabilized $LiMO_2$ (M = Mn, Ni, Co) electrodes for lithium-ion batteries". *Journal of Materials Chemistry* 17 (2007), p. 3112.

[65] A. Armstrong et al. "Demonstrating oxygen loss and associated structural reorganization in the lithium battery cathode $Li[Ni_{0.2}Li_{0.2}Mn_{0.6}]O_2$". *Journal of the American Chemical Society* 128 (2006), p. 8694.

[66] N. Yabuuchi et al. "High-capacity electrode materials for rechargeable lithium batteries: Li_3NbO_4-based system with cation-disordered rocksalt structure". *Proceedings of the National Academy of Sciences* 112.25 (2015), pp. 7650–7655.

[67] Z. Lu, D. D. MacNeil, and J. R. Dahn. "Layered $Li[Ni_xCo_{1-2x}Mn_x]O_2$ cathode materials for lithium-ion batteries". *Electrochemical and Solid-State Letters* 4.12 (2001), A200–A203.

[68] E. A. Olivetti et al. "Lithium-ion battery supply chain considerations: analysis of potential bottlenecks in critical metals". *Joule* 1.2 (2017), pp. 229–243.

[69] J. Lee et al. "Unlocking the potential of cation-disordered oxides for rechargeable lithium batteries". *Science* 343.6170 (2014), pp. 519–522.

[70] D. H. Seo et al. "The structural and chemical origin of the oxygen redox activity in layered and cation-disordered Li-excess cathode materials". *Nature Chemistry* 8 (2016), p. 692.

[71] J. Lee et al. "Reversible Mn^{2+}/Mn^{4+} double redox in lithium-excess cathode materials". *Nature* 556.7700 (2018), pp. 185–190.

[72] S. Hoshino et al. "Reversible three-electron redox reaction of Mo^{3+}/Mo^{6+} for rechargeable lithium batteries". *ACS Energy Letters* 2.4 (2017), pp. 733–738.

[73] H. Chen and M. S. Islam. “Lithium extraction mechanism in Li-rich Li_2MnO_3 involving oxygen hole formation and dimerization”. *Chemistry of Materials* 28 (2016), p. 6656.

[74] R. Wang et al. “A disordered rock-salt Li-excess cathode material with high capacity and substantial oxygen redox activity: $Li_{1.25}Nb_{0.25}Mn_{0.5}O_2$”. *Electrochemistry Communications* 60 (2015), pp. 70–73.

[75] N. Twu et al. “Designing new lithium-excess cathode materials from percolation theory: nanohighways in $Li_xNi_{2-4x/3}Sb_{x/3}O_2$”. *Nano letters* 15.1 (2015), pp. 596–602.

[76] J. Lee et al. “A new class of high capacity cation-disordered oxides for rechargeable lithium batteries: Li–Ni–Ti–Mo oxides”. *Energy & Environmental Science* 8.11 (2015), pp. 3255–3265.

[77] S. L. Glazier et al. “Characterization of disordered $Li_{(1+x)}Ti_{2x}Fe_{(1-3x)}O_2$ as positive electrode materials in Li-Ion batteries using percolation theory”. *Chemistry of Materials* 27.22 (2015), pp. 7751–7756.

[78] N. Yabuuchi et al. “Origin of stabilization and destabilization in solid-state redox reaction of oxide ions for lithium-ion batteries”. *Nature Communications* 7.1 (2016), pp. 1–10.

[79] J. Lee et al. “Mitigating oxygen loss to improve the cycling performance of high capacity cation-disordered cathode materials”. *Nature Communications* 8.1 (2017), pp. 1–10.

[80] M. S. Whittingham. “Lithium batteries and cathode materials”. *Chemical Reviews* 104.10 (2004), pp. 4271–4302.

[81] M. M. Thackeray et al. “Electrochemical extraction of lithium from $LiMn_2O_4$”. *Materials Research Bulletin* 19.2 (1984), pp. 179–187.

[82] A. Urban, J. Lee, and G. Ceder. “The configurational space of rocksalt-type oxides for high-capacity lithium battery electrodes”. *Advanced Energy Materials* 4.13 (2014), p. 1400478.

[83] Z. Lun et al. “Improved cycling performance of Li-excess cation-disordered cathode materials upon fluorine substitution”. *Advanced Energy Materials* 9.2 (2019), p. 1802959.

[84] J. Hong et al. “Critical role of oxygen evolved from layered Li–excess metal oxides in lithium rechargeable batteries”. *Chemistry of Materials* 24.14 (2012), pp. 2692–2697.

[85] R. Imhof and P. Novák. “Oxidative Electrolyte Solvent Degradation in Lithium-Ion Batteries: An In Situ Differential Electrochemical Mass Spectrometry Investigation”. *Journal of The Electrochemical Society* 146.5 (1999), pp. 1702–1706.

[86] S. Renfrew and B. McCloskey. “Quantification of surface oxygen depletion and solid carbonate evolution on the first cycle of $LiNi_{0.6}Mn_{0.2}Co_{0.2}O_2$ electrodes”. *ACS Applied Energy Materials* 2 (2019), p. 3762.

[87] W. D. Richards et al. "Fluorination of lithium-excess transition metal oxide cathode materials". *Advanced Energy Materials* 8.5 (2018), p. 1701533.

[88] A. Urban et al. "Electronic-structure origin of cation disorder in transition-metal oxides". *Physical Review Letters* 119.17 (2017), p. 176402.

[89] S. Hy et al. "Performance and design considerations for lithium excess layered oxide positive electrode materials for lithium ion batteries". *Energy & Environmental Science* 9.6 (2016), pp. 1931–1954.

[90] M. Freire et al. "A new active Li–Mn–O compound for high energy density Li-ion batteries". *Nature Materials* 15.2 (2016), pp. 173–177.

[91] V. Etacheri et al. "Challenges in the development of advanced Li-ion batteries: a review". *Energy & Environmental Science* 4.9 (2011), pp. 3243–3262.

[92] S. E. Renfrew and B. D. McCloskey. "Residual lithium carbonate predominantly accounts for first cycle CO_2 and CO outgassing of Li-stoichiometric and Li-rich layered transition-metal oxides". *Journal of the American Chemical Society* 139.49 (2017), pp. 17853–17860.

[93] M. M. Thackeray. "Manganese oxides for lithium batteries". *Progress in Solid State Chemistry* 25 (1997), p. 1.

[94] P. Kalyani et al. "Lithium metal rechargeable cells using Li_2MnO_3 as the positive electrode". *Journal of Power Sources* 80 (1999), p. 103.

[95] A. Robertson and P. Bruce. "Mechanism of electrochemical activity in Li_2MnO_3". *Chemistry of Materials* 15 (2003), p. 1984.

[96] D. Yu et al. "Electrochemical activities in Li_2MnO_3". *Journal of the Electrochemical Society* 156 (2009), A417.

[97] J. Rana et al. "Structural changes in Li_2MnO_3 cathode material for Li-ion batteries". *Advanced Energy Materials* 4 (2014), p. 1300998.

[98] S. F. Amalraj et al. "Phase transitions in Li_2MnO_3 electrodes at various states-of-charge". *Electrochimica Acta* 123 (2014), p. 395.

[99] F. Dogan et al. "Solid state NMR studies of Li_2MnO_3 and Li-rich cathode materials: Proton insertion, local structure, and voltage fade". *Journal of the Electrochemical Society* 162 (2015), A235.

[100] K. Kubota et al. "Direct synthesis of oxygen-deficient $Li_2MnO_{3\text{-x}}$ for high capacity lithium battery electrodes". *Journal of Power Sources* 216 (2012), p. 249.

[101] P. J. Phillips et al. "On the localized nature of the structural transformations of Li_2MnO_3 following electrochemical cycling". *Advanced Energy Materials* 5 (2015), p. 1501252.

[102] J. Croy et al. "First-cycle evolution of local structure in electrochemically activated Li_2MnO_3". *Chemistry of Materials* 26 (2014), p. 7091.

[103] Z. Lu and J. Dahn. “Understanding the anomalous capacity of Li/Li[$Ni_xLi_{1/3\text{ - }2x/3}Mn_{2/3\text{ - }x/3}O_2$ cells using in situ X-ray diffraction and electrochemical studies”. *Journal of the Electrochemical Society* 149 (2002), A815.

[104] J. S. Kim et al. “Electrochemical and structural properties of $_xLi_2MO$ 3·(1-x)$LiMn_{0.5}Ni_{0.5}O_2$ electrodes for lithium batteries (M = Ti, Mn, Zr; 0 $\leq x \leq 0.3$)”. *Chemistry of Materials* 16 (2004), p. 1996.

[105] C. S. Johnson et al. “The significance of the Li_2MnO_3 component in ‘composite’ xLi_2MnO_3·(1- x)$LiMn_{0.5}Ni_{0.5}O_2$ electrodes”. *Electrochemistry Communications* 6.10 (2004), pp. 1085–1091.

[106] P. Yan et al. “Probing the degradation mechanism of Li_2MnO_3 cathode for Li-ion batteries”. *Chemistry of Materials* 27 (2015), p. 975.

[107] C. S. Johnson et al. “Anomalous capacity and cycling stability of xLi_2MnO_3·(1- x) $LiMO_2$ electrodes (M= Mn, Ni, Co) in lithium batteries at 50 °C”. *Electrochemistry Communications* 9.4 (2007), pp. 787–795.

[108] J. Rana et al. “On the structural integrity and electrochemical activity of a 0.5Li_2MnO_3· 0.5$LiCoO_2$ cathode material for lithium-ion batteries”. *Journal of Materials Chemistry A* 2.24 (2014), pp. 9099–9110.

[109] J. Rana et al. “Structural changes in a Li-rich 0.5 Li_2MnO_3* 0.5$LiMn_{0.4}Ni_{0.4}Co_{0.2}O_2$ cathode material for Li-ion batteries: a local perspective”. *Journal of The Electrochemical Society* 163.6 (2016), A811.

[110] T. Teufl et al. “Oxygen release and surface degradation of Li- and Mn-rich layered oxides in variation of the Li_2MnO_3 content”. *Journal of the Electrochemical Society* 165 (2018), A2718.

[111] M. Radin et al. “Manganese oxidation as the origin of the anomalous capacity of Mn-containing Li-excess cathode materials”. *Nature Energy* 4 (2019), p. 639.

[112] B. Qiu et al. “Gas–solid interfacial modification of oxygen activity in layered oxide cathodes for lithium-ion batteries”. *Nature Communications* 7.1 (2016), pp. 1–10.

[113] V. Pimenta et al. “Synthesis of Li-rich NMC: A comprehensive study”. *Chemistry of Materials* 29 (2017), p. 9923.

[114] W. Gent. “Coupling between oxygen redox and cation migration explains unusual electrochemistry in lithium-rich layered oxides”. *Nature Communications* 8 (2017), p. 2091.

[115] J. Xu et al. “Elucidating anionic oxygen activity in lithium-rich layered oxides”. *Nature Communications* 9 (2018), p. 947.

[116] Z. Lebens-Higgins et al. “Distinction between intrinsic and X-ray-induced oxidized oxygen states in Li-rich 3d layered oxides and $LiAlO_2$”. *The Journal of Physical Chemistry C* 123 (2019), p. 13201.

[117] F. Massel et al. “Excess lithium in transition metal layers of epitaxially grown thin film cathodes of Li_2MnO_3 leads to rapid loss of covalency during first battery cycle”. *The Journal of Physical Chemistry C* 123 (2019), p. 28519.

[118] Z. Lebens-Higgins. “Revisiting the charge compensation mechanisms in $LiNi_{0.8}Co_{0.2y}Al_yO_2$ systems”. *Materials Horizons* 6 (2019), p. 2112.

[119] N. Li et al. “Unraveling the cationic and anionic redox reactions in a conventional layered oxide cathode”. *ACS Energy Letters* 4 (2019), p. 2836.

[120] P. Strobel and B. Lambert-Andron. “Crystallographic and magnetic structure of Li_2MnO_3”. *Journal of Solid State Chemistry* 75 (1988), p. 90.

[121] A. Boulineau et al. “Structure of Li_2MnO_3 with different degrees of defects”. *Solid State Ionics* 180 (2010), p. 1652.

[122] Y. Liang and D. Prendergast. “Quantum many-body effects in X-ray spectra efficiently computed using a basic graph algorithm”. *Physical Review B* 97 (2018), p. 205127.

[123] W. Yang and T. Devereaux. “Anionic and cationic redox and interfaces in batteries: Advances from soft X-ray absorption spectroscopy to resonant inelastic scattering”. *Journal of Power Sources* 389 (2018), p. 188.

[124] A. Jain et al. “Commentary: The materials project: A materials genome approach to accelerating materials innovation”. *APL Materials* 1 (2013), p. 011002.

[125] A. Christensen, P. Hansen, and M. Lehmann. “Isotope effects in the bonds of α-CrOOH and α-CrOOD”. *Journal of Solid State Chemistry* 21 (1977), p. 325.

[126] T. Yamamoto. “Assignment of pre-edge peaks in K-edge X-ray absorption spectra of 3d transition metal compounds: electric dipole or quadrupole?” *X-Ray Spectrometry* 37 (2008), p. 572.

[127] D. Wang et al. “Observation of lithiation-induced structural variations in TiO_2 nanotube arrays by X-ray absorption fine structure”. *Journal of Materials Chemistry A* 3 (2015), p. 412.

[128] S. Gautam et al. “Electronic structure modification and Fermi level shifting in niobium-doped anatase titanium dioxide thin films: a comparative study of NEXAFS, work function and stiffening of phonons”. *Physical Chemistry Chemical Physics* 18 (2016), p. 3618.

[129] J. Wandt et al. “Singlet oxygen evolution from layered transition metal oxide cathode materials and its implications for lithium-ion batteries”. *Materials Today* 21 (2018), p. 825.

[130] A. Grenier et al. “Reaction heterogeneity in $LiNi_{0.8}Co_{0.15}Al_{0.05}O_2$ induced by surface layer”. *Chemistry of Materials* 29 (2017), p. 7345.

[131] Z. W. Lebens-Higgins et al. “Evolution of the electrode–electrolyte interface of $LiNi_{0.8}Co_{0.15}Al_{0.05}O_2$ electrodes due to electrochemical and thermal stress”. *Chemistry of Materials* 30.3 (2018), pp. 958–969.

[132] K. Edström, T. Gustafsson, and J. O. Thomas. “The cathode–electrolyte interface in the Li-ion battery”. *Electrochimica Acta* 50.2-3 (2004), pp. 397–403.

[133] L. El Ouatani et al. “The effect of vinylene carbonate additive on surface film formation on both electrodes in Li-ion batteries”. *Journal of the Electrochemical Society* 156 (2009), A103.

[134] L. Dahéron et al. “Electron transfer mechanisms upon lithium deintercalation from $LiCoO_2$ to CoO_2 investigated by XPS”. *Chemistry of Materials* 20.2 (2008), pp. 583–590.

[135] A. Quesne-Turin et al. “Surface reactivity of Li_2MnO_3: first-principles and experimental study”. *ACS Applied Materials & Interfaces* 9.50 (2017), pp. 44222–44230.

[136] A. Robertson and P. Bruce. “The origin of electrochemical activity in Li_2MnO_3”. *ChemComm* (2002), p. 2790.

[137] J. N. Zhang. “Trace doping of multiple elements enables stable battery cycling of $LiCoO_2$ at 4.6 V”. *Nature Energy* 4 (2019), p. 594.

[138] E. McCalla et al. “Visualization of O-O peroxo-like dimers in high-capacity layered oxides for Li-ion batteries”. *Science* 350 (2015), p. 1516.

[139] Y. Xie, M. Saubanère, and M. L. Doublet. “Requirements for reversible extra-capacity in Li-rich layered oxides for Li-ion batteries”. *Energy & Environmental Science* 10.1 (2017), pp. 266–274.

[140] E. Zhao et al. “Local structure adaptability through multi cations for oxygen redox accommodation in Li-Rich layered oxides”. *Energy Storage Materials* 24 (2020), p. 384.

[141] M. P. Pechini. *Method of preparing lead and alkaline earth titanates and niobates and coating method using the same to form a capacitor*. US Patent 3,330,697. July 1967.

[142] K. M. Shaju, G. V. S. Rao, and B. V. R. Chowdari. “Performance of layered $Li(Ni_{1/3}Co_{1/3}Mn_{1/3})O_2$ as cathode for Li-ion batteries”. *Electrochimica Acta* 48.2 (2002), pp. 145–151.

[143] K. Kumai et al. “Gas generation mechanism due to electrolyte decomposition in commercial lithium-ion cell”. *Journal of Power Sources* 81-82 (1999), pp. 715–719. ISSN: 0378-7753.

[144] Q. Zhong et al. “Synthesis and Electrochemistry of $LiNi_xMn_{2-x}O_4$”. *Journal of the Electrochemical Society* 144.1 (1997), p. 205.

[145] T. Ohzuku and R. J. Brodd. “An overview of positive-electrode materials for advanced lithium-ion batteries”. *Journal of Power Sources* 174.2 (2007), pp. 449–456. ISSN: 0378-7753.

[146] J. R. Dahn et al. “Rechargeable $LiNiO_2$/carbon cells”. *Journal of the Electrochemical Society* 138.8 (1991), p. 2207.

[147] J. B. Goodenough and K. S. Park. “The Li-ion rechargeable battery: a perspective”. *Journal of the American Chemical Society* 135.4 (2013), pp. 1167–1176.

[148] S. Venkatraman and A. Manthiram. “Synthesis and characterization of P3-type CoO_2-δ”. *Chemistry of Materials* 14.9 (2002), pp. 3907–3912.

[149] R. Gupta and A. Manthiram. “Chemical extraction of lithium from layered $LiCoO_2$”. *Journal of Solid State Chemistry* 121.2 (1996), pp. 483–491. ISSN: 0022-4596.

[150] P. Kalyani et al. “Lithium metal rechargeable cells using Li_2MnO_3 as the positive electrode”. *Journal of Power Sources* 80.1-2 (1999), pp. 103–106.

[151] J. Rana et al. “Quantifying the Capacity Contributions during Activation of Li_2MnO_3”. *ACS Energy Letters* 5.2 (2020), pp. 634–641.

[152] B. D. McCloskey et al. “On the efficacy of electrocatalysis in nonaqueous Li–O_2 batteries”. *Journal of the American Chemical Society* 133.45 (2011), pp. 18038–18041.

[153] N. Li et al. “Unraveling the cationic and anionic redox reactions in a conventional layered oxide cathode”. *ACS Energy Letters* 4.12 (2019), pp. 2836–2842.

[154] G. G. Amatucci, J. M. Tarascon, and L. C. Klein. “Cobalt dissolution in $LiCoO_2$-based non-aqueous rechargeable batteries”. *Solid State Ionics* 83.1-2 (1996), pp. 167–173.

[155] J. L. Tebbe, T. F. Fuerst, and C. B. Musgrave. “Degradation of ethylene carbonate electrolytes of lithium ion batteries via ring opening activated by $LiCoO_2$ cathode surfaces and electrolyte species”. *ACS Applied Materials & Interfaces* 8.40 (2016), pp. 26664–26674.

[156] W. S. Yoon et al. “Oxygen contribution on Li-ion intercalation- deintercalation in $LiCoO_2$ investigated by O K-edge and Co L-edge X-ray absorption spectroscopy”. *The Journal of Physical Chemistry B* 106.10 (2002), pp. 2526–2532.

[157] H. Wang et al. “CO_2 and O_2 evolution at high voltage cathode materials of Li-ion batteries: a differential electrochemical mass spectrometry study”. *Analytical Chemistry* 86.13 (2014), pp. 6197–6201.

[158] S. Ramakrishnan et al. “Extended interfacial stability through simple acid rinsing in a Li-rich oxide cathode material”. *Journal of the American Chemical Society* 142.18 (2020), pp. 8522–8531.

[159] S. E. Renfrew and B. D. McCloskey. “Quantification of Surface Oxygen Depletion and Solid Carbonate Evolution on the First Cycle of $LiNi_{0.6}Mn_{0.2}Co_{0.2}O_2$ Electrodes”. *ACS Applied Energy Materials* 2.5 (2019), pp. 3762–3772.

[160] J. Wandt et al. “Singlet oxygen evolution from layered transition metal oxide cathode materials and its implications for lithium-ion batteries”. *Materials Today* 21.8 (2018), pp. 825–833.

[161] A. T. S. Freiberg et al. "Singlet oxygen reactivity with carbonate solvents used for Li-ion battery electrolytes". *The Journal of Physical Chemistry A* 122.45 (2018), pp. 8828–8839.

[162] N. Guerrini et al. "Charging Mechanism of Li_2MnO_3". *Chemistry of Materials* 32.9 (2020), pp. 3733–3740.

[163] B. D. McCloskey et al. "Combining accurate O_2 and Li_2O_2 assays to separate discharge and charge stability limitations in nonaqueous Li–O_2 batteries". *The Journal of Physical Chemistry Letters* 4.17 (2013), pp. 2989–2993.

[164] Y. K. Sun et al. "High-energy cathode material for long-life and safe lithium batteries". *Nature Materials* 8.4 (2009), pp. 320–324.

[165] C. Tian, F. Lin, and M. M. Doeff. "Electrochemical characteristics of layered transition metal oxide cathode materials for lithium ion batteries: surface, bulk behavior, and thermal properties". *Accounts of Chemical Research* 51.1 (2017), pp. 89–96.

[166] M. C. Biesinger et al. "Resolving surface chemical states in XPS analysis of first row transition metals, oxides and hydroxides: Cr, Mn, Fe, Co and Ni". *Applied Surface Science* 257.7 (2011), pp. 2717–2730.

[167] K. G. Gallagher et al. "Quantifying the promise of lithium–air batteries for electric vehicles". *Energy & Environmental Science* 7.5 (2014), pp. 1555–1563.

[168] S. Okuoka et al. "A new sealed lithium-peroxide battery with a Co-doped Li_2O cathode in a superconcentrated lithium bis(fluorosulfonyl)amide electrolyte". *Scientific Reports* 4 (2014), p. 5684.

[169] H. Kobayashi et al. "Improved performance of Co-doped Li_2O cathodes for lithium-peroxide batteries using $LiCoO_2$ as a dopant source". *Journal of Power Sources* 306 (2016), pp. 567–572.

[170] H. Kobayashi et al. "Synthesis of Cu-doped Li_2O and its cathode properties for lithium-ion batteries based on oxide/peroxide redox reactions". *Journal of Power Sources* 340 (2017), pp. 365–372.

[171] H. Arai et al. "Electrochemical and structural study of Li_2CuO_2, $LiCuO_2$ and $NaCuO_2$". *Solid State Ionics* 106.1-2 (1998), pp. 45–53.